Doctoral Dissertation
博士論文

Classification and Representation of Physical States by Neural Networks

(ニューラルネットワークによる物理状態の判定および表現**)**

Dissertation Submitted for Degree of Doctor of Philosophy
December 2019
令和元年 **12** 月博士（理学）申請

Department of Physics, Graduate School of Science,
The University of Tokyo
東京大学大学院理学系研究科物理学専攻

Nobuyuki YOSHIOKA
吉岡　信行

Publication by the Author

1. N. Yoshioka, H. Matsuura and M. Ogata,
   "Quantum Hall Effect of Massless Dirac Fermions and Free Fermions in Hofstadter's Butterfly,"
   J. Phys. Soc. Jpn. **85**, 064712 (2016).

2. N. Yoshioka, Y. Imai, and M. Sigrist,
   "Spontaneous thermal Hall effect in three-dimensional chiral superconductors with gap nodes,"
   J. Phys. Soc. Jpn. **87**, 124602 (2018).

3. N. Yoshioka, Y. Akagi, and H. Katsura,
   "Learning Disordered Topological Phases by Statistical Recovery of Symmetry,"
   Phys. Rev. B **97**, 205110 (2018).

4. N. Yoshioka, Y. Akagi, and H. Katsura,
   "Transforming generalized Ising model into Boltzmann machine,"
   Phys. Rev. E **99**, 032113 (2019).

5. N. Yoshioka and R. Hamazaki,
   "Constructing neural stationary states in open quantum many-body systems,"
   Phys.Rev. B **99**, 214306 (2019).

6. N. Yoshioka, Y. O. Nakagawa, K. Mitarai, and K. Fujii,
   "Variational Quantum Algorithm for Non-equilibrium Steady States,"
   arXiv:1908.09836 (2019).

7. N. Yoshioka, Y. Akagi, and H. Katsura
   "From classification to representation of physical states by neural networks,"
   Solid State Physics **54**, 475 (2019). (in Japanese)

8. N. Shibata, N. Yoshioka, and H. Katsura,
"Onsager's scars in disordered spin chains,"
arXiv:1912.13399 (2019).

9. Z. Gong, N. Yoshioka, N. Shibata, and R. Hamazaki,
"Universal error bound for constrained quantum dynamics,"
arXiv:2001.03419 (2020).

10. Z. Gong, N. Yoshioka, N. Shibata, and R. Hamazaki,
"Error bounds for constrained dynamics in gapped quantum systems: Rigorous results and generalizations,"
arXiv:2001.03421 (2020).

Acknowledgments

I would like to express my sincere gratitude to my supervisor, Prof. Hosho Katsura, for the continuous and meticulous support of my Ph.D. research, advice based on his immense knowledge, stimulating discussions, and generosity. I would like to express my appreciation to Prof. Masahito Ueda, my secondary supervisor through the Advanced Leading Graduate Course for Photon Science (ALPS), for his insightful comments on research and thoughtful words on career. I am deeply grateful to the member of my defence committee for their fruitful and critical comments: Prof. Naoki Kawashima as the chair committee and Prof. Kensuke Kobayashi, Prof. Taisuke Ozaki, Prof. Kazumasa Takeuchi, and Prof. Yohei Yamaji as the vice committees.

I gratefully acknowledge the financial support from ALPS, the Japan Society for the Promotion of Science (JSPS) and Computational Science Alliance.

I owe a sincere gratitude to Dr. Yutaka Akagi, the Assistant Professor of our group, for his enthusiasm for discussion, warm advice, and constant encouragement. His support has been essential in keeping me on the track of the Ph.D. program. I would like to thank Dr. Ryosuke Akashi, Dr. Yusuke Nomura, Prof. Tsuyoshi Okubo, Prof. Synge Todo, Dr. Akihito Soeda, Dr. Hidemaro Suwa, Prof. Shu Tanaka for fruitful discussion, insightful advice, and sharing their vast knowledge.

My deep gratitude goes to Prof. Franco Nori for the passionate discussion and the kind offer for a postdoctoral position in RIKEN. The stimulating and front-line research environment excites me. I would like to express my thanks to Dr. Clemens Gneitig and Dr. Ken Funo for the fruitful and mind-opening discussions.

I greatly appreciate my productive, bright, and supportive colleagues and group mates. I express my gratitude to Mr. Ryusuke Hamazaki for the intensive discussion and toughness to produce a scientific progress. I am grateful to Mr. Zongping Gong for his deep insights and eagerness to share his knowledge

through refined discussion. My gratitude goes to Mr. Naoyuki Shibata for his willingness to make a steady progress and keen perception in discussion.

The works in the current thesis have been strongly motivated by the fruitful discussions. I sincerely appreciate Dr. Evert van Nieuwenburg for his enlightening seminars, helpful discussions, and enthusiastic encouragement. My appreciation goes to Mr. Kenny Choo for the numerous support and helpful discussions. I would express my deep acknowledgement to Prof. Lei Wang for the valuable and supportive comments. I owe very important debts to Dr. Jinguo Liu, Mr. Soshi Mizutani, Prof. Titus Neupert, Prof. Nic Shannon, and Prof. Manfred Sigrist for their kind invitation and hospitality during my visit.

I would like to express my gratitude to Dr. Naoki Kanazawa, Mr. Yoshifumi Inui, and Dr. Yuto Murashita for their patience for sharing profound knowledge and helping out with career thinking. I wish to express my thanks for the members of QunaSys Inc. for the invoking discussions. My appreciation in particular goes to Prof. Keisuke Fujii, Mr. Kosuke Mitarai, Prof. Wataru Mizukami, Dr. Yuya. O. Nakagawa, and Mr. Tennin Yan for their valuable comments on research, stimulating discussion based on sharp perspectives.

I would like to thank the administrative officers in our department for their solid work. Warm supports by our secretaries have been indispensable: Ms. Saki Kohno, Ms. Yoshie Sayama, Ms. Yumiko Wada and Ms. Chiharu Yoshioka.

I would like to express my sincere acknowledgements to all my friends who supported my personal life during the Ph.D. program. My deepest gratitude goes to Mr. Kenei Matsudaira, Mr. Haruhisa Tabata, and Ms. Kazuko Tamagaki for the heartwarming conversations, thoughtful encouragements, and stimulating philosophy. Last but not least, I would like to show my greatest appreciation to my family for their continuous support not only during my graduate study but throughout my life.

Abstract

The technological progress in the computational resource, invention of efficient optimization technique, and the enhancement of the capability to handle enormous amount of variational parameters have accelerated the application of the neural networks to various tasks. Although the method evolved in the field of machine learning, the target issues can be more diverse. Numerous problems in condensed matter physics or statistical physics are excellent candidates, and indeed new ideas and techniques have been proposed rapidly through integration of knowledge. Our objective is to develop new frameworks that apply the neural networks as the machine to solve tasks in condensed matter physics.

In the present thesis, we provide novel methodologies on three topics. The first is the classification of disordered topological systems using the neural network, trained in the clean limit, to perform "phase recognition" on data obtained by numerical calculation. The second is the representation of classical spin systems in thermal equilibrium. We find that the transformation of the generalized Ising model into the Boltzmann machines are beneficial from the viewpoint of Monte Carlo simulation. The third is the representation of the stationary states of open quantum many-body systems. The variational optimization of the ansatz based on complex-valued restricted Boltzmann machine allows one to simulate the desired state far more efficiently compared to the brute-force calculation by exact diagonalization.

Contents

Acronyms

BM Boltzmann machine. 17

CPTP completely-positive trace-preserving. 66

cRBM complex-valued restricted Boltzmann machine. 20, 64, 75, 89

DBM deep Boltzmann machine. 10, 19, 43

DIT decoration-iteration transformation. 44

GKSL Gorini-Kossakowski-Sudarshan-Lindblad. 63, 66

MC Monte Carlo. 41

MLP multilayer perceptron. 13, 23

NSS neural stationary state. 64, 74

RBM restricted Boltzmann machine. 9, 18, 43

SGD stochastic gradient descent. 95

SR stochastic reconfiguration. 78

SSF single-spin flip. 41

STT star-triangle transformation. 44

ThM thermal metal. 28, 101

TM transfer matrix. 25, 97

VMC variational Monte Carlo. 73

1
Introduction

The revolutionary success of the (artificial) neural network boosted the advancement in various computer science fields such as the image or speech recognition and machine translation [1–4]. Although the theoretical understanding on the success of the neural networks has not been fully explored [5], it is not too bold to state that the practical factors are three-fold: the drastic improvement in the computational resource, the development of efficient optimization technique, and the increase in the number of variational parameters which enhances the representation power. While the technology itself was invented in the field of machine learning, the target problems can be ubiquitous; the methodology awaits further opportunity to exert its potential in other research fields. Numerous problems in condensed matter physics or statistical physics are excellent candidates, and indeed novel ideas and techniques have been developed rapidly through integration of knowledge. To understand this, we start with introducing some terminologies and notions in machine learning.

Loosely speaking, in machine learning a "machine" which extracts information from data to generate predictions is constructed by applying an appropriate "learning" algorithm. A succinct and insightful definition is given by Mitchell as follows [6, 7];

> *A computer program is said to learn from experience E with respect to some class of tasks T and performance measure P, if its performance at tasks in T, as measured by P, improves with experience E.*

Prompted by this elegant description, we find very useful to build such an element-wise understanding.

Task T**.** A task, in short, is the problem you want to solve. In an abstract sense, a task indicates a process that extracts appropriate information via operations on some quantified data.

The major tasks with excellent connections to physics include the classification, representation, generation, and regression. Concise descriptions are given as follows,

- *Classification* refers to the attempt to provide some discrete label on a data. In physics language, the objective is to identify qualitative physical properties such as phases. A classification task is discussed in Chapter 3 of this thesis.

- *Representation* aims to obtain low-dimensional expression that reproduces or approximates the target dataset or model. The equivalent objectives in physics are diverse: low dimensional variational parametrization of many-body states, reconstruction of true probability distribution via restricted measurement recourse, and so on. We consider the representation task in exact and approximate manner in Chapter 4 and 5, respectively.

- *Generation* concerns sampling of new data that obeys the probability distribution of some desired model or existing dataset. For instance, increasing the amount of data based on appropriate inference to improve classification task or designing a new algorithm with improved autocorrelation can be understood as the generation.

- *Regression* involves the prediction of the (usually) continuous output from a given function whose explicit operation is unknown. For instance, forecasting the physical property of a matter from its atomic structure or the descriptor is considered to be a regression task.

In the current thesis, we intensively focus on the classification and representation tasks that are expected to advance dramatically by interdisciplinary study. Obviously, the discussion of the task is associated with that of the nonlinear function that actually executes the task. Hence, in the current thesis, we emphasize the importance of *"computer program"* in the Mitchell's words, and refer to it as the **machine**.

Performance P**.** The performance is the quantitative indicator which is necessary to evaluate the algorithm, or equivalently the machine. While a random machine does not satisfy the criteria required for a given task in general, it is natural to attempt to improve the machine in a quantitative way by optimizing an

Chapter	Task T and Machine M	Performance P	Experience E
3	Classification by MLP	Cross entropy	Quantum state, supervised
4	Representation by real BM	-	Thermal state, -
5	Representation by complex RBM	"Energy"	Mixed state, unsupervised

Table 1.1: Element-wise understanding of the contents in Chapter 3, 4, and 5.

appropriate objective that reflects the capability of the algorithm. Finding a well-defined and numerically stable measure with respect to the task is crucial. A more frequently-used term equivalent to the performance P is the **cost function**, which would be used in this thesis interchangeably. Note that the performance may not be considered in a case where the exact construction of the machine is the task itself, such as the case in Chapter 4.

Experience E. The experience is the dataset used to evaluate and improve the performance of the machine. Machine learning algorithms can be divided into two types with respect to the property of the dataset: the supervised and the unsupervised learning. The supervised learning scheme considers a dataset with every data accompanied with its "answer." Namely, we have access to both the input and its corresponding output for the machine. The unsupervised learning, on the other hand, does not assume the output. Only the input data is available.

Now we have prepared the perspective to discuss physics problems and machine learning in a unified way, and therefore ready to state the main topic of this thesis. Namely, our objective is to develop new frameworks that apply the neural networks as the machine to solve tasks in condensed matter physics. As is summarized in Table 1.1, we focus on the classification of disordered topological systems, representation of both classical and quantum systems in particular.

1.1 Classification task in physics

In the classification task, the machine assigns discrete labels for finite- or infinite-dimensional data. A familiar example is the automated tagging for digital images. The data representing the RGB values is processed by some "prediction machine" that calculates the label based on image recognition techniques. The neural network is commonly used to perform such a complicated mapping from the RGB values to the label [8]. The machine learning community has recognized

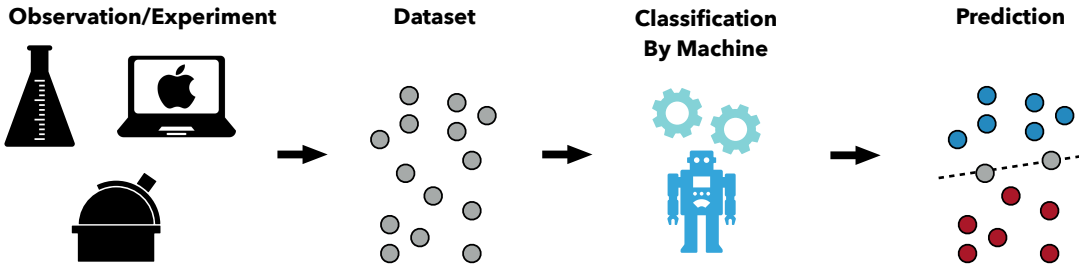

Figure 1.1: Procedure of classification task by machine. A dataset gathered by observation, experiment, numerical calculation is passed to a machine that performs multiclass labeling.

the task of developing an efficient classification machine as one of the central problems for visionary, audible or market data. Recent findings show that the background of the data could be even more diverse; the neural networks can handle data gathered via scientific experiments or numerical simulations that are intended to investigate natural phenomena. Of course, including condensed matter physics.

Needless to say, the classification of phases is one of the fundamental tasks in physics as well. In the work by Carraquilla and Melko, they showed that the finite temperature phases of the two-dimensional Ising model can be successfully classified by a neural network trained by the supervised learning scheme [9]. Here, the input data is a "gray image" with each binary pixel corresponding to the up or down spin. The results suggest that the machine learns the feature corresponding to the local order parameter, and hence becomes capable of not only the classification of the unseen data but also prediction of the phase transition temperature. The classification task in systems with local order parameter is in good connection with the ordinary image recognition technique, and is confirmed to be valid in numerous systems in either supervised or unsupervised scheme [10–16].

Nontrivial application has been done for many-body localized states [17–20]. The many-body localization refers to the quantum phenomenon in which a non-integrable many-body interacting system is prohibited to thermalize due to the "localization in the Hilbert space" caused by the disorder [21, 22]. Classification schemes proposed for such a property focus on the behaviour of the entanglement entropy or eigenvalue statistics. The study by Schindler *et al.* showed that by feeding a neural network with the entanglement spectra, which is the negative logarithm of the spectrum of a reduced density matrix for appropriate subsystem,

one may classify the quantum phase with relatively low numerical cost [17]. Also, van Nieuwenburg *et al.* showed that the dynamics of a quantum state, which can be expected to encode richer information compared to a single eigenstate, can also be used as the input data for the machine [20, 23].

Even more intriguing direction is the classification of topological phases, which cannot be characterized by local order parameters as well. Since the discovery of the quantum Hall effect [24, 25], physicists have been fascinated by the bizarre concept of classifying quantum states based on the band topology of wave functions up to now. Given the profoundness and abundance of its nature, it is undoubtedly counted as one of the most significant and difficult classification tasks in condensed matter physics. It is very natural to apply the machine learning approach to promote further understanding; one may take the many-body correlation function as the input for the neural network trained by data generated from noninteracting fermion systems to classify phases of interacting fermion systems [26], or take the Fourier-space representation of Bloch components of a Hamiltonian to feed into machine that learns the formula of winding number [27]. While these works tackle systems in the clean limit, the real challenge lies in the disordered regime.

While the disorder and impurity are present in real materials, the commonly-used formulae for topological invariants break down when the translation symmetry is absent. An image-classification-based approach offers a powerful method to compensate for this gap. In the Chapter 3 of this thesis, we discuss a method to predict the quantum phase under disorder based on a machine trained to classify phases in the clean limit. In sharp contrast with the previous works by Ohtsuki and Ohtsuki [28, 29], we establish a novel method which allows us to investigate disordered systems that assume knowledge of only the clean limit. Furthermore, the proposed method is numerically advantageous compared to other methods such as the transfer matrix method and the noncommutative geometry approach from the perspective of the variety of applicable models; the former method becomes inefficient when multiple phase boundaries approach each other and the latter is ill-defined when both the bulk and mobility gap is closed. We see that neural-network-based method is capable of both difficulties.

As the closing of this section, we would like to mention the diverse methodology of integrating knowledge in physics and computer science.

- One may focus on the significant difference between the two fields – the generation of synthetic data from physical models allows one to modify

the model parameters almost freely. Van Nieuwenburg *et al.* proposed a "confusion scheme" to find the ground-truth transition point as the best criteria obtained by sorting the fictitious "transition point" [30]. Broecker *et al.* argued that the sudden change of behavior near the critical point can be captured by the anomaly detection technique [31].

- Exporting the notion and knowledge of physics is also promising. It is notable that the tensor network, which is one of the most powerful "machine" developed for quantum systems, has been applied to image recognition tasks [32–36].

- Application of machine learning technique to experimental data is attracting attention [37–39]. In Ref. [39], Zhang *et al.* trained a classifier trained by synthetic data generated from physical models with impurity, and applied to the experimental data obtained by STM.

1.2 Representation task in physics

Another valuable task with progressive results is the **representation** of physical states. In the present thesis, we define the representation as the explicit expression of physical states such as the ground-state wave function of isolated systems and the stationary-state density matrix of open quantum systems. For instance, an exactly soluble model can be rephrased as "the model with the exact representation of the eigenstates available" and an attempt to calculate the ground state via variational optimization can be described as the "calculation of the approximate representation of the ground state." Also, the function (or machine) may be referred to as "the representation function (machine)."

In a data-driven task, one usually does not have access to the exact representation, or the ground truth, of the probability distribution from which the dataset was drawn. The goals of building the representation, which is closely related to the representation learning in the field of machine learning, are mainly two-fold:

- *Higher performance in classification.* Constructing an approximate machine often involves feature extraction of the data by parametrization. This can be used to improve tasks such as the classification.

- *Mass and cheap production of new data.* Once the distribution of the data is learned with sufficient accuracy, sampling can be done from the machine

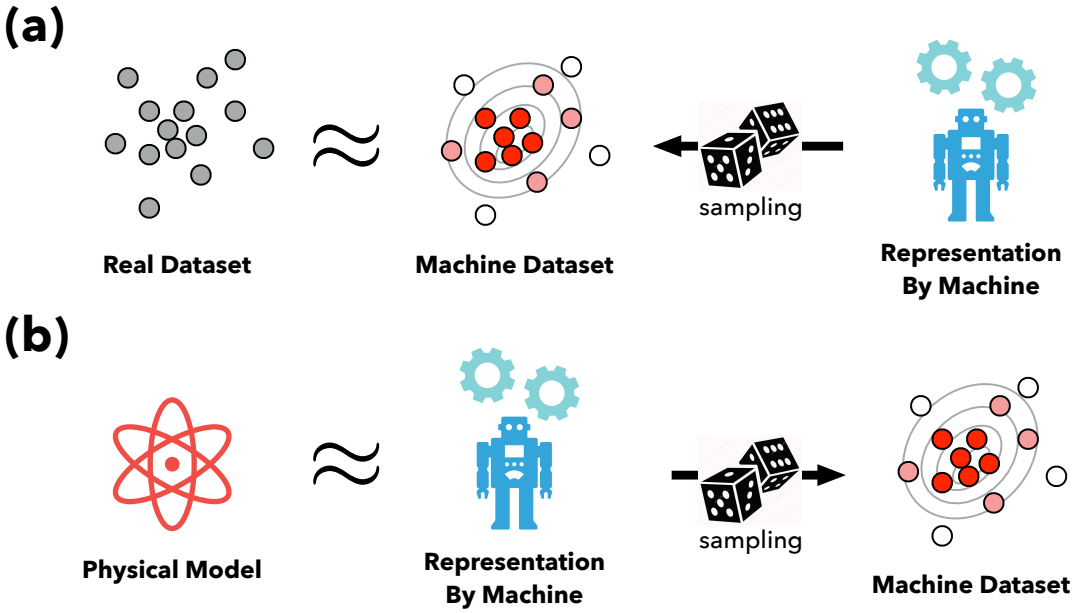

Figure 1.2: Two flavours of representation task. (a) A data-driven approach. Given a dataset, one trains the machine so that the data generated by the machine resembles the real ones. Building a parametrized representation is expected to construct further understanding of the real dataset. (b) A model-driven approach. Given a model that describes some natural phenomena, one constructs a machine either approximates or exactly reproduces the original model. The machine allows one to perform cheaper sampling and accelerates the understanding of the original model.

instead of the original source.

While computational physics may differ from the ordinary machine learning in terms of the accessibility to the data resource, as is graphically described in Fig. 1.2, the both of fields appreciate the above-mentioned points to establish better understanding of the data or model.

1.2.1 Representation of classical system

Building the approximate representation in classical systems has been studied intensively in the field of machine learning and statistics. An example is the inverse engineering of the model that reproduces the obtained dataset. [See Fig. 1.2(a) for graphical illustration.] Various approaches have been developed [40]

for parameter estimation including mean field theory [41], contrastive-divergence method [42], minimum probability flow [43], and the use of variational autoregressive model [44].

The approximate representation in condensed matter physics can be used to accelerate the Monte Carlo simulations such as the classical Ising model on the square lattice [45–47], the Falicov-Kimball model [48], and the classical spin glass model [44]. However, construction of such representation requires some extra numerical cost, and it is desirable to have a training-free algorithm that draws samples efficiently. As we discuss in Chapter 4, this strongly motivates us to construct an exact transformation of a model with difficulty in sampling into another equivalent one with different representation in which the cluster update algorithm can be applied to speed up the simulation in terms of the autocorrelation between the samples. In particular, we consider a mapping of a model with many-body interacting binary degrees of freedom into the Boltzmann machine. In other words, we get rid of the higher order interactions at the expense of additional auxiliary degrees of freedom. We see that the application of the cluster update algorithm would significantly reduce the autocorrelation compared to the vanilla single-spin flip algorithm.

1.2.2 Representation of quantum system

Search of approximate representation has been one of the significant issues in numerical investigation of quantum many-body systems. The main objective is to avoid the bottlenecks that arise in principal, namely the exponential increase in the memory consumption and numerical cost. Unless one builds a quantum simulator or universal quantum computer with sufficient fidelity, this severely limits the accessible system sizes via full-space approach such as the exact diagonalization, and instead deal with some machine that accurately captures the property of the physical system with reduced degrees of freedom.

The approach by the tensor network states has been recognized as one of the most successful methods [49, 50]. In a gapped one-dimensional (1d) system, for instance, an ansatz called the Matrix Product State (MPS) gives highly accurate approximation of the ground state via optimization by the Density Matrix Renormalization Group (DMRG) [51]. This success is currently attributed to the structure of the quantum entanglement; the entanglement entropy of the ground state in gapped 1d systems obey the area-law, which is satisfied in the

MPS [52–54]. The drastic restriction of the Hilbert space enables prompt and precise search of the objective state. Numerous extensions of the MPS have been proposed: the Projected Entangled Pair States (PEPS) that are capable of states in two-dimensions (2d) with area-law entanglement [55][*1], the Multiscale Entangled Renormalization Ansatz (MERA) for sub-volume-law states such as the ground states of critical 1d systems [56], and the Tree-Tensor Network (TTN) with the connectivity of the tensors given by the tree-structure [57]. Compared to the extreme progress in 1d systems, the approximate representation by the tensor network in higher dimensions including 2d is not as striking, and new methods are actively investigated.

The recent findings for the ability of the neural networks as representation machine have attracted intensive attention [58–60]. Carleo and Troyer showed that the restricted Boltzmann machine (RBM), a representation machine with auxiliary degrees of freedom that interact with the whole system, can be optimized via the variational Monte Carlo method to accurately express the ground states of quantum spin models such as the tranverse-field Ising model in 1d and the antiferromagnetic Heisenberg model in both 1d and 2d [61][*2]. The accuracy for the 2d system is comparable with that obtained by the tensor network approach. This is partly understood due to the ability to express states with large entanglement, and the dimension-free construction of the connection between the physical and auxiliary degrees of freedom. Deng *et al.* have shown that the maximally entangled pure state of spin-1/2 system can be expressed with only polynomial number of parameters with respect to the system size, where the requirement by the tensor network ansatz scales exponentially [62]. This lead condensed matter physicists to consider systems with fermionic [63, 64] or bosonic [65, 66] degrees of freedom, chiral topological states [67–69], anyonic symmetry [70], and topological order such as the surface codes [71–73].

Despite its capability to express highly-entangled states, the RBM alone does not open a road to simulate arbitrary physical states efficiently[*3]; another hidden

[*1] Calculation of physical observables such as the correlation function based on the canonical form requires massive numerical cost. This is one of the bottlenecks for the application of the PEPS.

[*2] The calculation in Ref. [61] is done for wavefunctions with real and non-nnegative values under the periodic boundary condition.

[*3] It is notable that the investigation into one of the major challenge in 2d system, the J_1- J_2 Heisenberg model [74–76] with controversial property of its ground state in the frustrated regime, has not been able to exhibit strong merit over the result by tensor network approach.

layer on top of an RBM, or the deep Boltzmann machine (DBM), would achieve even higher representability. For instance, arbitrary quantum circuit can be expressed with an DBM with auxiliary degrees of freedom scaling only linearly with respect to the qubit number and the circuit depth [77]. The representation power of the RBM, on the other hand, has been investigated through comparison of the tensor network states [78], and is currently understood to be equivalent to the class of variational states named the correlator-product-states [67, 79]. While Carleo *et al.* and Freitas *et al.* developed a method to perform exact imaginary-time evolution on the DBM, the applicability is limited [80, 81]. It is still not clear how to utilize the representation power of the DBM.

There has been continuous effort to extend the variational method to the excited states [82], imaginary time evolution toward the ground state [80, 81] and the finite temperature state [83]. Although the applicability has been largely expanded, approximate representations by the neural networks have yet to be applied to one of the most challenging problems in modern condensed matter physics – the open quantum many-body systems. It is notoriously difficult to solve the fundamental equation of motions for such systems, which is often well captured by the time-homogeneous quantum master equation. Besides the brute-force calculation by the exact diagonalization, few methods have been developed up to now. The quantum jump method, which consider dynamics of pure states that stochastically undergo "jump" caused by dissipation, would require a large amount of sampling when the steady state is thermal, and the variational calculation based on the tensor network ansatz suffers when the quantum entanglement is large. Motivated by such situations, in Chapter 5, we develop a new method to simulate the nonequilibrium stationary state of open quantum many-body systems.

1.3 Organization of this Thesis

Here, let us outline the organization of this thesis. In Chapter 2, we introduce the machines that are used for the classification and representation tasks. In particular, we focus on the simplest and most versatile machines applied to the classification and representation tasks. As the classification machine, we introduce the multilayer perceptron and the convolutional neural network. Either is a non-linear function consisting of huge number of parameters such that arbitrary function can be expressed by increasing the degrees of freedom. As the repre-

sentation machine, we introduce the Boltzmann machine. Furthermore, models with restrictions on the connectivity between the physical and auxiliary spins are given to define the restricted and deep Boltzmann machines. We also discuss the complex-valued Boltzmann machine as well.

In Chapter 3, we develop a new scheme to classify the quantum phases of free-fermion systems under disorder. Given the disorder that keeps the discrete symmetries of the ensemble as a whole, we argue that translational symmetry, which is broken in the individual quasiparticle distribution, is recovered statistically by taking the ensemble average. This enables one to classify the quantum phases in the disordered regime using a neural network trained in the clean limit. We demonstrate our method by applying it to a two-dimensional system in the class DIII by showing that the result obtained from the machine is totally consistent with the calculation by other independent methods. Furthermore, the proposed method is capable of parameter regions in which the transfer martix method (noncommutative geometry approach) becomes inefficient (ill-defined) due to the approaching multiple phase boundaries (bulk/mobility gap closing).

In Chapter 4, we find an exact representation of the generalized Ising models using the Boltzmann machine. We show that the appropriate combination of the algebraic transformations, namely the star-triangle and decoration-iteration transformations, allows one to express the many-spin interaction in terms of fewer-spin interactions at the expense of the degrees of freedom. Furthermore, we find that the application of such a representation is beneficial from the viewpoint of Monte Carlo simulations since the celebrated cluster update algorithm becomes applicable. We demonstrate this point by applying the cluster-update algorithm by Swendsen and Wang, and find that the critical slowing down observed in the single-spin flip algorithm is drastically reduced in a model with two- and three-spin interactions on the Kagomé lattice. Our framework provides a general and systematic procedure to speed up the Monte Carlo studies in many-spin interacting models.

In Chapter 5, we develop a numerical algorithm that builds the approximate representation of stationary states in open quantum many-body systems. Our algorithm, dubbed as the neural stationary state algorithm, performs a variational optimization on an ansatz based on the complex-valued restricted Boltzmann machine to compute the stationary states of quantum dynamics obeying the time-homogeneous quantum master equations. This is enabled by considering a mapping of the stationary-state search problem into finding a zero-energy

ground state of an appropriate Hermitian operator. Our method is demonstrated to simulate various dissipative spin systems efficiently, i.e., the transverse-field Ising models in both one and two dimensions and the XYZ model in one dimension that are subject to damping effect.

Chapter 6 is devoted to the Summary of this thesis. Some supplemental materials are provided in Appendices.

2
Machines for Classification and Representation

In this chapter, we introduce the machines that are used in the classification and representation tasks. While the flexibility of the neural network allows one to consider some specific structure that best fits one's objective [*1], here we deal with the most versatile, simple, and hence popular structures. Also note that the usage of the machines are not rigorously fixed to specific tasks. Namely, the machines for representation may ultimately used to improve the accuracy in classification, and vice versa.

2.1 Machines for Classification

Machines used in the classification task are required to be mathematical models that take high-dimensional input data to return continuous/discrete values through deterministic calculations. Among the variety of such models, usually called as the discriminative models in the field of machine learning, we consider the artificial neural networks, since it performs very good in numerous classification tasks. In particular, we introduce one of the most basic models: the **multilayer perceptron (MLP)** [*2] and the **convolutional neural network (CNN)**.

2.1.1 Multilayer perceptron

The multilayer perceptron (MLP), one of the most simple and typical models applied to classification tasks, is a nonlinear function that takes an input $\mathbf{x}$ to compute an output $\mathbf{y}$ through sequential mappings by layers of perceptrons. While we exclusively consider a model with real values in the following, it can be easily extended to incorporate complex values.

[*1] Refer to **Neural Network Zoo** (`http://www.asimovinstitute.org/neural-network-zoo/`) for detailed information.

[*2] The MLP is also known as the fully-connected neural network, vanilla neural network, feed-forward neural network etc.

Before discussing the MLP, let us consider a **single perceptron** [84]. As is graphically illustrated in Fig. 2.1(a), a single perceptron is a nonlinear function that applies the activation function to each element of the weighted input. The concrete expression of a single perceptron that takes an N-dimensional vector $\mathbf{x} \in \mathbb{R}^N$ (or $\mathbb{C}^{N*3}$) to return a value $y \in \mathbb{R}$ can be given as

$$y = \mathcal{A}(z) = \mathcal{A} \circ \mathcal{W}(\mathbf{x}), \tag{2.1}$$

$$z = \mathcal{W}(\mathbf{x}) = \sum_i W_i x_i + b, \tag{2.2}$$

$$\mathcal{A}(z) = A(z), \tag{2.3}$$

where $\mathcal{W} : \mathbb{R}^N \to \mathbb{R}$ is the weighing operation and $\mathcal{A} : \mathbb{R} \to \mathbb{R}$ is the activation operation. The weighing operation in a single perceptron first multiplies the weight W_i on the i-th input and then add the bias b. The activation operation, on the other hand, operates a non-linear activation function A such as the sigmoid, tanh, or ReLU functions.

A set of perceptrons that share an identical input is called a **layer**. The MLP is a many-perceptron model with layers that can be uniquely numbered according to the order of input and output and do not include any intralayer processing. [See Fig. 2.1(b).] The first and last layers, or the input and output layers, sandwich the in between **hidden layers** which play an important role in increasing the expressive power to perform feature extraction. In the following, we consider a MLP with M hidden layers with m-th layer consisting of N_m units. Note that the input and output layers can be considered as the 0-th and $(M+1)$-th layers in such a notation.

The weighing and activation operations in the m-th layer are given as $\mathcal{W}_m : \mathbb{R}^{N_{m-1}} \to \mathbb{R}^{N_m}$ and $\mathcal{A}_m : \mathbb{R}^{N_m} \to \mathbb{R}^{N_m}$, respectively. Correspondingly, the output is calculated as

$$\mathbf{y} = \mathcal{A}_{M+1} \circ \mathcal{W}_{M+1} \circ \cdots \circ \mathcal{A}_1 \circ \mathcal{W}_1(\mathbf{x}), \tag{2.4}$$

where the intermediate output from the $(m-1)$-th layer $\mathbf{y}^{(m-1)} \in \mathbb{R}^{N_{m-1}}$ is pro-

[*3] It is natural to consider extension to complex-valued ones. Although this naively seems to be suitable to describe complex systems, the analyticity of the activation function would be lost. Instead, some works have adopted the real-valued network to output both the amplitude and the phase of the wave function for quantum systems [64–66].

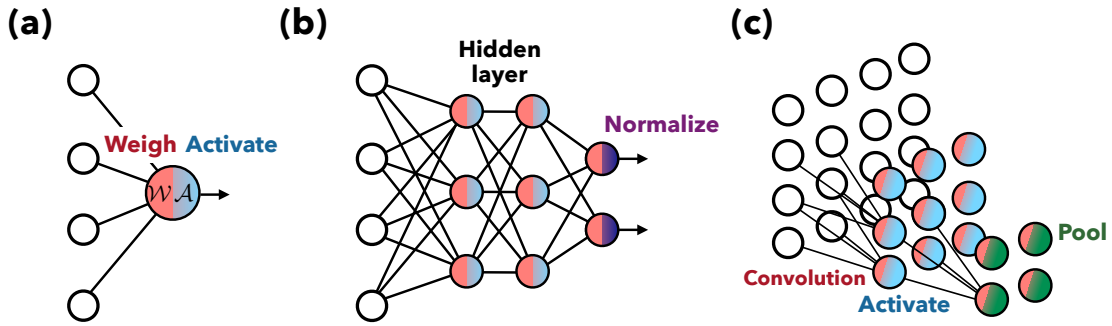

Figure 2.1: Graphical illustration of (a) single perceptron, (b) multilayer perceptron (MLP), and (c) a layer of convolutional neural network (CNN). A single perceptron first sums up the weighted input, and then operates the non-linear activation function to return the output. The MLP, which consists of many layers with such units, would in general have another type of activation function in the last layer. A CNN also consists of the weighing and activation operations, which is often subsequently passed to the pooling layer.

cessed to obtained the output from the next layer, $\mathbf{y}^{(m)}$, as

$$\begin{aligned} \mathbf{y}^{(m)} &= \mathcal{A}_m(\mathbf{z}^{(m)}) = \mathcal{A}_m \circ \mathcal{W}_m(\mathbf{y}^{(m-1)}), \\ z^{(m)} &= \left(\mathcal{W}_m(\mathbf{y}^{(m-1)})\right)_j = \sum_i W_{ji}^{(m)} y_i^{(m-1)} + b_j^{(m)}, \\ \left(\mathcal{A}_m(\mathbf{z}^{(m)})\right)_j &= A^{(m)}(z_j^{(m)}), \end{aligned} \tag{2.5}$$

where $W^{(m)}$ and $b^{(m)}$ are the weight and bias for the m-th layer and $A^{(m)}$ is the activation function.

One of the appreciated properties of the neural network is undoubtedly its expressive power. As long as the activation is not polynomial function, the function with at least one hidden layer is known to be capable of approximating arbitrary nonlinear function by increasing the number of hidden neurons [85–87][*4].

2.1.2 Convolutional Neural network

Computer scientists have become aware that the correlation in the visionary data should be explicitly extracted to perform better classification. This lead to

[*4]It is notable that although the MLP with a small number of hidden layers are capable of expressing arbitrary functions, the required number of hidden neurons becomes exponentially larger compared to those for the deep-layered MLPs.

the proposal of the **convolutional neural network (CNN)** [88, 89]. Ordinary type of a CNN consists of the *convolution* and *pooling* operations in addition to the activation and the ordinary weighing operations.

Given a d-dimensional array $X = (x_1, ..., x_d) \in \mathbb{R}^{N_1} \times \cdots \times \mathbb{R}^{N_d}$, the convolution operation $\mathcal{C}$ can be is given as[*5]

$$(\mathcal{C}(X))_{i_1,...,i_d} = \sum_{m_1,...,m_d} X_{i_1+m_1,...,i_d+m_d} K_{m_1,...,m_d}, \tag{2.6}$$

where the kernel K is equivalent to translationally-symmetric weighing. The subscripts denote the elements of the high-dimensional arrays. The sparcity of the interaction and translation symmetry is understood to help the machine to extract features efficiently. As in the MLP, one may also prepare multiple convolution filters that simultaneously operates on an input. Note that the convolution operation is usually followed by the activation operation as is shown in Fig. 2.1(c). We therefore refer to a set of convolution and activation as the convolution layer.

The pooling, on the other hand, is often considered to introduce an operation that "summarizes" the statistics of the nearby outputs. An example is the max pooling that operates on an input X as

$$(\mathcal{P}(X))_{i_1,...,i_d} = \max_{(m_1,...,m_d)} \{X_{i_1+m_1,...,i_d+m_d}\}. \tag{2.7}$$

While Eq. (2.7) assumes a single "sheet" of input, it can be modified to take more than one of them. For instance, one may consider max pooling concerning all the filters that is calculated by the convolution layer.

In an ordinary CNN structure, the output from the layers of convolution and pooling are passed to fully-connected units which yield the final classification result. For instance, a network structure named the VGG, which was proposed in Ref. [90], repeats the pooling per two or three layers of convolution, and connect to the fully-connected layers with the subsequent softmax function.

The network structure of the CNN is not only understood to be suitable with image recognition, but also expected to capture quantum entanglement due to the exponential growth of entanglement entropy with respect to the number of layers when the pooling is absent [91].

[*5] Important notions in practical application are the **stride** and **padding**. A convolution (or a pooling) with stride k concerns the operation for every k pixels. Namely, it denotes the translation of the kernel. The padding, on the other hand, refers to the value of the pixels *outside* the image when the number of the pixels and the kernel are not commensurate.

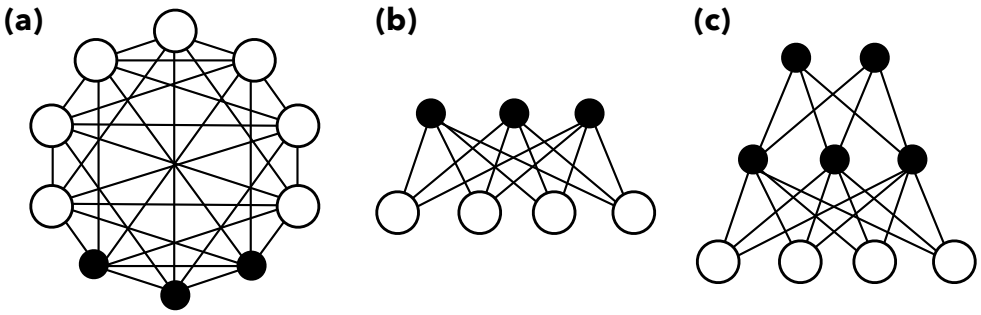

Figure 2.2: (a) Boltzmann machine with generic structure, (b) restricted Boltzmann machine (RBM) which has a bipartite structure, and (c) deep Boltzmann machine (DBM) with multiple layers of hidden spins. The white (black) circles denote the visible (hidden) spins and the black lines correspond to non-zero interaction between spins.

2.2 Machines for Representation

In contrast to the classification task in which one constructs non-linear separation criteria between data, the objective of the representation task is to obtain a low-dimensional representation of some probability distribution that approximates or exactly represents the given dataset or the physical model. The machines for this task is referred to as the generative model in the machine learning community. The high expressive power of the artificial neural networks is also capable of the representation task. As in the classification task, we introduce the most vanilla type among such models – the Boltzmann machine (BM). The machine is employed for exact representation in Chapter 4 and approximate representation in Chapter 5.

2.2.1 Boltzmann machines

The BM is an artificial neural network which expresses a canonical distribution reflecting the virtual energy computed from the configuration of local variables in the system. Although the local variables are allowed to be taken as either discrete or continuous, here we restrict our discussion to the former for simplicity[*6]. BMs were originally introduced to approximate (or estimate) the likelihood

[*6]Two of variable types are discriminated by the terms "Gaussian" and "Bernoulli." For example, a model with continuous visible variables and discrete hidden variables are called "the

distribution that best fits (or explains) a given dataset consisting of binary variables [7, 92].

In the following, we define the BM as a likelihood distribution[*7] for a set of N_v binary degrees of freedom, or the visible spins, $\boldsymbol{\sigma} := (\sigma_1, \dots \sigma_{N_v}) \in \mathcal{S}$ where $\mathcal{S} = \{+1, -1\}^{N_v}$. Concretely, the expression of the BM is given as follows,

$$\pi(\boldsymbol{\sigma}) = \sum_{\boldsymbol{h}} \widetilde{\pi}(\boldsymbol{\sigma}, \boldsymbol{h}) = \sum_{\boldsymbol{h}} e^{-E(\boldsymbol{\sigma}, \boldsymbol{h})}, \tag{2.8}$$

$$-E(\boldsymbol{\sigma}, \boldsymbol{h}) = \sum_{i,j} W_{ij}\sigma_i h_j + \sum_{i,i'} W_{ii'}\sigma_i\sigma_{i'} + \sum_{j,j'} W_{jj'}h_j h_{j'} + \sum_i a_i\sigma_i + \sum_j b_j h_j, \tag{2.9}$$

where the configuration of N_h auxiliary binary degrees of freedom, or the hidden spins, is given as $\boldsymbol{h} := (h_1, \dots, h_{N_h}) \in \mathcal{H}$ where $\mathcal{H} = (+1, -1)^{N_h}$. Here, σ_i and h_j are the i-th visible and j-th hidden spins that are coupled via the 2-spin interaction W_{ij}, $W_{ii'}$ and $W_{jj'}$. In addition, the local magnetic fields are denoted by a_i and b_j for visible and hidden spins, respectively. The graphical representation of the BM is given in general by the undirected graph which depicts the spins as the nodes and the non-zero interactions as the edges. The current thesis also employs such notation. [See Fig. 2.2 for some examples.]

The expressibility of the BM is enhanced by introducing the hidden spins. This is similar to the case in the MLP, in which the increasing number of hidden units enable us to construct a universal approximator which is capable of capturing any complicated correlation between the visible units. Correspondingly, the BM also becomes a universal approximator of likelihood distribution by increasing the number of the hidden spins [93].

Restricted Boltzmann machine The BM with particular structure of connectivity becomes beneficial from, e.g., numerical implementation cost or stackability to form deep layers[*8]. Here, we introduce the **restricted Boltzmann machine (RBM)** which is one of the most widely-known examples due to its simplicity. The RBM has a bipartite structure due to the lack of interactions within the visible layer or the hidden layer, namely $W_{ii'} = W_{jj'} = 0$ in Eq. (2.8). See Fig. 2.2(b) for its graphical representation.

Gaussian-Bernoulli Boltzmann machine."

[*7] This is equivalently the Boltzmann factor in statistical mechanics.

[*8] In fact, the RBM can be used to pre-train the MLP for classification [94, 95]. Namely, one may tune the parameters layer-by-layer by unsupervised training on dataset, which enables the layers to perform feature extraction.

The likelihood distribution given by the RBM is as follows,

$$\pi(\boldsymbol{\sigma}) = \sum_{\boldsymbol{h}} \widetilde{\pi}(\boldsymbol{\sigma}, \boldsymbol{h}) = \sum_{\boldsymbol{h}} e^{-E(\boldsymbol{\sigma}, \boldsymbol{h})} \tag{2.10}$$

$$-E(\boldsymbol{\sigma}, \boldsymbol{h}) = \sum_{i,j} W_{ij}\sigma_i h_j + \sum_i a_i \sigma_i + \sum_j b_j h_j. \tag{2.11}$$

Although the connectivity structure and hence the expression is "restricted" compared to the generic BM, any given likelihood distribution can be approximated with an arbitrary precision by considering exponentially many number of hidden spins [93].

One of the appreciated properties of the RBM originating from its bipartite structure is that the conditional probability distributions $p(\boldsymbol{\sigma}|\boldsymbol{h})$ and $p(\boldsymbol{h}|\boldsymbol{\sigma})$ are factored with respect to the variables. Given a fixed set of variables $\boldsymbol{h}$, the distribution for a visible spin configuration can be written as

$$p(\boldsymbol{\sigma}|\boldsymbol{h}) = \frac{\widetilde{\pi}(\boldsymbol{\sigma}, \boldsymbol{h})}{\sum_{\boldsymbol{\sigma}} \widetilde{\pi}(\boldsymbol{\sigma}, \boldsymbol{h})} \tag{2.12}$$

$$= \prod_i \frac{\exp(\sum_j W_{ij}\sigma_i h_j + a_i\sigma_i)}{\sum_{\sigma_i=\pm 1} \exp(\sum_j W_{ij}\sigma_i h_j + \sigma_i a_i)} = \prod_i p(\sigma_i|\boldsymbol{h}), \tag{2.13}$$

and also the conditional distribution given the hidden spins can be computed in parallel as

$$p(\boldsymbol{h}|\boldsymbol{\sigma}) = \prod_j \frac{\exp(\sum_i W_{ij}\sigma_i h_j + b_j h_j)}{\sum_{h_j=\pm 1} \exp(\sum_i W_{ij}\sigma_i h_j + b_j h_j)} = \prod_j p(h_j|\boldsymbol{\sigma}). \tag{2.14}$$

This is beneficial when we consider Monte Carlo sampling from the distribution π. Namely, we may consider independent sampling for each local variable, and hence expect to draw uncorrelated data if the connectivity of the BM is sufficiently dense.

Deep Boltzmann machine Employing the notion of the layers introduced for the MLP, we may describe the RBM as a model with a single visible layer and a hidden layer. A **deep Boltzmann machine (DBM)**, in contrast, has a multiple layers of latent spins. To be instructive, let us consider another hidden layer on top of the RBM as depicted in Fig 2.2(c). The likelihood distribution of a DBM with M layers is specified by the energy function involving $\boldsymbol{\sigma}, \boldsymbol{h}^{(1)}, \cdots, \boldsymbol{h}^{(M)}$ as

follows,

$$\pi(\boldsymbol{\sigma}) = \sum_{\boldsymbol{h}^{(1)},\ldots,\boldsymbol{h}^{(M)}} \widetilde{\pi}(\boldsymbol{\sigma}, \boldsymbol{h}^{(1)}, \ldots, \boldsymbol{h}^{(M)}) = \sum_{\boldsymbol{h}^{(1)},\ldots,\boldsymbol{h}^{(M)}} e^{-E(\boldsymbol{\sigma},\boldsymbol{h}^{(1)},\ldots,\boldsymbol{h}^{(M)})}, \quad (2.15)$$

$$-E(\boldsymbol{\sigma}, \boldsymbol{h}^{(1)}, \ldots, \boldsymbol{h}^{(M)}) = \sum_{i,j_1} W_{ij_1}\sigma_i h^{(1)}_{j_1} + \sum_{m=1}^{M-1} \sum_{j_m,j_{m+1}} W^{(m)}_{j_m j_{m+1}} h^{(m)}_{j_m} h^{(m+1)}_{j_{m+1}} + \\ + \sum_i a_i\sigma_i + \sum_{m=1}^{M} \sum_{j_m} b^{(m)}_{j_m} h^{(m)}_{j_m} \quad (2.16)$$

where $h^{(m)}_{j_m}$ is the j_m-th spin in the m-th hidden layer with the local magnetic field $b^{(m)}_{j_m}$, and $W^{(m)}_{j_m j_{m+1}}$ is the interaction between the m-th and $(m+1)$-th hidden layers. Note that there is in principle no bound on the number of hidden layers, and one may add as many latent spins as desired.

Complex-valued BM We have discussed the BM with real parameters to ensure the positivity of the likelihood. However, one may introduce complex values to represent complex amplitudes such as the wave function, density matrix, and so on. For example, we consider a spin-1/2 system with its quantum state described by wave function $|\psi\rangle$ by the **complex-valued restricted Boltzmann machine (cRBM)** as

$$\begin{aligned} \langle\sigma|\psi\rangle &= \frac{1}{Z}\sum_{\boldsymbol{h}} e^{-E(\boldsymbol{\sigma},\boldsymbol{h})}, \\ -E(\boldsymbol{\sigma},\boldsymbol{h}) &= \sum_{i,j} W_{ij}\sigma_i h_j + \sum_i a_i\sigma_i + \sum_j b_j h_j, \end{aligned} \quad (2.17)$$

where Z is the normalization that ensures $|\,\langle\psi|\psi\rangle\,| = 1$.

Previous research has shown that the connectivity of the hidden spins to the entire visible spins are beneficial in terms of the quantum entanglement [62]. For instance, let us consider a spin-1/2 chain of length $2L$, and consider an cRBM with $3L-1$ hidden spins which are connected with the visible spins as shown in Fig. 2.3. By taking the network parameters to be as follows,

$$\begin{aligned} W_{ij} &= \begin{cases} \dfrac{\mathbf{i}\pi}{4} & \text{if } j \in \{i, i-1, i+L-1, i+2L-1\}, \\ 0 & \text{otherwise}, \end{cases} \\ a_i &= 0, \\ b_j &= \begin{cases} \dfrac{\mathbf{i}\pi}{4} & \text{if } j \in [1, 2L-1], \\ -\dfrac{\mathbf{i}\pi}{4} & \text{otherwise}, \end{cases} \end{aligned} \quad (2.18)$$

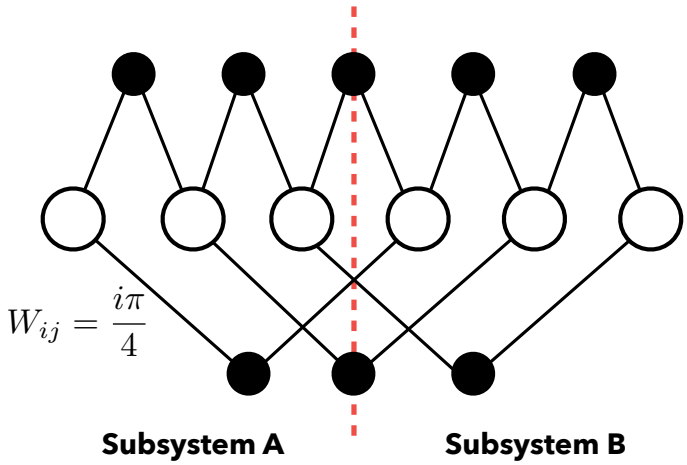

Figure 2.3: Structure of the cRBM that shows maximal amount of entanglement entropy in one-dimensional geometry.

one can show that the Renyi entropy given by the quantum state corresponding to the cRBM is given for arbitrary $\alpha \geq 0$ as

$$S_\alpha^A = L \ln 2, \tag{2.19}$$

where the definition is given as $S_\alpha^A = \frac{1}{1-\alpha} \log(\mathrm{Tr}[\rho_A^\alpha])$ with ρ_A being the reduced density matrix for subsystem A[*9]. This is the maximal value reachable by pure states. For higher dimensional systems with hypercubic geometry, one may also construct a cRBM which shows maximal entanglement by following a similar construction.

[*9]Note that this reduces to the von Neumann entropy when $\alpha \to 1$, and hence corresponds to the ordinary entanglement entropy.

3
Classification of Quantum Phases of Disordered Noninteracting Fermion Systems

In Chapter 2, we have introduced the multilayer perceptron (MLP) that is an versatile and simple machine to perform classification tasks. In this Chapter, we apply the MLP in a supervised manner to classify the quantum phases of noninteracting fermion systems with disorder. To be concrete, we train the MLP to discriminate the quasiparticle distributions of the first excited state in the clean limit, and then test its performance by applying to those obtained from the disordered region. Given the disorder that keeps the discrete symmetries of the ensemble as a whole, translational symmetry, which is broken in the individual quasiparticle distribution, is recovered statistically by taking the ensemble average. Therefore, the quantum phases can be classified by the machine trained in the clean limit. We demonstrate our method by applying it to a model for 2d topological superconductor in class DIII. The result obtained from the MLP is totally consistent with the calculation by other independent methods such as the transfer matrix method or noncommutative geometry approach. If all three phases, namely the $\mathbb{Z}_2$, trivial, and the thermal metal phases, appear in the clean limit, the machine can classify them with high confidence over the entire phase diagram. If only the former two phases are present, we find that the machine remains confused in a certain region, leading us to conclude the detection of the unknown phase which is eventually identified as the thermal metal phase.

3.1 Background

Bulk-gapped phases of noninteracting fermions can be classified based on the topology of the band structures. The symmetry class specified by the presence of three symmetries, namely the particle-hole symmetry, time-reversal symmetry, and chiral symmetry, and also the spatial dimension determines the possi-

	T	P	S	1d	2d	3d	4d	5d	6d	7d	8d
A	0	0	0	0	Z	0	Z	0	Z	0	Z
AIII	0	0	1	Z	0	Z	0	Z	0	Z	0
AI	1	0	0	0	0	0	Z	0	Z_2	Z_2	Z
BDI	1	1	1	Z	0	0	0	Z	0	Z_2	Z_2
D	0	1	0	Z_2	Z	0	0	0	Z	0	Z_2
DIII	-1	1	1	Z_2	Z_2	Z	0	0	0	Z	0
AII	-1	0	0	0	Z_2	Z_2	Z	0	0	0	Z
CII	-1	-1	1	Z	0	Z_2	Z_2	Z	0	0	0
C	0	-1	0	0	Z	0	Z_2	Z_2	Z	0	0
CI	1	-1	1	0	0	Z	0	Z_2	Z_2	Z	0

Table 3.1: Periodic table for topological insulators and superconductors [112, 113]. The ten symmetry classes are labeled by the notation of Altland and Zirnbauer [114], reflecting the presence or absence of time-reversal symmetry T, particle-hole symmetry P, and chiral symmetry $C = PT$. The values ± 1 and 0 denote the presence and absence of symmetry, where the signs specifying the value of T^2 and P^2. The topological classifications, i.e., Z, Z_2, and 0, show a regular pattern that repeats when $d \to d + 8$. In the current work, we consider a 2d system in class DIII, and hence gapped phases can be classified by a Z_2 invariant.

ble topological invariant in the system. See Table 3.1 for the correspondence between the symmetry class and the topological invariants. Although topological invariants in translationally invariant systems have been well studied including their concrete expressions and calculations [96–100], the investigation of disordered system is not only nontrivial since the wave number used for calculation of topological invariant is no longer a good quantum number, but also significant because of its connection with the real materials. The definition for infinite systems under disorder has been provided by Katsura and Koma [101, 102], and validity of numerical approach has been verified in limited number of symmetry class [103–111]. It is not straightforward, however, to extend such methods to topological crystalline insulators and higher-order topological insulators/superconductors since the approach concerns the extension of the definitions.

Motivated by such a situation, we develop a new method to determine the phase diagram of topological insulator/superconductor under finite disorder by

applying the MLP trained to discriminate the quantum phase **only in the clean limit**. The underlying key concept is the recovery of the translational symmetry by ensemble average. While the translational symmetry is broken in a system with disorder such as a random potential [115], as an ensemble of disorder average the symmetry is *statistically recovered*.

As a demonstration of our approach, we consider a model of topological superconductor with 2d noncentrosymmetric geometry to show that the MLP learned from the data in the clean limit is capable of classifying such ensemble averaged states. The phase diagram obtained from our method is fully consistent with the results in both the transfer matrix (TM) method [116] and the calculation of a $\mathbb{Z}_2$ index by noncommutative geometry which was recently proposed [101, 102, 111][*1]. We argue that the current approach is numerically advantageous compared to the above-mentioned methods from the perspective of the variety of applicable models; the transfer matrix method becomes inefficient when multiple phase boundaries approach each other and the noncommutative geometry approach is ill-defined when both the bulk and mobility gap is closed. We see that the well-trained MLP is capable of both difficulties when the translation symmetry is statistically recovered in the data.

The rest of this chapter is organized as follows. In Sec. 3.2 we provide the method to map out the phase diagram. The Hamiltonian for 2d noncentrosymmetric superconductor in class DIII with and without the disorder is introduced here. Next, in Sec. 3.3, we discuss the architecture, input, and output of the MLP. Also, we provide the supervised learning scheme which optimizes the parameters of the MLP to give appropriate classification labels. In Sec. 3.4 we show the results obtained by performing both ternary and binary classification with the MLP, comparing to those by other two methods. Finally, the summary for the current chapter and the discussion on the future direction is given in Sec. 3.5. For completeness, we describe optimization method of the cost function in Appendix A. In Appendices B and C, the other two methods to depict the phase diagram are provided.

[*1] Other options include the scattering matrix theory as in Ref. [117] or the Chalker-Coddington model as in Ref. [118].

3.2 Model

Topological superconductors exhibiting the gapless edge modes have been attracting keen interest, since the excitation can be described by the Majorana fermion, which is expected to be a candidate for topological qubit in quantum computation [119, 120]. For class DIII, in particular, the formulation of Niu-Thouless-Wu, an extension to many-body systems and disordered systems [103], is known to break down. The recent proposal of the candidate materials such as $Cu_xBi_2Se_3$ [121, 122] and $FeTe_xSe_{1-x}$ [11, 123, 124] further motivates one to investigate the quantum phase diagram of two-dimensional (2d) noncentrosymmetric superconductor in class DIII with disorder.

In the current thesis, we choose the model for 2d topological superconductor in class DIII for a demonstration of our approach. Inspired by the recent discovery of candidate materials that breaks the inversion symmetry, we assume the presence of both *s*- and *p*- wave couplings.

3.2.1 Bogoliubov-de Gennes Hamiltonian in real space

The Bogoliubov-de Gennes Hamiltonian H for 2d noncentrosymmetric superconductor in class DIII is given in the real space as [125]

$$
\begin{aligned}
H &= H_0 + H', && (3.1)\\
H_0 &= \sum_{\mathbf{r}} \sum_{k=1,2} \Psi_{\mathbf{r}}^\dagger t_k \Psi_{\mathbf{r}+\mathbf{e_k}} + \text{h.c.} + \sum_{\mathbf{r}} \Psi_{\mathbf{r}}^\dagger v \Psi_{\mathbf{r}}, && (3.2)\\
H' &= \sum_{\mathbf{r}} \Psi_{\mathbf{r}}^\dagger V_{\mathbf{r}} \Psi_{\mathbf{r}}, && (3.3)
\end{aligned}
$$

where H_0 is the Hamiltonian in the clean limit and H' corresponds to the disorder. The Nambu operator is denoted as $\Psi_{\mathbf{r}} = [c_{\mathbf{r}\uparrow}, c_{\mathbf{r}\downarrow}, c_{\mathbf{r}\uparrow}^\dagger, c_{\mathbf{r}\downarrow}^\dagger]^T$ where $c_{\mathbf{r}\alpha}$ is an annihilation operator of an electron with spin α at site $\mathbf{r}$. For concreteness, we define our model on a square lattice with cylindrical boundary conditions. This leads us to define the 4×4 matrices in Eqs. (3.2) and (3.3) as follows,

$$
\begin{aligned}
t_1 &= t s_3 \otimes \sigma_0 + \frac{i\Delta}{2} s_1 \otimes \sigma_3, && (3.4)\\
t_2 &= t s_3 \otimes \sigma_0 + \frac{\Delta}{2} s_1 \otimes \sigma_3, && (3.5)\\
v &= -\mu s_3 \otimes \sigma_0 - \Delta_2 s_2 \otimes \sigma_2, && (3.6)\\
V_{\mathbf{r}} &= (w_{\mathbf{r}} s_3 \otimes \sigma_0), && (3.7)
\end{aligned}
$$

where $t_{1(2)}$ and $\mathbf{e}_{1(2)}$ are the hopping matrix and the primitive vector along the $x(y)-$direction with the transfer integral t and the helical p-wave coupling Δ. The Pauli matrices s_k and σ_k (k = 0,1,2,3) operate on the particle-hole and spin space, respectively. The on-site term, v, consists of the chemical potential μ and the s-wave pairing Δ_2. The mixture of the spin-singlet and the spin-triplet pairings are caused by the broken inversion symmetry. Although the square lattice is considered in the effective model, i.e. Eq. (3.1), we assume that the underlying crystal structure of the original Hamiltonian breaks inversion symmetry. The randomness is introduced as a on-site random potential $V_{\mathbf{r}}$ with its amplitude distributed independently with respect to the site $\mathbf{r}$ and also uniformly within the width w as $w_{\mathbf{r}} \in [-w/2, w/2]$.

It is easy to confirm that the following symmetries are present in the Hamiltonian: even particle-hole symmetry, odd time-reversal symmetry, and chiral symmetry. In the presence of such discrete symmetries, the system can be classified as the class DIII according to the classification by Altland and Zirnbauer [114, 126]. The topological property of a translationally symmetric 2d system under such class is known to be characterized by the $\mathbb{Z}_2$ topological invariant. The formula for the topological invariant, ν, for systems with occupied 2χ-bands was found by Kane and Mele as follows [98, 99, 112, 113, 127, 128],

$$(-1)^{\nu} = \prod_{i=1}^{4} \frac{\mathrm{Pf}[\omega(\Lambda_i)]}{\sqrt{\det[\omega(\Lambda_i)]}}. \tag{3.8}$$

The antisymmetric $2\chi \times 2\chi$ matrix ω, which is called as the "sewing matrix," is defined using the Bloch wave functions, $\{|u_{\alpha,\mathbf{k}}\rangle\}$, and the time-reversal operator, Θ, as

$$\omega_{\alpha\beta}(\mathbf{k}) = \langle u_{\alpha,-\mathbf{k}}|\Theta|u_{\beta,\mathbf{k}}\rangle\,, \tag{3.9}$$

where α and β denote the band indices. Here, Pf is the Pfaffian defined for a $2\chi \times 2\chi$ antisymmetric matrix A as

$$\mathrm{Pf}[A] = \frac{1}{2^{\chi}\chi} \sum_{s \in S_{2\chi}} \mathrm{sgn}(s) \prod_{i=1}^{\chi} A_{s(2i-1),s(2i)}, \tag{3.10}$$

where $S_{2\chi}$ is a permutation group and $\mathrm{sgn}(s)$ gives the sign of a permutation s. The Pfaffian is related with the determinant, or det, as $\mathrm{Pf}[A]^2 = \det[A]$. Using the formula given in Eq. (3.8), we find that the system in the clean limit, i.e., $w = 0$, is in $\mathbb{Z}_2$ phase at $2 - 2\sqrt{1-(\Delta_2/\Delta)^2} < |\mu| < 2 + 2\sqrt{1-(\Delta_2/\Delta)^2}$ if $|\Delta_2/\Delta| < 1$.

Once the disorder is turned on, the wave number is no longer a good quantum number and thus the formula for the Kane-Mele invariant is no longer applicable. It is known that moderate randomness in spin-rotational symmetry broken system may cause destructive interference of time-reversal paths of the quasiparticle, suppressing the back scattering and thereby leading the system to show metallic behavior (weak-antilocalization) in 2d [129–131]. In particular, "insulator-metal" transition from the $\mathbb{Z}_2$ phase, in which Majorana fermions pinned to the disorder percolates, gives rise to the bulk-gap closed phase which is often referred to as the Majorana metal phase [132]. In the 2d, the thermal conductivity grows logarithmically with the system size, which is understood as a consequence of the extended behavior of the quasiparticle over the whole system. Actually, the metallic property of thermal transport arises also when the bulk gap is closed in the clean limit. Thus, all of these will be collectively referred to as the thermal metal (ThM) phase in the following.

3.3 Training the machine

In the current section, we introduce the classification scheme based on the statistical recovery of symmetry to discriminate the quantum phases of noninteracting fermions. We first argue that the disorder average of the spacial distribution of the quasiparticle qualifies as the input for classification task. After introducing the architecture of the MLP, we define the cost function and the optimization method to train the machine.

3.3.1 Input data for machine

Adopted as the input data $\mathbf{x}$ is the disorder average over N_r realizations of the spacial distribution of the quasiparticle, $P(\mathbf{r})$, corresponding to the first excited state. Our expectation is that the qualitatively different behavior of the quasiparticle gives the machine sufficient information to discriminate phases. The bulk-edge correspondence in the $\mathbb{Z}_2$ phase, for instance, assures the robust edge-localization of the low-lying states across the zero energy. Furthermore, the behaviours in other two phases, namely the bulk-localization in the trivial phase and the delocalization of the quasiparticle over the system due to the bulk gap closing in the ThM phase, encourage us to consider $P(\mathbf{r})$ for the lowest excitation as an appropriate input for the machine.

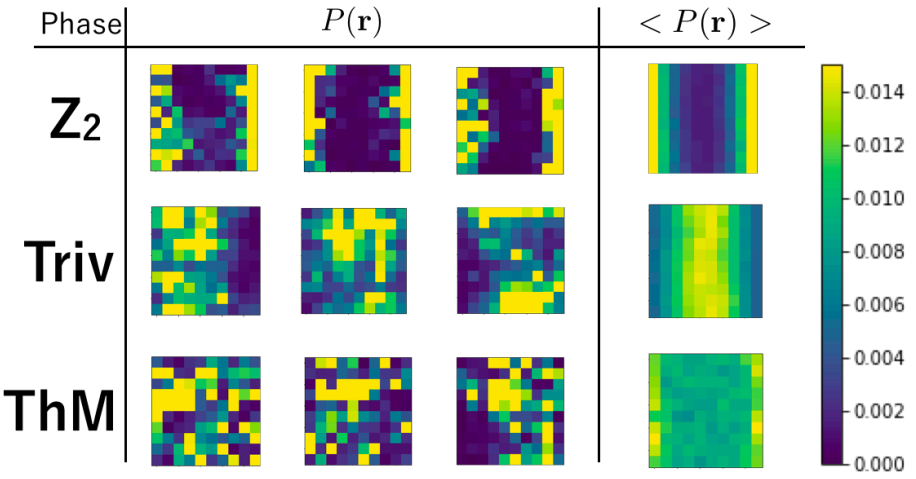

Figure 3.1: Typical single-shot quasiparticle distribution of the first excited state, $P(\mathbf{r})$, and its disorder average, $\langle P(\mathbf{r})\rangle$, over 500 realizations of random configurations. The parameters are taken from deep inside the phases as $(\mu, w) = (2,9), (6,5), (2,18)$ with $\Delta = 3$ and $\Delta_2 = 0$ from the top. The system size is taken as 10×10.

Let us consider the eigenstate $|\psi\rangle$ satisfying $H|\psi\rangle = E_1|\psi\rangle$ with the lowest $E_1 > 0$. The degeneracy, if exists, is lifted up to time-reversal symmetry, and the two states are identical in terms of the quasiparticle distribution, namely,

$$P(\mathbf{r}) = |\psi^e_\uparrow(\mathbf{r})|^2 + |\psi^e_\downarrow(\mathbf{r})|^2 + |\psi^h_\uparrow(\mathbf{r})|^2 + |\psi^h_\downarrow(\mathbf{r})|^2, \tag{3.11}$$

where the super(sub)script denotes the degree of freedom in the Nambu (spin) space. Some examples of single disorder realization $P(\mathbf{r})$ and its disorder average $\langle P(\mathbf{r})\rangle$ for $N_r = 500$ are shown in Fig. 3.1.

While it is difficult to find evident pattern in respective $P(\mathbf{r})$ due to the randomness, we expect that the translational symmetry is *statistically recovered* by taking the disorder average. For instance, the bulk-edge correspondence assures the Majorana edge mode in the $\mathbb{Z}_2$ phase, which is robust against perturbation unless the bulk gap closes. The quasiparticle is localized at the edge although the amplitude of $P(\mathbf{r})$ may become uneven along the circumference of the cylinder under spacial inhomogeneity. Such a fluctuation is eliminated by considering $\langle P(\mathbf{r})\rangle$, which we confirm from the top row of Fig. 3.1. Furthermore, the localization in the bulk for the middle row indicates the thermal insulating property of the trivial phase, and the extension of the quasiparticle over the whole system in the bottom row reflects the metallic behavior of the ThM.

Therefore, we classify the phases by feeding $\langle P(\mathbf{r})\rangle$ to the ANN which learned the labels of $P(\mathbf{r})$ in the clean limit. Both binary and ternary classification are considered.

3.3.2 Network structure of machine

As the machine for the classification task, we employ the MLP that performs K-class discrimination with simply two hidden layers. The output from the machine, which is graphically described in Fig. 3.2, is given as

$$\mathbf{y} = \mathcal{A}_3 \circ \mathcal{W}_3 \circ \mathcal{A}_2 \circ \mathcal{W}_2 \circ \mathcal{A}_1 \circ \mathcal{W}_1(\mathbf{x}), \tag{3.12}$$

where the input $\mathbf{x} \in \mathbb{R}^N$ is a N-dimensional vector, the output $\mathbf{y} \in \mathbb{R}^K$ is normalized so that $\sum_k y_k = 1$, and $\mathcal{W}_i(\mathcal{A}_i)$ is the weighing (activation) operation on the i-th layer. It is instructive to recall that, given the number of neurons in the i-th layer as N_i, the explicit form of $\mathcal{W}_i : \mathbb{R}^{N_i} \to \mathbb{R}^{N_{i+1}}$ is given as

$$\left(\mathcal{W}_i(\mathbf{x})\right)_j = \sum_{k=1}^{N_i} W_{jk}^{(i)} x_k + b_j^{(i)}, \tag{3.13}$$

where $W_{jk}^{(i)}$ is the weight of output from the k-th neuron in the i-th layer passed to the j-th neuron in the next layer, and $b_j^{(i)}$ denotes the bias term. For the activation function of the hidden and output layers, we consider the Rectified Linear Unit (ReLU) and the Softmax function, respectively. The explicit expression of the nonlinear functions on a given real vector $\mathbf{z}$ is given as

$$\mathcal{A}_i(\mathbf{z}) = \begin{cases} \mathrm{ReLU}(\mathbf{z}) = \{\max(0, z_j)\}_{j=1}^{\dim(\mathbf{z})} & \text{if } i = 1, 2, \\ \mathrm{Softmax}(\mathbf{z}) = \left\{\dfrac{\exp(z_j)}{\sum_i \exp(z_i)}\right\}_{j=1}^{\dim(\mathbf{z})} & \text{if } i = 3, \end{cases} \tag{3.14}$$

where z_j denotes the j-th element of the vector $\mathbf{z}$ and $\dim(\mathbf{z})$ is the dimension of the vector. Note that the sum of the output is normalized to be unity, which enables us to interpret as the "confidence" of the prediction. The use of ReLU function is based on the principle that the machines are easier to optimize if their behavior is closer to linear [7].

3.3.3 Cost function

In the following, we introduce the cross-entropy between the training data and the prediction of the machine, which is frequently used as the cost function

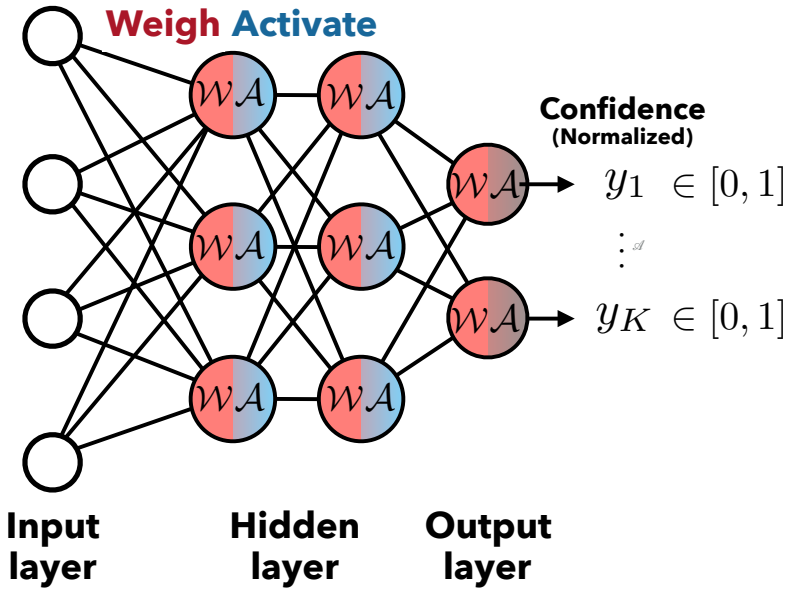

Figure 3.2: The architecture of a feedforward artificial neural network with two hidden layers, at which the input data is compressed to extract some abstract feature for classification. The activation of the output layer is the Softmax function so that the sum is unity, allowing us to interpret as the confidence of the machine. We employ an MLP with two hidden layers containing 50 and 40 neurons, respectively.

for multi-label classification [7, 133]. This is closely related with the minimization of the dissimilarity between the empirical distribution defined by the training set and the model prediction measured by the Kullback-Leibler (KL) divergence, which is widely applied in the statistics community.

To see that the cross entropy is appropriate as the cost function, let us first consider the KL divergence D_{KL} between single-component probability distributions $p(\mathbf{x})$ and $q(\mathbf{x})$ as

$$D_{\mathrm{KL}}(p||q) = \int d\mathbf{x} p(\mathbf{x}) \log \frac{p(\mathbf{x})}{q(\mathbf{x})}, \tag{3.15}$$

which has nice properties such as the non-negativity, i.e., it becomes 0 if and only if $p = q$ [*2]. Let us assume p to be an empirical distribution $\hat{p}$ given by a dataset

[*2]Note that due to the assymetry between the two distributions, KL divergence does not qualify as a distance metric in a mathematical sense.

$\mathcal{D} = \{\hat{\mathbf{x}}_i\}$ as

$$\hat{p}(\mathbf{x}) = \frac{\sum_{\hat{\mathbf{x}}\in\mathcal{D}} \delta(\mathbf{x}-\hat{\mathbf{x}})}{|\mathcal{D}|}. \tag{3.16}$$

We take the other probability distribution q to be the parametrized prediction by the machine, and hence explicitly rewrite as q_θ where θ denoting the parameters. The minimization of Eq. (3.15) can be done by considering the optimization of some cost function C_θ defined as

$$C_\theta = -\frac{1}{|\mathcal{D}|}\sum_{\hat{\mathbf{x}}\in\mathcal{D}} \log q_\theta(\hat{\mathbf{x}}), \tag{3.17}$$

where $|\mathcal{D}|$ denotes the number of data. It is clear that Eq. (3.17) is the cross entropy $H(\hat{p}, q_\theta) = -\int d\mathbf{x}\hat{p}(\mathbf{x})\log q_\theta(\mathbf{x})$ or alternatively the negative log likelihood.

Quantification of "distance" between the prediction by a classification machine and training data can be done for multi-label data in a parallel way. Let a dataset be $\mathcal{D} = \{\hat{\mathbf{x}}_i, \hat{\mathbf{y}}_i\}$ where $\hat{\mathbf{x}}_i$ is the i-th input data with its label $\hat{\mathbf{y}}$ given as the K-dimensional one-hot vector, which is a vector with only one of its element unity while others set to zero. Concretely, the k-th element of the one-hot vector for the i-th data is $\hat{y}_i^{(k)} = \delta_{\hat{k}_i,k}$ if the data is labeled as the $\hat{k}_i$-th class. We may extend Eq. (3.17) to K-class case as

$$\begin{aligned} C_\theta &= -\frac{1}{|\mathcal{D}|}\sum_i \log y_\theta^{(\hat{k}_i)}(\hat{\mathbf{x}}_i) \\ &= -\frac{1}{\mathcal{D}}\sum_{(\hat{\mathbf{x}}_i,\hat{\mathbf{y}}_i)\in\mathcal{D}}\sum_k \hat{y}_i^{(k)}\log y_\theta^{(k)}(\hat{\mathbf{x}}_i), \end{aligned} \tag{3.18}$$

where $y_\theta^{(k)}(\hat{\mathbf{x}}_i)$ is the k-th element of the output vector from the parametrized machine which takes the i-th input $\hat{\mathbf{x}}_i$. In actual calculation, we also include the regularization term as

$$C_\theta = -\frac{1}{\mathcal{D}}\sum_{(\hat{\mathbf{x}}_i,\hat{\mathbf{y}}_i)\in\mathcal{D}}\sum_k \hat{y}_i^{(k)}\log y_\theta^{(k)}(\hat{\mathbf{x}}_i) + \lambda\sum_{n=1}^{(\#\text{layers})}|\mathcal{W}^{(n)}|^2. \tag{3.19}$$

where the second term, or the L2 regularization, is the sum over the squared value of all the weight and bias parameters. Suppression of the amplitudes of the weight parameters is commonly considered to prevent the machine from overfitting to the training data. The parameters are updated by mini-batch gradient descent with batch size 40 as $\theta \to \theta - \eta\,(\partial C_\theta/\partial\theta)$, where η is the learning rate that is controlled by the AdaGrad method to efficiently reach the global minimum [134]

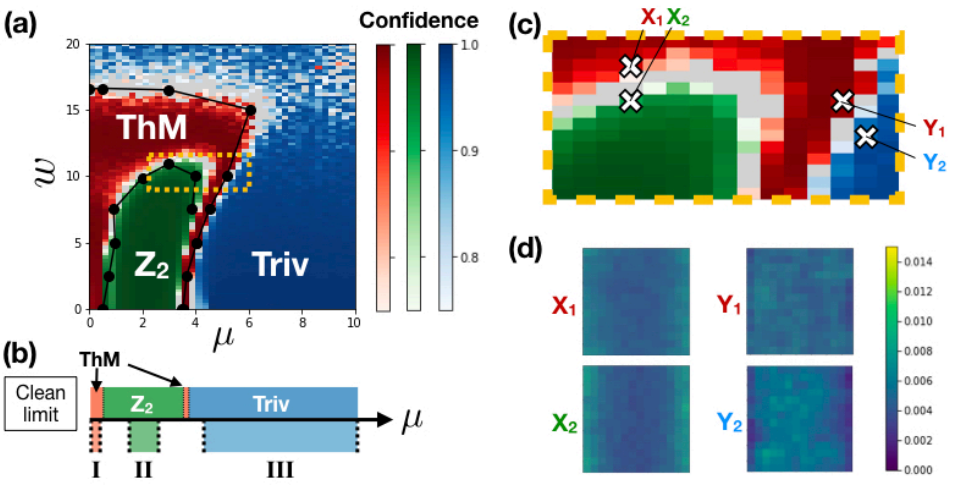

Figure 3.3: (a) Average outputs of 200 ternary-classifying MLPs trained with the clean-limit data for $t = 1, \Delta = 3, \Delta_2 = 2$. The color of each point (μ, w), denoting the chemical potential and the amplitude of the uniformly distributed random potential, indicates the confidence for the thermal metal (red), $\mathbb{Z}_2$ (green), and trivial (blue) phase. The machine is highly confident of each phase but confused at the boundary. The black dots are the phase boundary given by the TM method. (b) The parameter μ of 1000 training data with system size 14×14 is uniformly distributed within I: $[0.0, 0.3]$, II: $[1.0, 2.5]$, and III: $[4.0, 10.0]$. During the training scheme, the network is tested by the data generated along $\mu \in [0.0, 10.0]$ in the clean limit, resulting in accuracy over 90%. (c) Enlargement of the region surrounded by the orange dotted line in (a). (d) The averaged inputs $\langle P(\mathbf{r}) \rangle$ for $N_r = 500$ in the vicinity of the boundaries. The parameters (μ, w) are given as X_1:$(3, 11.5)$, X_2:$(3, 10.75)$, Y_1:$(5.25, 10.5)$, Y_2:$(5.5, 10)$.

and the derivative $\partial C_\theta / \partial \theta$ is computed by the back-propagation method [135]. The details on the optimization scheme is provided in Appendix A. The drop-out method is also applied to avoid overfitting [136].

3.4 Results

In the current section, we discuss the result of the classification of disordered quantum phase of class DIII topological superconductor by the MLP trained only in the clean limit. We consider both the ternary classification, i.e., a case in which all three of the phases are present in the clean limit., and also the binary classifica-

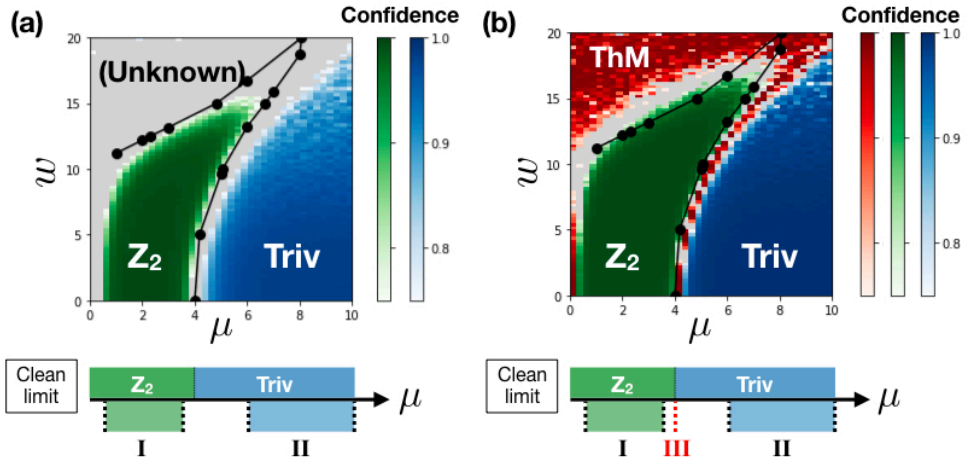

Figure 3.4: Average output of 200 binary-classifying s trained with the clean-limit data for $t = 1, \Delta = 3, \Delta_2 = 0$. The parameter μ of 1000 training data with system size 14×14 is uniformly distributed within (a) I: $[0.5, 3.5]$ and II: $[6.0, 10.0]$, (b) I, II, and III: $\mu = 0.0, 4.0$, each corresponding to the $\mathbb{Z}_2$ (green), the trivial (blue) phase and the critical point (red). The performance of the machine is monitored with the test data generated at $\mu \in [0.0, 10.0]$ in the clean limit, resulting in over 95% accuracy. The outputs above 0.75 for $\langle P(\mathbf{r}) \rangle$ with N_r = 500 are indicated by the depth of the color, and merely gray for below 0.75.

tion, namely only two phases in the clean limit. The classification by the MLP is shown to be consistent with other independent methods. Finally, we compare the output from the MLPs which take data with and without the statistical recovery of symmetry.

3.4.1 Ternary classification

First, we carry out the ternary classification at finite Δ_2. For $|\Delta_2| < |\Delta|$, the bulk gap is closed when (i) $|\mu| < 2 - 2\sqrt{1 - (\Delta_2/\Delta)^2}$ or (ii) $2 + 2\sqrt{1 - (\Delta_2/\Delta)^2} < |\mu| < 4\sqrt{1 - (\Delta_2/\Delta)^2/2}$, and the system shows metallic behavior. [117, 125] We focus on $\Delta = 3, \Delta_2 = 2$ and feed three phases, namely the $\mathbb{Z}_2$, trivial and ThM, to the machine, expecting to predict the whole phase with high confidence. Shown in Fig. 3.3 (a) is the average output of 200 MLPs which takes $\langle P(\mathbf{r}) \rangle$ with N_r =500 as the input. Each MLP is trained independently in a stochastic manner using the data from the clean limit indicated in Fig. 3.3(b). Only the region $\mu \geq 0$ is shown since the phase diagram is symmetric with respect to $\mu = 0$. The black dots are

the transition points obtained from the reliable TM method, which becomes numerically inefficient when multiple phase boundaries approach as in the region between the $\mathbb{Z}_2$ and trivial phases. [See Appendices A and B for details of other two methods.] Remarkably the machine has successfully learned their characteristics even in the vicinity of the phase boundaries and fully extended the phase diagram in the entire region. As is obvious from Figs. 3.3(c)-(d), classifying X_1 and X_2, or Y_1 and Y_2, with a comparable precision is beyond our cognitive ability.

Next, let us focus along $\mu = 2$. In the clean limit, the system is in the $\mathbb{Z}_2$ and enters the ThM and trivial phase sequentially by increasing the disorder, which is accurately captured by the MLP. The blurred output at $w \sim 15$ between the ThM and trivial phases is attributed to the larger fluctuation of the data, which is suppressed by increasing N_r. Other $\mathbb{Z}_2$-ThM and ThM-trivial phase boundaries are nicely reproduced.

Furthermore, the weak disorder region between the $\mathbb{Z}_2$ and the trivial phase at $\mu \sim 3.5$ is unambiguously classified as the ThM. Let us emphasize again that this is attributed to the statistical recovery of the translational symmetry in the input data. As we see in Sec. 3.4.3, merely taking the average of the output is insufficient. Note that such close parallel boundaries require extra effort on the other two methods; determining the peak of the localization length, which diverges with the system size, by the TM becomes difficult due to the broadening by the finite-size effect, and that the noncommutative geometry approach does not work for critical phases.

3.4.2 Binary classification

To examine the binary classification by the MLP, we consider $\Delta_2 = 0$ at which the ThM phase is absent in the clean limit. The quasiparticle distributions are generated at $\mu \in [0.5, 3.5]$ and $[6.0, 10.0]$ for the $\mathbb{Z}_2$ and trivial phase, respectively. The result is shown in Fig. 3.4. As is expected, the machine reproduces the $\mathbb{Z}_2$-trivial phase boundary not only in the clean limit, i.e., the transition point $\mu = 4$, but also at $w > 0$ which is obtained by the TM and the noncommutative geometry approach. At larger disorder, the phase boundaries approach each other. Therefore, machine is confused, i.e, the output remains far below 1, by the finite-size effect, resulting in the small estimation of the $\mathbb{Z}_2$ phase.

The drop of confidence along $\mu = 0$ is also observed. This is understood as $\mathbb{Z}_2 - \mathbb{Z}_2$ transition line, which is consistent with the analysis of the staggered

fermion model for class D. [137] Note that, such a transition that lacks the change in the size dependence on the thermal conductivity or localization length is very difficult to detect even by the TM method.

The most remarkable confusion appears above the $\mathbb{Z}_2$ phase, e.g. $\mu = 5$, which clearly suggests phase transition. [See the gray region in Fig. 3.4(a).] While the output in the trivial phase at small disorder is close to unity, we observe that the confidence in the gray region is far below 1 regardless of the number of average for input or the machine. Such a confusion implies the qualitatively different feature from the trivial phase, namely, the consequence of entering a completely different phase. As was the case in $\Delta_2 > 0$ and also from the argument of the nonlinear sigma model [130, 131], we expect this region corresponds to the thermal metal phase. To reinforce this argument, we add two critical points , i.e., $\mu = 0$ for the $\mathbb{Z}_2 - \mathbb{Z}_2$ and $\mu = 4$ for the $\mathbb{Z}_2-$trivial transition points, as the third label. Figure 3.4(b) shows that the extended behaviour of the quasiparticle is detected by the MLP: the finite w regions at $\mu = 0$ and inbetween the $\mathbb{Z}_2$ and trivial phase, which are naturally expected to be critical lines, and the previously confused region above the $\mathbb{Z}_2$ phase. Here, the machine only have access to the real-space density of the quasiparticle and hence mistakenly identifies the thermal metal phase with the critical regime. Although the two regimes have completely different physical property such as the thermal transport, the machine cannot provide the correct classification without physical properties reflecting such a difference, e.g. the energy spectra or transport property. The region above the $\mathbb{Z}_2$ phase, which we confirm to be the thermal metal from its energy spectra, is expected to be distinguished by a machine trained with such additional information. It is noteworthy that the $\mathbb{Z}_2$-ThM phase boundary predicted by the machine is quantitatively consistent with the result by the numerical calculation of TM.

3.4.3 Single-shot and averaged data

In the following, we see that the success by the MLP is attributed to the recovery of symmetry, but not merely by the law of large numbers. Taking disorder average of the input data corresponds to an appropriate feature selection, which is crucial in training our machine. Since the MLP is a totally nonlinear function, this is not the case for averaging the output.

As is shown in Fig. 3.5(a), classification of $P(\mathbf{r})$, i.e., the single-shot realization, results in a total meaninglessness, particularly in the strong disorder region.

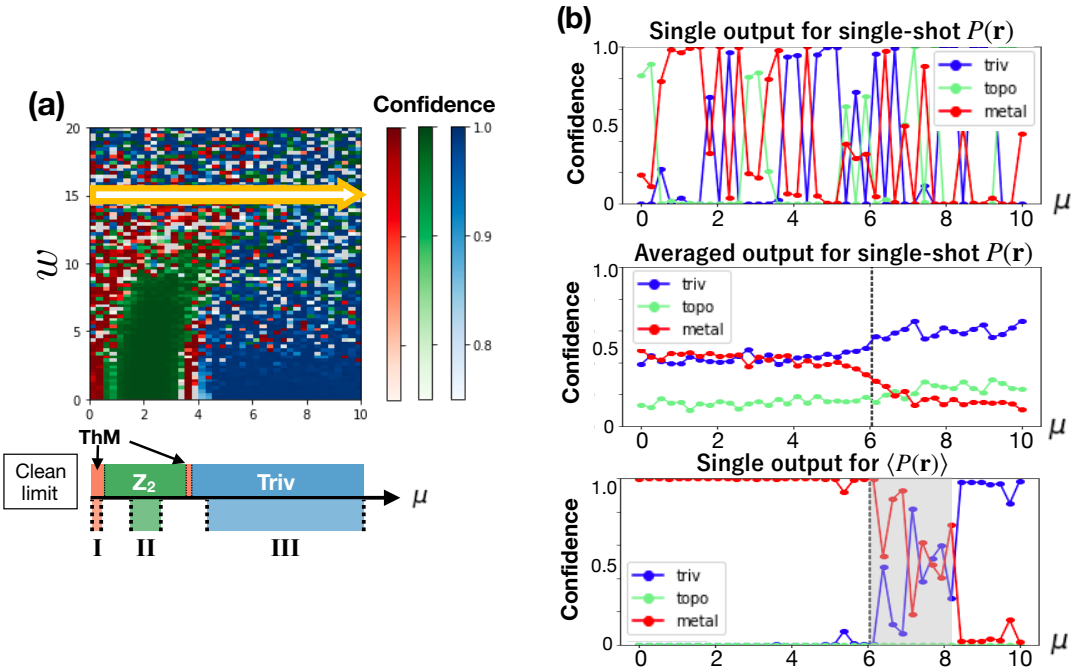

Figure 3.5: (a) The output of MLP for single-shot $P(\mathbf{r})$ for $\Delta = 3, \Delta_2 = 2$. Boundary between phases are hardly recognizable. (b) The single output for $P(\mathbf{r})$, the average of 200 outputs for independently generated $P(\mathbf{r})$, and the single output for $\langle P(\mathbf{r})\rangle$ with $N_r = 500$ from the top. The amplitude of the random potential is fixed as $w = 15$.

For the sake of simplicity, let us restrict the amplitude as $w = 15$ in the following. Shown at the top of Fig. 3.5(b) is the output for single-shot. The random values reflect the fact that the MLP is confused by the translational-symmetry-broken behavior of the quasiparticle. We see in the middle that averaging such outputs in a brute-force manner does not improve the situation at all. Although the faint slope around the boundary seems to capture the phase transition, the output converges far below the unity. It is questionable whether we can determine the phase in general. Shown at the bottom is the appropriate classification for $\langle P(\mathbf{r})\rangle$ with $N_r = 500$, in which the feature of the quasi-translational states are detected appropriately.

3.5 Summary of this Chapter

In this Chapter, the use of the MLP to classify phases of 2d noncentrosymmetric superconductor in class DIII with disorder is shown to be valid in the following two cases. One is the extension of the phase diagram of $w = 0$ to $w > 0$ when all possible phases are present in the clean limit. We have confirmed that the machine successfully learns the property of each phase from the *quasi*-translational symmetric $\langle P(\mathbf{r})\rangle$. The confidence of the machine is high within the phases, which reflects the successful feature extraction. Another is the detection of the unlearned phase. A correctly optimized MLP judges a state with high confidence when the learned feature is present in the data, and vice versa. The new phase does not exhibit localization in either bulk or the edge, and thus the machine is confused. We confirmed that in both cases the consistency with other independent methods (the transfer matrix method and noncommutative geometry approach) holds. Furthermore, the proposed method is numerically advantageous compared to the other two from the perspective of the variety of applicable models; the transfer matrix method becomes inefficient when multiple phase boundaries approach each other and the noncommutative geometry approach is ill-defined when both the bulk and mobility gap is closed. We see that neural-network-based method is capable of such difficulties.

Importantly, the current method relies on the appearance of edge states assured by the bulk-edge correspondence and the statistical recovery of the translational symmetry that is broken in individual data. Therefore, it is applicable to models with arbitrary lattice geometry, dimension, and symmetry class. In fact, it has been shown that higher-order topological phases in 2d systems has been detected [138] via the current scheme. Application to even wider class of models including topological crystalline insulators/superconductors is worth investigating. Also, we naturally expect from the ubiquitous appearance of the bulk-edge correspondence that the proposed scheme is applicable even under the presence of interaction or in bosonic systems.

Let us note that although the analysis here is based on the first moment of the quasiparticle distribution, in general, higher moments may also play a crucial role. In such a case, we expect that by adding the appropriate higher moments the classification can be done in other random system as well. Furthermore, we may consider alternative input to quasiparticle distribution for interacting systems with disorder; as long as the quantity contains information on the system

and recovers the symmetry statistically, the validity of the proposed method is expected. For instance, learning the entanglement spectra with the MLP has been shown to be a valid idea [17, 18, 20, 30]. We expect that such quantities are capable of capturing the property even when the disorder is present.

4
Representation of Classical Systems in Thermal Equilibrium

In this chapter, we find an exact mapping from the generalized Ising models with many-spin interactions to equivalent Boltzmann machines, i.e., the models introduced in Chapter 2 that consist of only two-spin interactions between physical and auxiliary binary variables accompanied by local external fields. More precisely, the appropriate combination of the algebraic transformations, namely the star-triangle and decoration-iteration transformations, allows one to express the model in terms of fewer-spin interactions at the expense of the degrees of freedom. Furthermore, the benefit of the mapping in Monte Carlo simulations is discussed. In particular, we demonstrate that the application of the method in conjunction with the Swendsen-Wang algorithm drastically reduces the critical slowing down in a model with two- and three-spin interactions on the Kagomé lattice.

4.1 Background

Since the invention of the Monte Carlo (MC) method, physicists have long made efforts to develop versatile and efficient simulation methods to investigate statistical models. In classical lattice systems, the single-spin flip (SSF) algorithm is undoubtedly one of the most widely-used techniques due to its independence. The locality of the variables involved in a single update procedure, however, inevitably leads to a severe slowing down near critical points or at low temperature for non-ordering systems. One of the solutions is to apply the global updates such as the cluster algorithms [139, 140], worm algorithm [141], and loop algorithm [142], but they are mostly restricted to two-spin interacting systems. Developing a generic technique applicable to a wide variety of systems involving many-spin interactions is highly challenging.

In this work, we establish a mapping from the generalized Ising model to the BM. The former, which includes many-spin interactions, is used to describe

a wide variety of natural phenomena including magnetic and thermodynamic properties of solids, the effective model of alloys, spin glass models, and so on [143–145]. As we have introduced in Chapter 2, the BM, on the other hand, is an expression of probability distribution by two-spin interactions between physical (visible) and auxiliary (hidden) degrees of freedom. The mapping procedure goes as follows: one first decomposes a p-spin Ising interaction into a sum of three- and $(p-1)$-spin interactions by adding an auxiliary spin. This is repeated until the total interaction is expressed in terms of two- and three-spin interactions. Finally, each three-spin interaction is transformed into two-spin interactions and single-spin terms. The idea of such consecutive decomposition can also be seen in the context of quantum annealing, in which embedding of hidden spins are considered to keep the ground state (and limited number of excited states) invariant [146–149].

After constructing the rigorous mapping between these representations, we take advantage of it by presenting a novel global update scheme; the application of the Swendsen-Wang algorithm to the exactly surrogate BM. By comparing the autocorrelation times of the visible spin configurations, we demonstrate in a model with two- and three-spin interactions on the Kagomé lattice that the sampling efficiency of the cluster algorithm on the BM at the critical temperature is drastically improved compared to that of the SSF algorithm performed on the original Hamiltonian. While it is possible to introduce cluster-update algorithm with fewer auxiliary degrees of freedom in some specific many-spin interacting models by modifying the Fortuin-Kasteleyn transformation, as was done for the four-spin interacting model on the square lattice [15], the mapping introduced in this thesis aims to provide a rather general framework. Namely, models with arbitrary order of interaction in any number of dimensions can be handled systematically.

The remainder of this chapter is organized as follows. In Sec. 4.2 we first introduce the most primary transformation techniques, namely the decoration-iteration and star-triangle transformations. Embedding the hidden spins by combining the two, an arbitrary many-spin interaction is shown to be mappable to the BM. Furthermore, multiple interaction terms can be taken into account by simply considering the embedding procedures independently. In Sec. 4.3, we see that the transformation is numerically beneficial since the existing cluster update can be applied to the BM. Finally, the summary for the current work and discussion concerning the future direction are given in Sec. 4.4. For the completeness of the

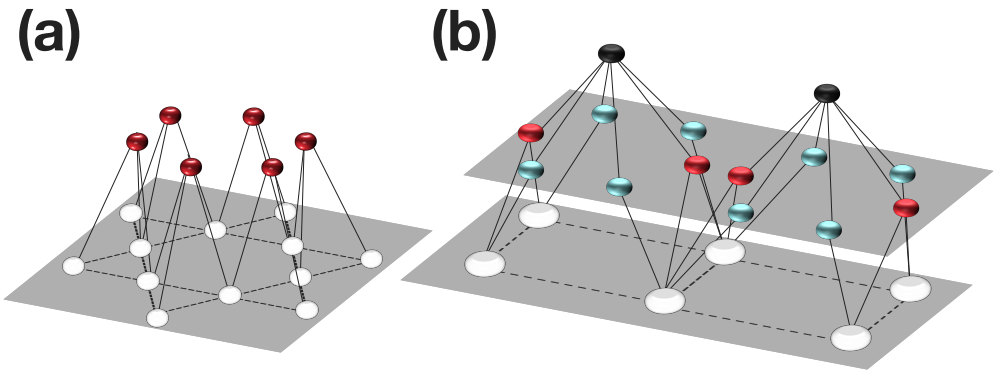

Figure 4.1: Schematic picture of (a) restricted Boltzmann machine (RBM) that is equivalent to a model with three-spin interaction, (b) deep Boltzmann machine (DBM) that is equivalent to a model with four-spin interaction. The white and black objects denote visible and deep spins, respectively. Also, the blue and red objects are the hidden spins introduced by the decoration-iteration transformation (DIT) and star-triangle transformation (STT), which are given by Eq. (4.5) and Eq. (4.7). The presence of the layers is denoted by the gray planes. Note that the mapping to the RBM or DBM is applicable irrespective of the spatial dimension.

chapter, in Appendix D, we describe the MC sampling algorithms. The partition function of the pure three-spin interacting model on the Kagomé lattice, from which the absence of the phase transition follows, is calculated in Appendix E.

4.2 Algebraic Transformation of Boltzmann Factors

In this section, we find the equivalence of the generalized Ising models and the BMs with specific architectures, i.e., the restricted Boltzmann machine (RBM) and the deep Boltzmann machine (DBM). [See Fig. 4.1 for the graphic representation.] As was introduced in Chapter 2, the Boltzmann factor given by the RBM is follows,

$$\pi(\boldsymbol{\sigma}) = \sum_{\boldsymbol{h}} \widetilde{\pi}(\boldsymbol{\sigma}, \boldsymbol{h}) = \sum_{\boldsymbol{h}} e^{-E(\boldsymbol{\sigma}, \boldsymbol{h})} \tag{4.1}$$

$$-E(\boldsymbol{\sigma}, \boldsymbol{h}) = \exp\left\{ \sum_{i,j} W_{ij}\sigma_i h_j + \sum_i a_i \sigma_i + \sum_j b_j h_j \right\}, \tag{4.2}$$

where the parameter W_{ij} is the interaction between the i-th visible and j-th hidden spins, to which the magnetic fields are imposed as a_i and b_j. We denote the visible and hidden spin configurations by $\boldsymbol{\sigma} := (\sigma_1, \sigma_2, ..., \sigma_{N_v}) \in \mathcal{S}$ and $\boldsymbol{h} := (h_1, h_2, ..., h_{N_h}) \in \mathcal{H}$, where $\mathcal{S} = \{-1, 1\}^{N_v}$ and $\mathcal{H} = \{-1, 1\}^{N_h}$ are the sets of all possible binary spin configurations for N_v visible and N_h hidden spins, respectively. Also, to discriminate between the spaces with and without the hidden spins, we call $\mathcal{S}$ as the "original space" and $\mathcal{S} \cup \mathcal{H}$ as the "extended space."

As for the DBM, we find that the maximum number of layers obtained by mapping from the generalized Ising model is two. We therefore discriminate the first and second hidden layers as the "hidden layer" and "deep layer" in the current chapter for simplicity, and the spins included in these layers are correspondingly referred to as the "hidden spins" and "deep spins." To be concrete, the Boltzmann factor of a two-hidden-layer DBM is given as

$$\pi(\boldsymbol{\sigma}) = \sum_{\boldsymbol{h},\boldsymbol{d}} \widetilde{\pi}(\boldsymbol{\sigma}, \boldsymbol{h}, \boldsymbol{d}), \tag{4.3}$$

$$\widetilde{\pi}(\boldsymbol{\sigma}, \boldsymbol{h}, \boldsymbol{d}) = \exp\left\{ \sum_{i,j} W_{ij}\sigma_i h_j + \sum_{j,k} W'_{jk} h_j d_k + \right. \\ \left. + \sum_i a_i \sigma_i + \sum_j b_j h_j + \sum_k b'_k d_k \right\}, \tag{4.4}$$

where $\widetilde{\pi}(\boldsymbol{\sigma}, \boldsymbol{h}, \boldsymbol{d})$ is the Boltzmann factor for each spin configuration, d_k is the k-th deep spin with the local field b'_k, and W'_{jk} is the interaction between the j-th hidden spin and the k-th deep spin. As is the case for the visible and hidden spins, a configuration of the deep spins is denoted by $\boldsymbol{d} := (d_1, d_2, ..., d_{N_d}) \in \mathcal{D}$, where $\mathcal{D} = \{-1, 1\}^{N_d}$ is the set of all possible configurations of N_d deep spins. The union $\mathcal{S} \cup \mathcal{H} \cup \mathcal{D}$ is also referred to as the extended space in the following.

In the remainder of this section, we find the exact mapping from the generalized Ising model to the RBM or DBM.

4.2.1 Transformation techniques

We introduce two mapping techniques to embed hidden spins as is graphically described in Fig. 4.2: the decoration-iteration transformation (DIT) and star-triangle transformation (STT). Note that the newly embedded spins are auxiliary, and the original interactions are realized by tracing out such degrees of freedom.

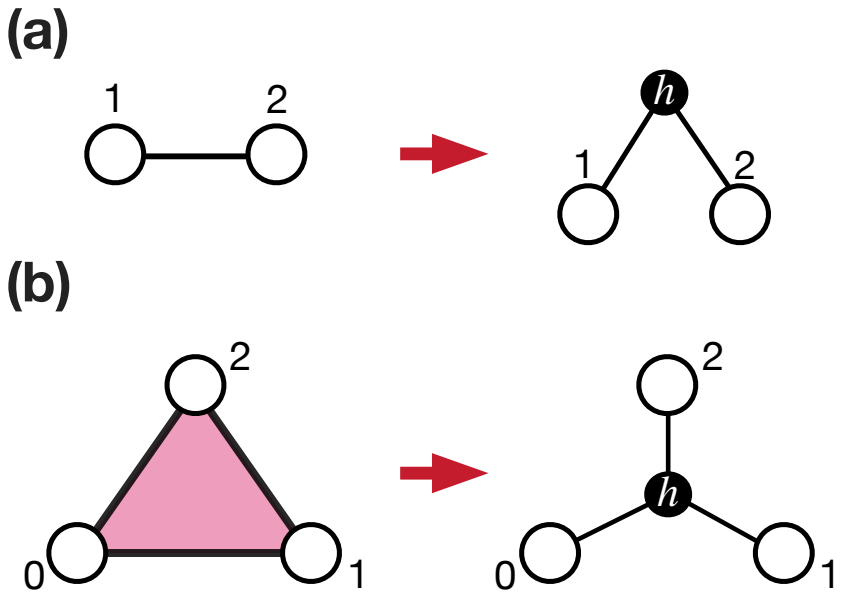

Figure 4.2: Schematic description of the mapping techniques: (a) Decoration-iteration transformation and (b) star-triangle transformation. The white and black circles correspond the visible and hidden spins, respectively, and the numbers denote the labels of the visible spins. The solid lines and the filled region denote the two- and three-spin interactions, respectively.

The DIT, depicted in Fig. 4.2(a), is a very simple transformation which embeds a hidden spin h between two interacting visible spins as follows [150, 151],

$$e^{J\sigma_1\sigma_2} = \Delta \sum_{h=\pm 1} \exp\left[W(\sigma_1 + \mathrm{sgn}(J)\sigma_2)h\right], \tag{4.5}$$

where Δ is the normalization factor and the new interaction W is given as

$$W = \mathrm{arc\,cosh}\left(e^{2|J|}\right)/2. \tag{4.6}$$

Since the DIT can be carried out for any J, an arbitrary Ising model with two-spin interactions including random spin-glass, frustrated system, and fully-connected models can be mapped into an equivalent RBM. Application of such transformation technique allows one to obtain the exact solution for a model on, for instance, two-spin interacting Ising model on a bond-decorated lattice that can be transformed into the soluble model on an undecorated lattice [150, 152–156].

The other technique, known as the STT, embeds a hidden spin h into three visible spins with both two- and three-spin interactions as is illustrated in Fig. 4.2(b) [151,

157–160]. Expressed in the form of the Boltzmann weight, this can be written as [161]

$$\begin{aligned}&\exp\left[M\sigma_1\sigma_2\sigma_3 + J_1\sigma_2\sigma_3 + J_2\sigma_3\sigma_1 + J_3\sigma_1\sigma_2\right]\\ &\quad = \Delta \sum_{h=\pm 1} \exp\left[\sum_{i=1}^{3}(W_i h + a_i)\sigma_i + bh\right],\end{aligned} \tag{4.7}$$

where M and J_i are the amplitudes of three- and two-spin interactions, respectively. The interaction between the visible and the hidden spins in the extended space is denoted by W_i, and the local fields are denoted by a_i and b, respectively. It can be shown that Eq. (4.7) amounts to eight nonequivalent conditions which yields the solutions as

$$\exp(4\chi_i a_i) = \frac{\sinh(2(|J_i| + M))}{\sinh(2(|J_i| - M))}, \tag{4.8}$$

$$\cosh(2W_i) = \frac{e^{2|J_i|}\cosh\left(2(|J_j|+|J_k|)\right) - e^{-2|J_i|}\cosh\left(2(|J_j|-|J_k|)\right)}{[2\cosh(4|J_i|) - 2\cosh(4M)]^{1/2}}, \tag{4.9}$$

$$\sinh(2b) = \frac{-\sinh(2\chi_i W_i)\sinh(4M)}{[(\cosh(4J_j) - \cosh(4M))(\cosh(4J_k) - \cosh(4M))]^{1/2}}, \tag{4.10}$$

where $\chi_i = \mathrm{sgn}(J_i)$ is the sign of the two-spin interaction. The subscripts in Eqs. (4.9) and (4.11), i.e., i, j, and k, must be chosen such that none of them are identical to each other. Importantly, the STT is valid under the following conditions [*1]

$$|M| < |J_i| \qquad (i = 1, 2, 3), \tag{4.11}$$

$$\mathrm{sgn}(J_1 J_2 J_3) = 1. \tag{4.12}$$

The notion of the DIT and STT can be generalized to include many-spin interactions. A system in the original space with both four- and two-spin interactions, for instance, can be mapped to a model with three-spin interactions that involves a single hidden spin. This mapping, used to obtain the solution of the zero-field eight-vertex model, is referred to as the star-square transformation [151, 162–164]. While the transformation from the extended space into the original space, known as "the star-polygon transformation," is achieved by tracing out the hidden spins and is in general tractable [155, 165], its inverse mapping exists in very limited

[*1] Naively, it might seem that the mapping is inapplicable to frustrated systems due to the condition given in Eq. (4.12). However, we emphasize that any frustrated system can be mapped to RBM/DBM, for instance, by introducing virtual two-spin interactions as in Eq. (4.16)

cases. We note in passing that the DIT and STT have been extended to models with local quantum degrees of freedom such as Heisenberg spins and itinerant electrons [166–168].

4.2.2 Generalized Ising model as Boltzmann Machine

Here, we show that the generalized Ising model, which consists of many-spin interactions, can be mapped to an equivalent BM. Since the Boltzmann factor can be written as products over those of many-spin interactions, we may simply focus on the decomposition of a bare p-spin interaction. More concretely, let us consider a Hamiltonian as follows,

$$-\beta H = \sum_{\mathcal{C}} M_{\mathcal{C}} \left(\prod_{\sigma \in \mathcal{C}} \sigma \right), \tag{4.13}$$

where $M_{\mathcal{C}}$ is the amplitude of the interaction with the inverse temperature β multiplied and $\mathcal{C}$ is a support of an interaction. We dub the support of a given interaction as the "cell" in the following, and denote the number of visible spins included as $|\mathcal{C}|$. The Boltzmann weight of this Hamiltonian under the inverse temperature β is given as

$$\begin{aligned} \pi(\boldsymbol{\sigma}) &= \prod_{\mathcal{C}} \pi_{|\mathcal{C}|}(\boldsymbol{\sigma}_{\mathcal{C}}; M_{\mathcal{C}}) = \prod_{\mathcal{C}} \left(\sum_{\boldsymbol{h}_{\mathcal{C}}, \boldsymbol{d}_{\mathcal{C}}} \widetilde{\pi}(\boldsymbol{\sigma}_{\mathcal{C}}, \boldsymbol{h}_{\mathcal{C}}, \boldsymbol{d}_{\mathcal{C}}) \right), \\ \pi_{|\mathcal{C}|}(\boldsymbol{\sigma}_{\mathcal{C}}; M) &:= \exp\left(M \prod_{\sigma \in \mathcal{C}} \sigma \right), \end{aligned} \tag{4.14}$$

where $\pi_{|\mathcal{C}|}$ is the Boltzmann factor for $|\mathcal{C}|$-spin interaction. The visible spin configuration of the cell $\mathcal{C}$ is denoted by $\boldsymbol{\sigma}_{\mathcal{C}} \in \mathcal{S}_{\mathcal{C}}$, where $\mathcal{S}_{\mathcal{C}}$ is the set of all possible configurations of the visible spins included in $\mathcal{C}$.

As is evident from Eq. (4.14), the Boltzmann factor for Hamiltonian given as Eq. (4.13) can be decomposed into products over cells. We therefore focus on bare p-spin interaction and verify the following decomposition,

$$\pi_{|\mathcal{C}|}(\boldsymbol{\sigma}_{\mathcal{C}}; M_{\mathcal{C}}) = \sum_{\boldsymbol{h}_{\mathcal{C}}, \boldsymbol{d}_{\mathcal{C}}} \widetilde{\pi}(\boldsymbol{\sigma}_{\mathcal{C}}, \boldsymbol{h}_{\mathcal{C}}, \boldsymbol{d}_{\mathcal{C}}), \tag{4.15}$$

where $\widetilde{\pi}(\boldsymbol{\sigma}_{\mathcal{C}}, \boldsymbol{h}_{\mathcal{C}}, \boldsymbol{d}_{\mathcal{C}})$ is the weight of the BM obtained by transformation. Also, a single realization of hidden and deep spins labeled by $\mathcal{C}$ is denoted as $\boldsymbol{h}_{\mathcal{C}} \in \mathcal{H}_{\mathcal{C}}$ and $\boldsymbol{d}_{\mathcal{C}} \in \mathcal{D}_{\mathcal{C}}$, where $\mathcal{H}_{\mathcal{C}}$ and $\mathcal{D}_{\mathcal{C}}$ are the sets of all possible configurations of the hidden and deep spins included in $\mathcal{C}$, respectively. Note that although a visible

spin may be included in multiple cells, the auxiliary spins are uniquely allocated to their corresponding cells by construction.

Three-spin interaction as RBM

First, we discuss the three-spin interaction as the simplest possible case. Due to the conditions given in Eqs. (4.11) and (4.12), the STT cannot be applied straightforwardly to a bare three-spin interaction. To avoid this problem, we introduce the "virtual two-spin interactions" that cancel each other out as follows,

$$\begin{aligned}\pi_3(\boldsymbol{\sigma}; M) &= \exp(M\sigma_1\sigma_2\sigma_3) \\ &= \exp\left[M\sigma_1\sigma_2\sigma_3 + J_1\sigma_2\sigma_3 + J_2\sigma_3\sigma_1 + J_3\sigma_1\sigma_2\right] \\ &\quad \times \exp\left[-(J_1\sigma_2\sigma_3 + J_2\sigma_3\sigma_1 + J_3\sigma_1\sigma_2)\right]. \end{aligned} \tag{4.16}$$

As is depicted in Fig. 4.3(a), this can be mapped into the RBM by applying Eq. (4.7) to the first and subsequently Eq. (4.5) to the second factors. Note that the amplitudes of the virtual two-spin interaction, J_i, can be taken arbitrarily as long as Eqs. (4.11) and (4.12) are satisfied.

Next, let us consider two sets of interacting spins as denoted in Fig. 4.3(b). Although the naive application of Eq. (4.16)) yields eight hidden spins, two of them on the shared edges can be eliminated by modifying the signs of virtual two-spin interactions. For instance, by considering the virtual two-spin interactions with a homogeneous amplitude, we obtain

$$\begin{aligned}&\pi_3(\boldsymbol{\sigma}_{\mathcal{C}_1}; M)\pi_3(\boldsymbol{\sigma}_{\mathcal{C}_2}; M) \\ =\ &\exp(M\sigma_1\sigma_2\sigma_3)\exp(M\sigma_2\sigma_3\sigma_4) \\ =\ &\exp\left[M\sigma_1\sigma_2\sigma_3 + J\sigma_2\sigma_3 + J\sigma_3\sigma_1 + J\sigma_1\sigma_2\right]\exp\left[M\sigma_2\sigma_3\sigma_4 + J\sigma_3\sigma_4 - J\sigma_4\sigma_2 - J\sigma_2\sigma_3\right] \\ &\times \exp\left[-(J\sigma_3\sigma_1 + J\sigma_1\sigma_2 + J\sigma_3\sigma_4 - J\sigma_4\sigma_2)\right], \end{aligned} \tag{4.17}$$

from which six hidden spins emerge.

Furthermore, a system with pure three-spin interaction on the triangular lattice, known to be exactly soluble and dubbed as the Baxter-Wu model [169], can also be mapped into the RBM merely without hidden spins generated by the DIT. In other words, we may choose the signs of the virtual two-spin interactions on the triangles carefully so that the sum at each edge would cancel out, resulting in a reduced number of the hidden spins. Still, there are exponential number of ways to represent this model by tuning the amplitudes and the signs of the virtual two-spin interactions. Shown in Fig. 4.3(c) is the mapping with 4-fold periodicity along the x-axis.

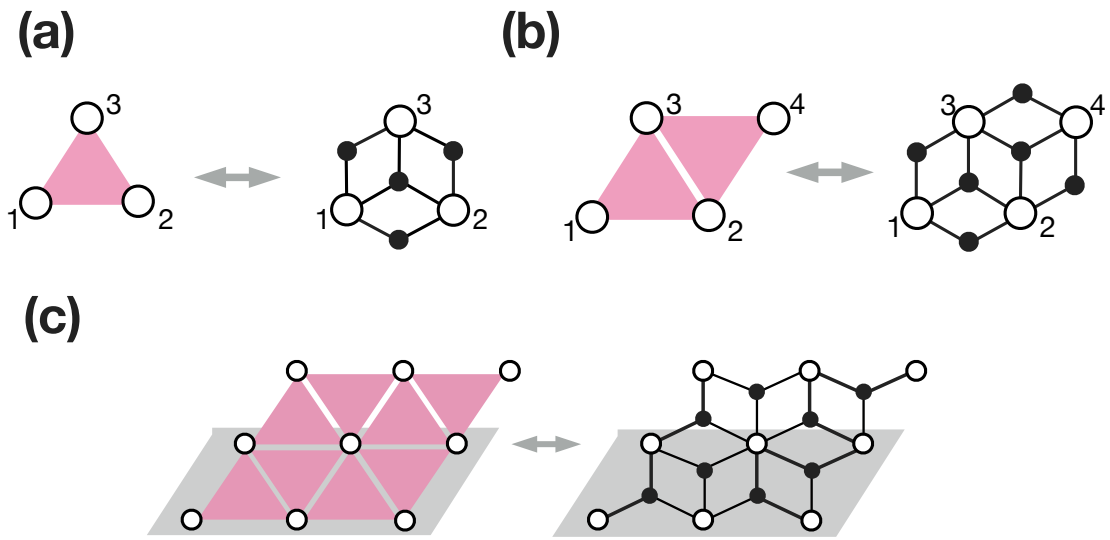

Figure 4.3: (a) Transforming a pure three-spin interaction into an RBM. The red filled circles in the right-hand side are generated by the STT and the blue ones by the DIT. The black solid and dotted lines denote the positive and negative two-spin interactions, respectively. The amplitudes of the virtual two-spin interactions are taken as $J_i > 0$ in the figure. (b) Transforming a couple of three-spin interactions. The signs of the virtual two-spin interactions are modified so that the number of the hidden spins is reduced. (c) Transforming the Baxter-Wu model into an RBM.

Four-spin interaction as DBM

Next, we show that four-spin interaction can be expressed by introducing the second hidden layer, or the "deep" layer. The illustration of the two-step transformation is shown in Fig. 4.4. In the first step, we interpret the product of Ising variable as a single new binary variable and apply the DIT as

$$\begin{aligned} \pi_4(\boldsymbol{\sigma}; M^{(0)}) &= \exp\left[M^{(0)}\sigma_1\sigma_2\sigma_3\sigma_4\right] \\ &= \Delta \sum_{d=\pm 1} \exp\left[M^{(1)}(\sigma_1\sigma_2 + \sigma_3\sigma_4)d\right] \\ &= \Delta \sum_{d=\pm 1} \pi_3\left(\sigma_1, \sigma_2, d; M^{(1)}\right) \pi_3\left(\sigma_3, \sigma_4, d; M^{(1)}\right), \end{aligned} \tag{4.18}$$

where $\pi_4(\boldsymbol{\sigma}; M^{(0)})$ is the Boltzmann factor for four-spin interaction with the amplitude $M^{(0)}$. The interaction amplitudes $M^{(0)}$ and $M^{(1)}$ are related by Eq. (4.6)

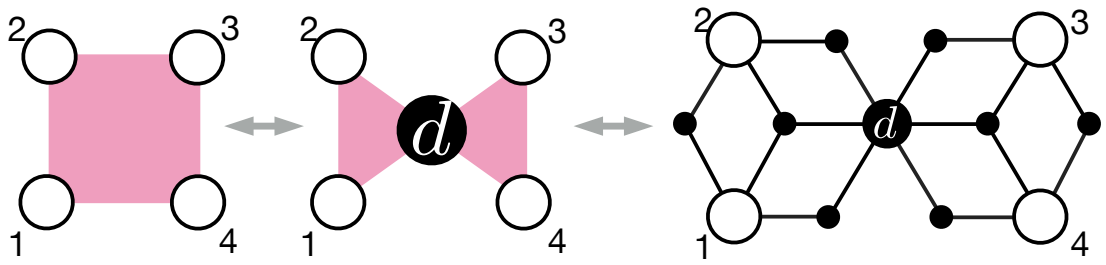

Figure 4.4: Transforming four-spin interaction into a DBM. The black filled circle is the spin in the deep layer, and the other notation follows that of Fig. 4.3.

as

$$M^{(1)} = \text{arc cosh}\left(e^{2|M^{(0)}|}\right)/2. \tag{4.19}$$

Next, we use Eq. (4.16), the result for the three-spin interaction, under homogeneous virtual two-spin interactions $J > |M^{(1)}|$ for simplicity. Here, we obtain the expression as

$$\pi_4(\boldsymbol{\sigma}; M^{(0)}) = \Delta \sum_d \sum_{h_a,h_b} \sum_{h_1,\ldots h_6} \widetilde{\pi}_2^{\text{STT}}(\boldsymbol{\sigma},\boldsymbol{h},d)\widetilde{\pi}_2^{\text{DIT}}(\boldsymbol{\sigma},\boldsymbol{h},d)\widetilde{\pi}_1(\boldsymbol{\sigma},\boldsymbol{h},d), \tag{4.20}$$

where

$$\begin{aligned}
\widetilde{\pi}_2^{\text{STT}}(\boldsymbol{\sigma},\boldsymbol{h},d) &= \exp[W(\sigma_1+\sigma_2+d)h_a + W(\sigma_3+\sigma_4+d)h_b], \\
\widetilde{\pi}_2^{\text{DIT}}(\boldsymbol{\sigma},\boldsymbol{h},d) &= \exp\left[\sum_{i=1}^{4} W'(\sigma_i - d)h_i + W'(\sigma_1-\sigma_2)h_5 + W'(\sigma_3-\sigma_4)h_6\right] \\
\widetilde{\pi}_1(\boldsymbol{\sigma},\boldsymbol{h},d) &= \exp\left[a\sum_i \sigma_i + a_d d + b(h_a+h_b)\right].
\end{aligned}$$

Here, $\widetilde{\pi}_2^{\text{STT(DIT)}}(\boldsymbol{\sigma},\boldsymbol{h},d)$ is the Boltzmann factor for the two-spin interaction in the extended space obtained by the STT (DIT), and $\widetilde{\pi}_1(\boldsymbol{\sigma},\boldsymbol{h},d)$ is that for the local external fields. The interaction W (W') is the interlayer coupling introduced by the STT (DIT). The magnetic field for the visible, deep, and hidden spins are denoted by a, a_d, and b, respectively. The equivalence of amplitudes of the three-spin interactions, $M^{(1)}$, leads to $a_d = 2a$. Also, the application of DIT to the virtual two-spin interaction yields $W' = \text{arc}\cosh(e^{2J})/2$. Note that the other parameters

are obtained by substituting $M = M^{(1)}$ and homogeneous $J_i = J$ into Eq. (4.7) as

$$\exp(4a) = \frac{\sinh(2(J + M^{(1)}))}{\sinh(2(J - M^{(1)}))}, \tag{4.21}$$

$$\cosh(2W) = \frac{e^{2J}\cosh(4J) - e^{-2J}}{[2\cosh(4J) - 2\cosh(4M^{(1)})]^{1/2}}, \tag{4.22}$$

$$\sinh(2b) = \frac{-\sinh(2W)\sinh(4M^{(1)})}{|\cosh(4J) - \cosh(4M^{(1)}))|}. \tag{4.23}$$

Another way to transform four-spin interaction is to apply the star-square transformation. Although it also requires a single deep spin, the architecture of the hidden spins would be symmetric and hence different from the aforementioned transformation. To keep the number of auxiliary spins minimum, we will not use the star-square transformation in the following.

Note that N_h/N_d, or the ratio of the number of the hidden spins to that of the visible spins, may be reduced in a larger system as well as in Sec. 4.2.2; we may cancel out the virtual two-spin interactions by modifying their signs.

p-spin interaction as DBM

The discussion for four-spin interaction can be extended to p-spin interaction. The procedure consists of two steps; embedding the deep spins, and then the hidden spins. The mapping procedure can be summarized as the following:

1. Decompose the p-spin Ising interaction into a sum of three- and $(p-1)$-spin interactions by adding an auxiliary spin.

2. Repeat 1. until the p-spin interaction is expressed in terms of two- and three-spin interactions.

3. Apply the STT for every three-spin interaction.

A system with a bare p-spin interaction is mapped into an equivalent system with three-spin interactions in the former step and subsequently broken into systems with two-spin interactions and local fields in the latter step. Since the DIT is applied repeatedly, we define

$$M^{(k+1)} = \operatorname{arc\,cosh}\left(e^{2|M^{(k)}|}\right)/2, \tag{4.24}$$

$$M^{(0)} = M, \tag{4.25}$$

where M determines the amplitude of the interaction as $\pi_p(\boldsymbol{\sigma}; M)$. The number of DITs applied, or k, is referred to the DIT transformation order.

Let us take four-spin interaction as the starting point. By replacing one of the Ising variables in Eq. (4.20) with a product of two, we obtain the expression for five-spin interaction as

$$\begin{aligned}\pi_5(\boldsymbol{\sigma}; M^{(0)}) &= \exp\left[M^{(0)}\sigma_1\sigma_2\sigma_3\sigma_4\sigma_5\right] \\ &= \Delta \sum_{d_1=\pm 1} \pi_3\left(\sigma_1, \sigma_2, d_1; M^{(1)}\right) \pi_4\left(\sigma_3, \sigma_4, \sigma_5, d_1; M^{(1)}\right) \\ &= \Delta \sum_{d_1, d_2=\pm 1} \pi_3\left(\sigma_1, \sigma_2, d_1; M^{(1)}\right) \pi_3\left(\sigma_3, d_1, d_2; M^{(2)}\right) \pi_3\left(\sigma_4, \sigma_5, d_2; M^{(2)}\right),\end{aligned} \tag{4.26}$$

which is visually described in Fig. 4.5(a). Repeating the DIT such that the DIT transformation order is as homogeneous as possible, we can show *a posteriori* that the general expression is given as

$$\begin{aligned}\pi_p(\boldsymbol{\sigma}; M) = \Delta \sum_{\mathbf{d}} & \overbrace{\pi_3(\sigma_1, \sigma_2, d_1; M^{(n)})\pi_3(\sigma_3, d_1, d_2; M^{(n)}) \cdots}^{2^{n+1}-(p-2)} \\ & \times \underbrace{\pi_3(\sigma_{p-1}, \sigma_p, d_{p-3}; M^{(n+1)})\pi_3(\sigma_{p-2}, d_{p-3}, d_{p-4}; M^{(n+1)}) \cdots}_{2(p-2-2^n)},\end{aligned} \tag{4.27}$$

where n is an integer satisfying $2^n \leq p-2 < 2^{n+1}$. Note that there are two factors consisting of two visible spins, whereas the others contain only one. The number of factors with $M^{(n+1)}$ is zero if $p-2 = 2^n$.

To consider the hidden spins, we substitute $M^{(n)}$ in the transformation introduced in Sec. 4.2.2 as, for instance,

$$\begin{aligned}\pi_3(\sigma_1, \sigma_2, d_1; M^{(n)}) = \Delta \sum_{\boldsymbol{h}} & \exp[(Wh + a)(\sigma_1 + \sigma_2 + d_1) + bh] \\ & \times \exp[W'[(\sigma_1 - \sigma_2)h_1 + (d_1 - \sigma_1)h_2 + (\sigma_2 - d_1)h_3]],\end{aligned} \tag{4.28}$$

which is described in the right-most panels of Fig. 4.5.

The number of the hidden and deep spins can be computed as well. We denote the numbers of hidden spins in the first layer generated by the STT, DIT, and that of the deep spins in the second hidden layer as $n_h^{\mathrm{STT}}, n_h^{\mathrm{DIT}}$, and n_d. It is straightforward to show that the following relations are satisfied,

$$n_h^{\mathrm{STT}} = 3(p-2), \quad n_h^{\mathrm{DIT}} = p-2, \quad n_d = p-3. \tag{4.29}$$

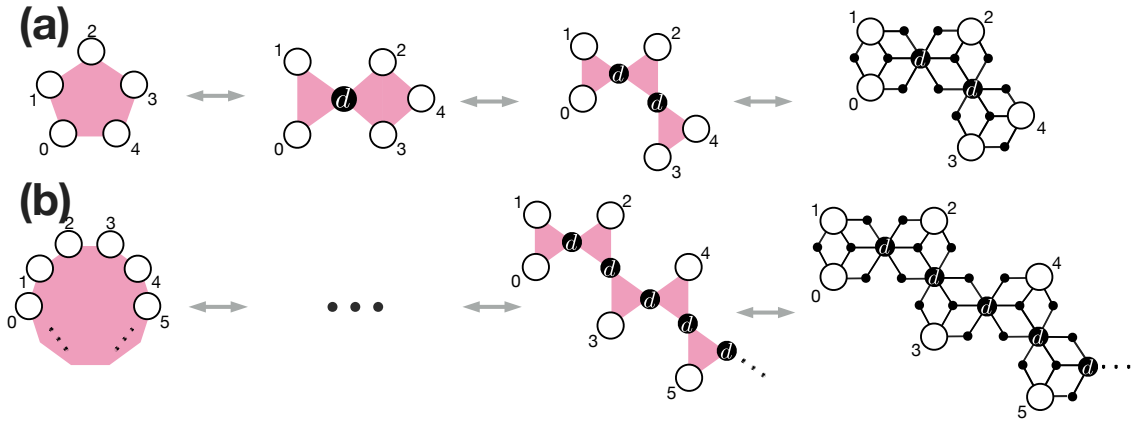

Figure 4.5: The transformation of (a) five-spin interaction and (b) p-spin interaction. First mapped into a system with only three-spin interactions by applying DIT, the transformation technique for the three-spin interaction is used to break up into two-spin interactions with local external fields.

It is noteworthy from the perspective of the numerical cost that the number of hidden and deep spins increases only linearly with respect to p. The computational cost remains to be the same for any update scheme.

4.3 Monte Carlo sampling on Boltzmann machine

In the following, we utilize the BM obtained by the transformation to classical MC sampling. The block Gibbs sampling, which is frequently used for the RBM or DBM in the machine learning community, turns out to lack efficiency in terms of autocorrelation although the numerical cost per a single MC step is low [7, 48]. We alternatively apply the cluster-update algorithm by Swendsen and Wang to the extended space and demonstrate the speed up compared to the SSF algorithm on the original space. First, we take the square-lattice Ising model for a simplified description of our scheme, and then proceed to show the results in the model with ferromagnetic two-spin interactions and alternating three-spin interactions on the Kagomé lattice, which is one of the the most comprehensible models that includes the many-spin interaction and also suffers from the slowing down at the critical temperature.

4.3.1 Ising model on square lattice

We consider a Hamiltonian with two-spin interactions on a square lattice,

$$H = -\sum_{\langle i,j \rangle} \sigma_i \sigma_j, \tag{4.30}$$

which shows the ferro-paramagnetic transition at $T_c = 2/\ln(\sqrt{2}+1)$ as is widely known in statistical physics [170]. The study by the SSF algorithm, i.e., the Glauber dynamics in a broader sense, suffers from severe critical slowing down [171, 172]. [The algorithm is given in Appendix D.1.] The application of global updates, e.g., cluster updates [139, 140], is one of the solutions under some circumstances. For instance, the well-known cluster update algorithm by Swendsen and Wang, which is discussed in detail in Appendix D.2, dramatically improves the situation by speeding up the pre-thermalization and reducing the autocorrelation time.

Given the bipartite structure of the square lattice, one might consider the block Gibbs sampling as is done for usual RBMs with dense connection. Unfortunately, this is not the case. Let A and B be the sublattices of the square lattice. The spin configuration on a sublattice is denoted as $\sigma_{A(B)} = \left\{ \{\sigma_i\} | i \in V_{A(B)} \right\}$ where $V_{A(B)}$ is the set of $A(B)$-sublattice sites. The posterior distribution for spin configuration on the A sublattice is written as

$$p(\sigma_A|\sigma_B) := \pi(\sigma_A, \sigma_B) / \sum_{\sigma_A} \pi(\sigma_A, \sigma_B), \tag{4.31}$$

$$\pi(\sigma_A, \sigma_B) = \exp\left(\beta \sum_{\langle i,j \rangle} \sigma_i \sigma_j \right), \tag{4.32}$$

where $\pi(\sigma_A, \sigma_B)$ denotes the Boltzmann factor for the total system and $\langle i, j \rangle$ denotes the edge connecting the sites i and j. Since spins in the A sublattice do not couple to each other, Eq. (4.31) can be factorized as

$$p(\sigma_A|\sigma_B) = \prod_{i \in V_A} p(\sigma_i|\sigma_B), \tag{4.33}$$

$$p(\sigma_i|\sigma_B) = \frac{\exp\left[\beta \sigma_i \sum_{j \in \partial i} \sigma_j\right]}{2\cosh\left[\beta \sum_{j \in \partial i} \sigma_j\right]}, \tag{4.34}$$

where ∂i denotes the set of sites adjacent to i. The update method based on the simultaneous and independent sampling of spins on either of sublattices without rejection is called the block Gibbs sampling.

However, such an algorithm is not beneficial for the following reason. Consider a domain consisting of upward spins. In the bulk region of the domain, it is highly probable according to the Eq. (4.33) that the newly sampled spins remain upwards as well. In other words, the limited range of the connection results in the mutual locking structure in the bulk region, allowing only the peripheral region to flip. Such a problematic situation is exacerbated as the domain size grows, and turns out that the slowing down is much worse than the SSF algorithm.

4.3.2 Generalized Ising model on Kagomé lattice

In the following, we find that the cluster algorithm is beneficial not only for simulation in two-spin interacting models but also the ones with many-spin interactions. By transforming the generalized Ising model into Boltzmann machines, we may employ the cluster update algorithm. As was shown in the previous section, the number of the hidden and deep spins increases linearly with the system size, and therefore the computational order of a single MC step remains to be $O(N)$ in a model with short-range interactions, which is also the case in the current work.

As a demonstration, we consider a model with ferromagnetic two-spin interactions and also three-spin interactions on a Kagomé lattice. Let E be the set of edges and $\triangle(\triangledown)$ be an upward (downward) triangle on the lattice. The Hamiltonian is defined as

$$-\beta H = \beta \sum_{\langle i,i' \rangle \in E} \sigma_i \sigma_{i'} + \sum_{\triangle} M_{\triangle} \tau_{\triangle} + \sum_{\triangledown} M_{\triangledown} \tau_{\triangledown}, \tag{4.35}$$

where $\tau_{\triangle} = \prod_{i \in \triangle} \sigma_i$ and $\tau_{\triangledown} = \prod_{i \in \triangledown} \sigma_i$ is the product of the spin variables, $M_{\triangle}/\beta$ ($M_{\triangledown}/\beta$) denotes the amplitude of the three-spin interactions for upward (downward) triangles, and $\langle i, i' \rangle$ is the edge connecting sites i and i'. The symmetry that combines the spin inversion and the mirror inversion is present when $M_{\triangle} + M_{\triangledown} = 0$, and the model exhibit second-order transition at finite temperature for finite $M_{\triangle}$ [See AppendixE for discussion when only three-spin interactions are present.]. This can be understood from the correspondence between the present model and the antiferromagnetic Ising model with a uniform external field on the honeycomb lattice [173].

In the following, we assume $M_{\triangle} = -M_{\triangledown} = M > 0$. The Boltzmann weight

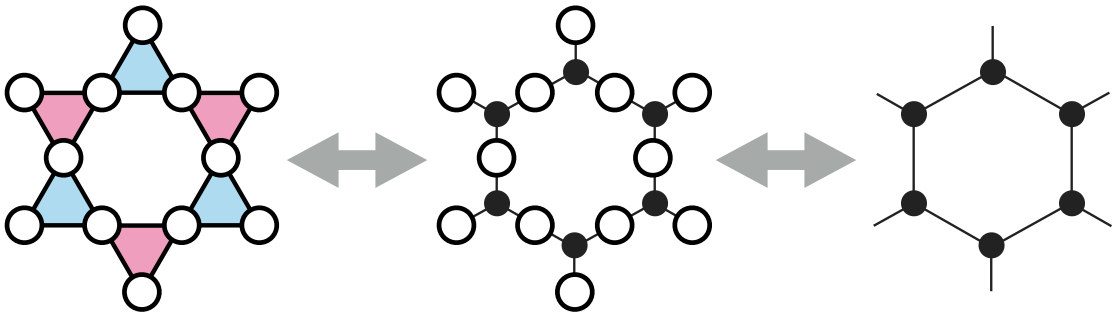

Figure 4.6: Graphical understanding of the transformation for the spin model defined by Eq. (4.35) into RBM and hidden-spin-only model. The original space is defined on the Kagomé lattice, in which the triangles are colored to denote the signs of three-spin interactions. The white open and red filled circles correspond to the visible and hidden spins, respectively. Also, the signs of the two-spin interactions are represented as solid and dotted lines for positive and negative, respectively.

is transformed as

$$\begin{aligned} \pi(\boldsymbol{\sigma}) &= \exp\left[\beta \sum_{\langle i,i'\rangle\in E} \sigma_i\sigma_{i'} + \sum_{\triangle} M_{\triangle}\tau_{\triangle} + \sum_{\triangledown} M_{\triangledown}\tau_{\triangledown}\right] && (4.36)\\ &= \Delta \sum_{\boldsymbol{h}} \exp\left[\sum_{\triangle} W_{\triangle}h_{\triangle} \sum_{i\in\triangle} \sigma_i + \sum_{\triangledown} W_{\triangledown}h_{\triangledown} \sum_{i\in\triangledown} \sigma_i + b \sum_{\triangle,\triangledown} (h_{\triangle} + h_{\triangledown})\right] \\ &= \sum_{h} \widetilde{\pi}(\boldsymbol{\sigma}, \boldsymbol{h}), && (4.37) \end{aligned}$$

where the parameters in the extended model are obtained by substituting $M_{\triangle(\triangledown)}$ and β into the STT, or Eq. (4.7). Note that the external fields on the visible spins are absent due to the cancellation caused by the alternating signs of the interactions. As is graphically described in Fig. 4.6, one hidden spin is embedded per triangle and denoted as $h_{\triangle}$ or $h_{\triangledown}$. The explicit expressions for the parameters can be read off from

$$\begin{aligned} \cosh(2W_{\triangle(\triangledown)}) &= \frac{e^{2\beta}\cosh(4\beta) - e^{-2\beta}}{[2\cosh(4\beta) - 2\cosh(4M)]^{1/2}}, && (4.38)\\ \sinh(2b) &= \frac{-\sinh(2W)\sinh(4M)}{|(\cosh(4\beta) - \cosh(4M))|}, && (4.39) \end{aligned}$$

where $W_{\triangle} = -W_{\triangledown} = W > 0$ and the signs of the parameters satisfy $\mathrm{sgn}(W_{\triangle(\triangledown)}) = \mathrm{sgn}(M_{\triangle(\triangledown)})$. Owing to the cancellation of the magnetic field on visible spins, we

obtain a simple expression by tracing out the visible spins as

$$\begin{aligned}\widetilde{\widetilde{\pi}}(\boldsymbol{h}) &= \sum_{\boldsymbol{\sigma}} \widetilde{\pi}(\boldsymbol{\sigma}, \boldsymbol{h}) \\ &= \Delta' \exp\left(-W_h \sum_{\langle j,j' \rangle \in \overline{E}} h_j h_{j'} + b \sum_{j \in \overline{V}} h_j \right), \end{aligned} \tag{4.40}$$

where Δ' is another renormalization factor, $\overline{E}$ and $\overline{V}$ are the sets of edges and vertices in the honeycomb lattice as is shown in the rightmost panel of Fig. 4.6. Note that the interaction is antiferromagnetic, reflecting the alternating signs of the three-spin interactions in the original space. The amplitude of the two-spin interaction is obtained by the DIT as

$$W_h = \operatorname{arc\,cosh}\left(e^{2W} \right) /2. \tag{4.41}$$

Although the model defined by Eq. (4.40) is not soluble at $b \neq 0$, an approximate solution of the transition point can be obtained by imposing some assumption after mapping the original model to an eight-vertex model [173]. This turns out to be fairly approximate but not exact, and hence we determine the transition point from the finite size scaling of the Binder ratio [174, 175].

As was introduced by Binder, the renormalization group theory leads us to assume the scaling law for the Binder ratio,

$$g := \frac{1}{2}\left(3 - \frac{\langle m^4 \rangle}{\langle m^2 \rangle^2} \right), \tag{4.42}$$

where m is the magnetization per site and $\langle \cdots \rangle$ denotes the thermal average. The scaling of this quantity in the vicinity of the critical temperature, T_{c}, is given as follows,

$$g \sim F\left(L^{1/\nu}(T - T_{\mathrm{c}}) \right), \tag{4.43}$$

where L is the linear system size, ν is the critical exponent for the correlation length, and F is an appropriate polynomial function, which has been taken to be cubic in this work. Shown in Fig. 4.7 are the results for ferromagnetic two-spin and alternating-sign three-spin interacting model on the Kagomé lattice with $M/\beta_c = 0.1$ and 0.2. From the data collapse in Fig. 4.7, we see that the scaling analysis is valid. The critical exponent ν is confirmed for numerous M/β to be in good agreement with $\nu = 1$, suggesting that the transition falls into the two-dimensional Ising universality class [176]. The simultaneously estimated quantity, i.e., the critical temperature T_{c}, is summarized in Fig. 4.8(a) together with the approximate solution given by Ref. [173].

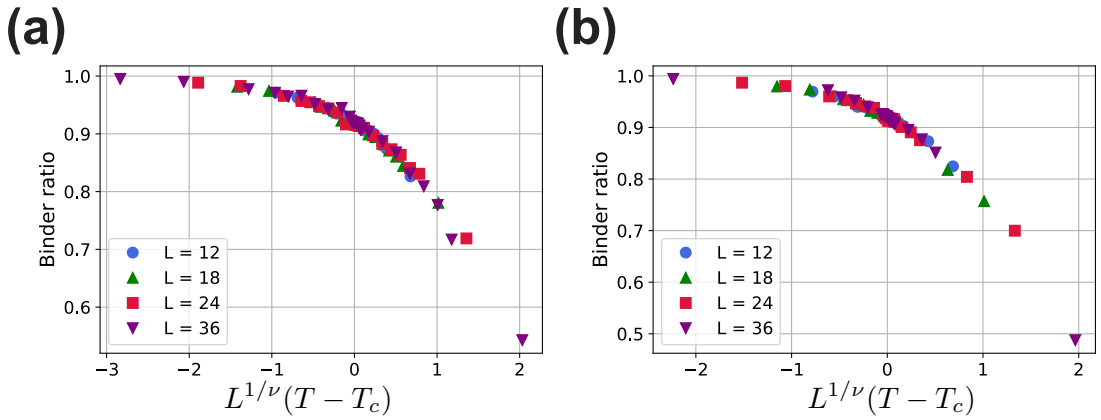

Figure 4.7: Data collapse of the Binder ratio for the Ising model with two-spin and alternating-sign three-spin interaction on the Kagomé lattice. The magnitude of two-spin interactions is set to unity while that of three-spin interactions is M/β_c = 0.1 and 0.2 for (a) and (b), respectively. the critical temperature and the critical exponent for the correlation length are obtained as (a) $T_c \sim 2.141$ and $\nu \sim 0.99$, (b) $T_c \sim 2.134$ and $\nu \sim 1.04$, respectively. The blue circles, green upward triangles, red squares, and purple downward triangles denote the data for the linear system sizes $L = 12, 18, 24$, and 36, respectively.

At the critical temperature, we focus on the representation by the BM and apply the cluster algorithm extended to deal with external magnetic field. [The detailed description on the algorithm is given in Appendix D.3.] Our main result is summarized in Fig. 4.8(b), in which we compare the autocorrelation time τ of the magnetization measured in units of Monte Carlo steps per site for the whole system. [See Appendix D.4 for the calculation of physical quantities in the extended space.] The magnetization at t-th Monte Carlo step is calculated from the spin configurations $\boldsymbol{\sigma}(t) = (\sigma_1(t), \sigma_2(t), ..., \sigma_{N_v}(t))$ with N_v being the number of visible spins as

$$m(t) = \sum_{i=1}^{N_v} \frac{\sigma_i(t)}{N_v}, \tag{4.44}$$

The estimation of τ is done by evaluating the decay of the equilibrium autocovariance [142],

$$A(t) = \frac{\langle |m(t_0 + t)m(t_0)| \rangle - \langle |m(t_0)| \rangle^2}{\langle |m(t_0)|^2 \rangle - \langle |m(t_0)| \rangle^2} = A_0 e^{-t/\tau}, \tag{4.45}$$

where $\langle \cdots \rangle$ denotes the average over t_0, namely the MC steps. The critical slow-

ing down is constantly observed in the SSF algorithm performed on the original space, while the application of the cluster update to the BM significantly improves the situation. We observe that the dynamical exponent z, which is the slope of data in Fig. 4.8(b), is also reduced, while the possibility that it gradually grows in the larger system sizes cannot be ruled out.

The increase in the autocorrelation time along the three-spin interaction M/β_c is understood in the following way. The virtual magnetic field induced in the hidden spins by the STT is amplified as M/β_c is increased, and thus the virtual magnetization per cluster increases, modifying the flipping probability of each cluster to be unbalanced. While the cluster is flipped randomly when the magnetic field is absent, finite-valued Zeeman energy results in unbalanced flipping probability due to the detailed balance condition. Such a situation prevents the system from exploring the spin configurations efficiently, and thus show a weaker speed up.

4.4 Summary of this Chapter

In the current work, we found an algebraic transformation of the Ising model with many-spin interactions into the BM in which only two-spin interactions and virtual local fields are present. The decoration-iteration and star-triangle transformations were applied to embed hidden and deep spins, namely the auxiliary degrees of freedom to be traced out. At the expense of the dimension of the spin space, significant suppression of the critical slowing down is achieved by applying the cluster algorithm to the BM.

We note that, in some specific many-spin interacting models, it is possible to introduce cluster-update algorithm with fewer auxiliary degrees of freedom by modifying the Fortuin-Kasteleyn transformation [15], which implicitly assumes application to models with finite-temperature phase transition in universality class such as the square Ising model or Potts model. In sharp contrast, the transformation technique introduced in our work allows us to apply arbitrary global update algorithm, and hence provide a general and systematic framework for models with arbitrary interaction in various lattice geometry.

Our scheme is also capable of handling continuous classical spin systems with many-spin interactions. As in the case with two-spin interactions [140], we may consider projecting each variable on some axis. Namely, we rewrite a continuous variable $\boldsymbol{S}_i$ on site i by a new Ising variable σ_i as $\boldsymbol{S}_i = \sigma_i |\boldsymbol{S}_i \cdot \boldsymbol{n}_i| \boldsymbol{n}_i + \boldsymbol{S}_i^{\perp}$, where $\boldsymbol{n}_i$ is the randomly chosen projection axis and $\boldsymbol{S}_i^{\perp}$ is orthogonal to $\boldsymbol{n}_i$. We can now

apply our method by regarding the model for $\{\sigma_i\}$ obtained by projection as the generalized Ising model. The randomness of the projection axis at each Monte Carlo step would assure the ergodicity of the scheme.

Beyond our scope in the current work is the optimal transformation for simulation. The transformation is non-unique when the virtual interaction is required, and we may even consider infinitely strong coupling to express extreme situations such as decoupled or completely aligned pairs of spins. Non-uniqueness arises also when four-spin interaction is present. Although we excluded the application of the star-square transformation for clarity, comparison of the numerical efficiency between different transformations may be worth investigating. Switching into different BMs for each step may allow us to explore the free energy landscape more efficiently.

In closing, we would like to note the applicability of the algebraic transformation to wider fields of research. One interesting direction is undoubtedly the pursuit of equilibrium statistical physics, which includes extending and exploring exactly soluble models and replacing the cluster-update algorithm by Swendsen and Wang with other global updates to tackle frustrated systems. Another problem lies in the field of computer science; the combinatorial optimization problems. Our decompositions, applicable also in the finite-temperature case, may open a new way to introduce ancilla spins required in the experimental implementation of annealing process.

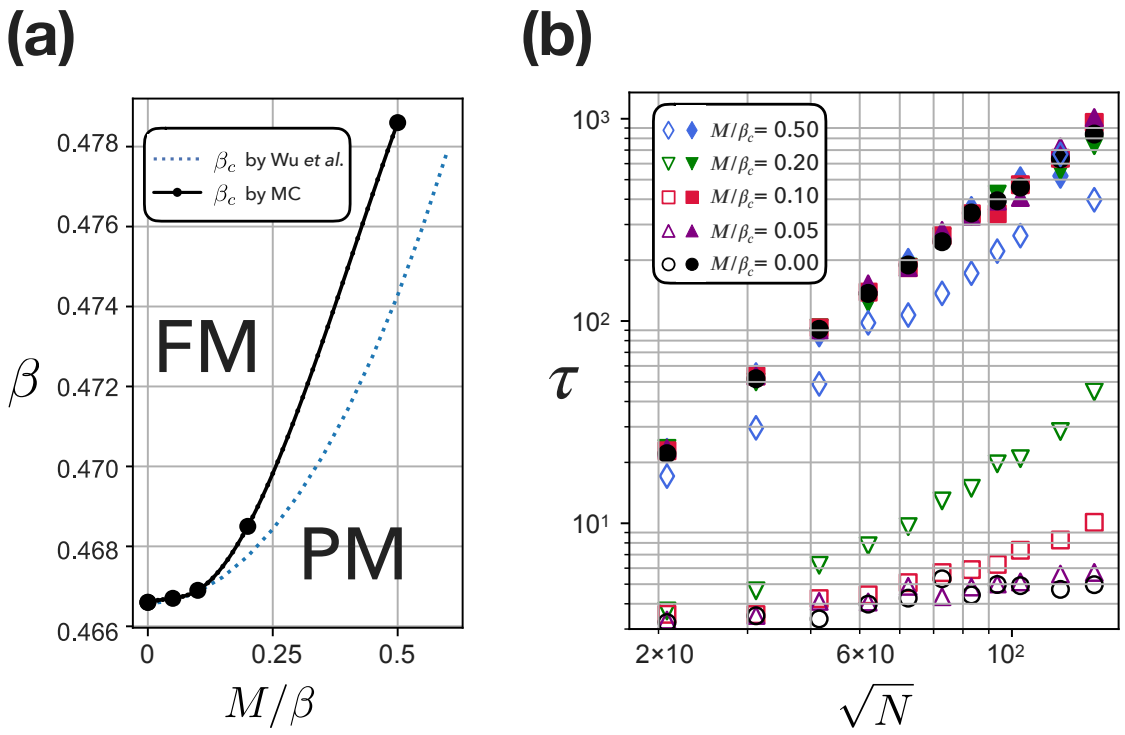

Figure 4.8: (a) The phase diagram of the model defined in Eq. (4.35). The boundary between the ferromagnetic (FM) and the paramagnetic (PM) phases are given here. The blue dotted line is calculated from the approximate solution in Ref. [173], and the black dots are given by the finite-size scaling of the Binder ratio. The numerically estimated inverse critical temperature at $M = 0$ approaches $\beta_c = \ln(3 + 2\sqrt{3})/4 \sim 0.4666$, which can be obtained from the exact solution [152]. (b) The autocorrelation time of the magnetization measured in units of Monte Carlo step. The black circle, purple upward triangle, red rectangle, green downward triangle, and blue diamond markers denote the magnitude of three-spin interactions to be $0, 0.05, 0.1, 0.2$, and 0.5, respectively. The filled (unfilled) markers represent the results by the single-spin flip in the original space (cluster update in the extended space).

5
Representation of Open Quantum Many-body Systems

In the present chapter, we study the approximate representation of stationary states in open quantum many-body systems by the neural-network quantum states. Using the high expressive power of the variational ansatz described by the restricted Boltzmann machines, which we dub as the neural stationary state ansatz in the following, we compute the stationary states of dynamics which obeys the time-homogeneous quantum master equation. The mapping of the stationary-state search problem into finding a zero-energy ground state of an appropriate Hermitian operator allows us to apply the conventional variational Monte Carlo method for the optimization. Our method is shown to simulate various dissipative spin systems efficiently, i.e., the transverse-field Ising models in both one and two dimensions and the XYZ model in one dimension.

5.1 Background

Despite its rapid progress, the approximation scheme of representation on quantum systems has yet to be applied to one of the most challenging problems in modern condensed matter physics – open quantum many-body systems. Although the astounding advancement of experiments [177–181] motivates an active research field on open quantum many-body physics, it is notoriously difficult to solve its fundamental equation of motion, which is often well captured by the time-homogeneous quantum master equation, or, the Gorini-Kossakowski-Sudarshan-Lindblad (GKSL) equation [182, 183]. Since the number of parameters required for exact description grows in proportion to the square of the Hilbert space dimension, additional numerical cost is required to capture the mixed states compared to the pure states in closed systems. Accordingly, the simulation of the GKSL equation with the exact diagonalization method is hard even for relatively small system sizes. It is thus important whether the approximate representation is beneficial to simulate open quantum many-body physics. Par-

ticularly intriguing are nonequilibrium stationary states of dynamics, in which various exotic structure are exhibited: the entanglement [184, 185], nontrivial topology [186, 187], and novel dissipative phases of matter [188–192].

We remark that there have been previous proposals for simulating open quantum many-body systems numerically. For example, the dissipative dynamics is simulated by the density matrix renormalization group [193–197] under the tensor network representation, which works very well especially in 1d as long as the operator space entanglement entropy of the density matrix is small. In addition, numerous works have focused particularly on the stationary states of the dissipative dynamics. Cui et al. [198] presented an elegant variational method to search for the stationary states of the dissipative dynamics by minimizing the expectation value of $\hat{\mathcal{L}}^\dagger\hat{\mathcal{L}}$ using the Matrix Product Operator (MPO) algorithm, which is powerful for 1d systems. Beyond 1d, Ref. [199] treated variational quantum states that take low-order correlations around the product states into account. It is also notable that certain approximations beyond the mean-field theory, e.g., the cluster mean-field theory [200, 201], were employed. Few methods besides the brute-force exact diagonalization have been proposed, however, that can efficiently capture quantum correlations beyond 1d [196, 197]. The quantum jump method, which consider dynamics of pure states that stochastically undergo "jump" caused by dissipation, would require a large amount of sampling when the steady state is thermal, and the variational calculation based on the tensor network ansatz is not as overwhelming in higher dimensions as in 1d.

To overcome this situation, we present a new scheme named the neural stationary state (NSS) algorithm for simulating the stationary states of open quantum many-body systems by employing the complex-valued restricted Boltzmann machine (cRBM) ansatz whose construction does not rely on the spacial dimension of the system. Due to the dimension-free structure and the capacity of representing large quantum entanglement, the cRBM ansatz is expected to be advantageous in simulating higher-dimensional systems or real/imaginary time evolution. As is schematically illustrated in Fig. 5.1, the overview of the NSS algorithm constitutes the following four steps:

(a) *Define cost function.* Given non-Hermitian operator $\hat{\mathcal{L}}$, or the Liouvillian, that generates the time evolution of the dynamics, consider a Hermitian positive-semidefinite operator $\hat{\mathcal{L}}^\dagger\hat{\mathcal{L}}$ whose "groundstate" corresponds to the stationary state.

(b) *Choose ansatz.* We take the cRBM as the variational ansatz for the stationary state in the current thesis. The volume-law scaling of entanglement entropy in the vector representation, namely the operator space entanglement entropy, is also discussed [202, 203].

(c) *Choose optimization strategy.* The optimization is done by the stochastic reconfiguration which is equivalent to imaginary time evolution based on Monte Carlo sampling.

(d) *Run optimization.* Update the parameters until termination condition, e.g., iteration counts or magnitude of cost function, is satisfied.

Before providing the detailed information on the algorithm, we first give a concise introduction to the GKSL formalism of open quantum system. After elaborating on the steps (a)-(d) of the NSS algorithm, we finally demonstrate the capability of calculating the stationary states of the dissipative transverse-field Ising models in 1d and 2d, and XYZ model in 1d.

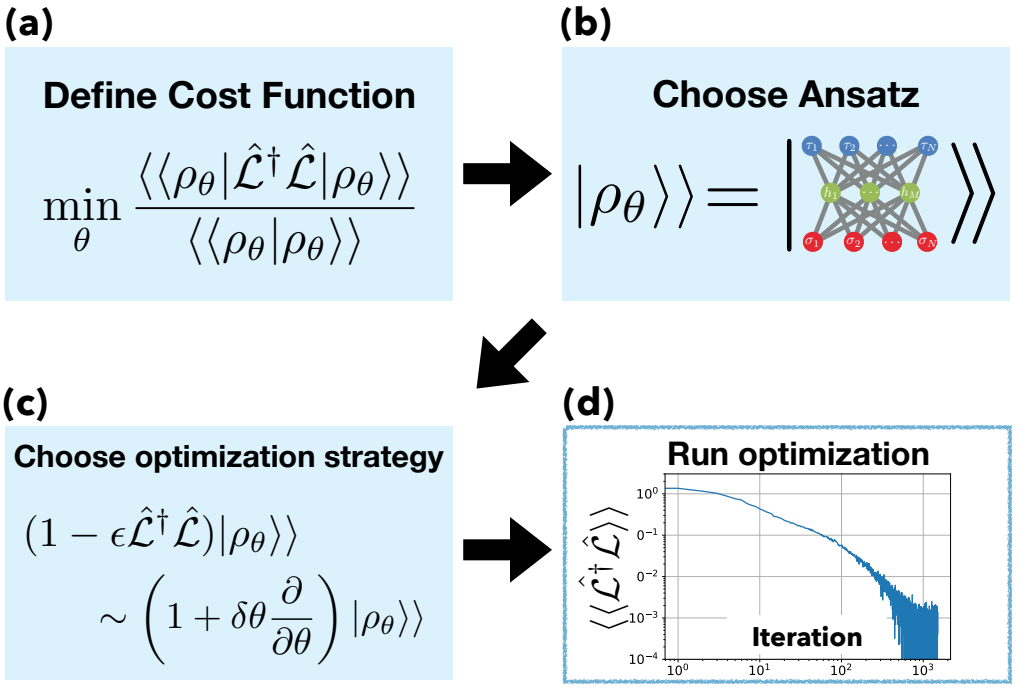

Figure 5.1: Overview of the Neural Stationary State (NSS) algorithm.

5.2 Formalism of Open Quantum System

Quantum systems are inevitably subject to interaction between uncontrollable external environment. Open quantum systems handle with effective dynamics of the system with the environment, which is usually macroscopic and hence cumbersome to take into account directly, traced out. Depending on the physical requirement imposed, numerous formalism exists for such a setup. In the current thesis, we consider the most standard Gorini-Kossakowski-Sudarshan-Lindblad (GKSL) formalism that yields completely-positive trace-preserving time evolution with Markovianity.

5.2.1 Physical requirements

For the sake of illustration, let us denote the Hilbert space of the system S which we are interested in as $\mathcal{H}_S$ and that of the external environment E as $\mathcal{H}_E$. Correspondingly, the total Hilbert space of the composite system is denoted as $\mathcal{H}_{\text{tot}} = \mathcal{H}_S \otimes \mathcal{H}_E$. We may also use subscripts S and E for operators to clarify which space they act on.

completely-positive trace-preserving (CPTP) property The CPTP property is a combination of complete positivity and trace-preserving property. Let us first remind the *positivity* of a quantum operation expressed by a superoperator Φ_S which maps an operator into another one. We say that Φ_S is positive if $\Phi_S(A_S)$ has a positive spectrum for any positive operator A_S that acts on the system Hilbert space $\mathcal{H}_S$. Furthermore, the *complete positivity* takes the external environment into account. Namely, Φ_S is completely positive if an operation in the total space $(\Phi_S \otimes \mathbb{1}_E)$ is positive for arbitrary dimension of the environment space $\mathcal{H}_E$. This is a much stronger condition than the mere positivity[*1], yet physically natural for quantum operations on quantum states since the environment can be extended arbitrarily. Trace-preserving property, on the other hand, requires a quantum operation Φ_S to satisfy $\text{Tr}[\hat{\rho}_S] = \text{Tr}[\Phi_S(\hat{\rho}_S)] = 1$ for arbitrary density matrix $\hat{\rho}_S$. This allows us to interpret the mapped state $\Phi_S(\hat{\rho}_S)$ as another quantum state that satisfies physical requirement.

The representation theorem given by Kraus [206] states that linear operation Φ_S satisfies the CPTP property if and only if there exists a set of operators such

[*1] For instance, the transpose operation $T_S(\hat{\rho}_S) = \hat{\rho}_S^{\text{T}}$ is a positive but not completely positive operation. Namely, $\hat{\rho}_S^{\text{T}}$ is positive, although $(T_S \otimes \mathbb{1}_E)(\hat{\rho}_{\text{tot}})$ is not necessarily positive [204, 205].

that

$$\Phi_S(\hat{\rho}) = \sum_k \hat{M}_k \hat{\rho} \hat{M}_k^\dagger, \tag{5.1}$$

$$\sum_k \hat{M}_k^\dagger \hat{M}_k = \mathbb{1}_S, \tag{5.2}$$

where $\hat{M}_k$ is called the Kraus operator that specify the quantum operation. Note that the choice of Kraus operator is not unique.

Markovianity A continuous-time stochastic process with Markovianity is described by time evolution equation that is independent from its memory. This condition originates from a physical assumption that the time scale of the decay of dynamics in system τ_S is much longer than that of the environment τ_E, namely $\tau_S \gg \tau_E$. Under such approximation, we may readily assume that the time evolution of the quantum state is given as $\frac{d\hat{\rho}}{dt} = \Phi(\hat{\rho})$ where $\Phi : \mathcal{H}_S \otimes \mathcal{H}_S \to \mathcal{H}_S \otimes \mathcal{H}_S$ is a superoperator that maps a matrix into matrix.

5.2.2 GKSL formalism in matrix representation

The two requirements for the evolution in open quantum system given in the previous section yield the quantum Markovian equation in the simplest GKSL formalism [182, 183].

Concretely, the time evolution of a mixed state $\hat{\rho}(t)$ is described under the GKSL formalism as follows,

$$\frac{d\hat{\rho}(t)}{dt} = \mathcal{L}\hat{\rho}(t) := -i[\hat{H}, \hat{\rho}(t)] + \sum_k \gamma_k \mathcal{D}[\hat{c}_k]\hat{\rho}(t). \tag{5.3}$$

where $\mathcal{L}$ is the Liouvillian superoperator, a linear map that maps a density matrix into another density matrix. The first term in the right hand side, given by the commutator $[\hat{H}, \hat{\rho}] = \hat{H}\hat{\rho} - \hat{\rho}\hat{H}$, describes the unitary dynamics ruled by the Hamiltonian $\hat{H}$. The second term describes the non-unitary dynamics due to the dissipations. The contribution of the k-th term, whose strength is given as $\gamma_k > 0$, is governed by a superoperator $\mathcal{D}[\hat{c}_k]$ acting on the density matrix $\hat{\rho}(t)$ as

$$\mathcal{D}[\hat{c}_k]\hat{\rho}(t) = \hat{c}_k \hat{\rho}(t) \hat{c}_k^\dagger - \frac{1}{2}\hat{c}_k^\dagger \hat{c}_k \hat{\rho}(t) - \frac{1}{2}\hat{\rho}(t)\hat{c}_k^\dagger \hat{c}_k. \tag{5.4}$$

Here, the detail of the non-unitary dynamics induced by the interaction between the system and bath is determined by the set of (non-Hermitian) operators $\{\hat{c}_k\}$.

As we shortly see in the next paragraph, the operators are related to the quantum jumps and hence referred to as the "jump operators."

We may concisely check that the dynamical map given by Eq. (5.3) satisfies the CPTP property. Let the system evolve for an infinitesimally small time step Δt. Obtaining $\hat{\rho}(t+\Delta t) - \hat{\rho}(t) = \mathcal{L}[\hat{\rho}(t)]\Delta t$, we find that the evolved state can be written up to the first order in Δt as follows,

$$\begin{aligned} \hat{\rho}(t+\Delta t) &= \hat{M}_0 \hat{\rho}(t) \hat{M}_0^\dagger + \sum_k \hat{M}_k \hat{\rho}(t) \hat{M}_k^\dagger, \\ \hat{M}_0 &= \mathbb{1}_S + \left(-i\hat{H} - \frac{1}{2}\gamma_k \hat{c}_k^\dagger \hat{c}_k \right) \Delta t, \\ \hat{M}_k &= \hat{c}_k \sqrt{\gamma_k \Delta t}, \end{aligned} \tag{5.5}$$

which is the Kraus representation given in Eq. (5.1). While the Kraus representation of quantum operation in general is not unique, the expression by Eq. (5.5) gives us intuitive understanding that the Kraus operators $\hat{M}_k$ describes the "quantum jump" induced by the operator $\hat{c}_k$.

5.2.3 GKSL formalism in vector representation

In Sec. 5.2.2 the generator of the time evolution was given by a superoperator, it would be more convenient if it is given as an ordinary operator which is independent of the state[*2]. In the following, we introduce the vector representation of the GKSL equation, which later turns out to be beneficial in terms of variational calculation of the stationary states.

To investigate the property of the mapping Φ such as the Liouvillian or quantum channel, it is useful to introduce the Choi-Jamiołkowski isomorphism [207, 208]. Here, we take an auxiliary Hilbert space $\mathcal{H}_A$ with an identical dimension as the original one $\mathcal{H}_P$. For simplicity, we abbreviate the subscript unless necessary. Let us consider a matrix $\phi : \mathcal{H} \otimes \mathcal{H} \to \mathcal{H} \otimes \mathcal{H}$ with its matrix elements given as

$$(\phi)_{(\sigma\sigma'),(\tau,\tau')} = \langle \sigma | \left(\Phi(|\sigma'\rangle \langle \tau'|) \right) |\tau\rangle , \tag{5.6}$$

where σ and τ denote computational bases that span $\mathcal{H}_P$. This mapping from the superoperator Φ from matrix ϕ is called the Choi-Jamiołkowski isomorphism. It is instructive to note that the quantum states are also mapped from a density "matrix" $\hat{\rho}$ to an element of the Hilbert space with a doubled dimension, or the

[*2] While it is possible to rewrite Liouvillian in the matrix representation as an operator, its action would be dependent on the quantum state $\hat{\rho}$.

operator space. The correspondence between the quantum state and the mapped pure state is explicitly given as

$$\hat{\rho} = \sum_{\sigma,\tau} \rho_{\sigma\tau} |\sigma\rangle \langle\tau| \quad \mapsto |\rho\rangle\rangle = \frac{1}{C} \sum_{\sigma,\tau} \rho_{\sigma\tau} |\sigma,\tau\rangle\rangle, \tag{5.7}$$

where $|\sigma,\tau\rangle\rangle = |\sigma\rangle \otimes |\tau\rangle \in \mathcal{H} \otimes \mathcal{H}$ denotes a computational basis that spans $\mathcal{H} \otimes \mathcal{H}$ and $C = \sqrt{\sum_{\sigma,\tau} |\rho_{\sigma\tau}|^2}$ is the normalization factor. To discriminate the spins in the doubled Hilbert space, we refer to those denoted by $\sigma(\tau)$ as the physical(fictitious) spins. Note that the normalization of the states are different in the matrix and vector representations; in the former the trace of the matrix is set to unity, i.e., $\sum_\sigma \rho_{\sigma\sigma} = 1$, whereas the L^2-norm of $|\rho\rangle\rangle$, or $\langle\langle\rho|\rho\rangle\rangle$, is unity in the latter.

Given the mapping by Eqs. (5.6) and (5.7), we may write down the GKSL equation in the vector representation. The product of operators and the density matrix is mapped as

$$\hat{A}\hat{\rho}\hat{B} = \sum_{\sigma\mu\nu\tau} A_{\sigma\mu}\rho_{\mu\nu}B_{\nu\tau} |\sigma\rangle \langle\tau|, \tag{5.8}$$

$$\mapsto \hat{A} \otimes \hat{B}^T |\rho\rangle\rangle = \frac{1}{C} \sum_{\sigma\mu\nu\tau} A_{\sigma\mu}\rho_{\mu\nu}(B^T)_{\tau\nu} |\sigma,\tau\rangle\rangle \tag{5.9}$$

$$= \hat{A} \otimes \hat{B}^T |\rho\rangle\rangle, \tag{5.10}$$

where $\hat{A}$ and $\hat{B}$ are the operators that act from left and right, respectively. Applying Eqs. (5.8) to the original expression given by Eq. (5.3), we finally obtain the vector representation of the GKSL equation as follows,

$$\begin{aligned} \frac{d|\rho(t)\rangle\rangle}{dt} &= \hat{\mathcal{L}} |\rho(t)\rangle\rangle \\ &= \left(-i(\hat{H} \otimes \mathbb{1} - \mathbb{1} \otimes \hat{H}^T) + \sum_k \gamma_k \hat{\mathcal{D}}[\hat{c}_k] \right) |\rho(t)\rangle\rangle, \end{aligned} \tag{5.11}$$

where $\hat{\mathcal{L}} : \mathcal{H} \otimes \mathcal{H} \to \mathcal{H} \otimes \mathcal{H}$ is the Liouvillian in the vector representation. Here, the hat symbol ($\hat{}$) is added to explicitly show that the superoperator is mapped into an operator. Also the jump operators are given as

$$\hat{\mathcal{D}}[\hat{c}_k] = \hat{c}_k \otimes \hat{c}_k^* - \frac{1}{2}\hat{c}_k^\dagger \hat{c}_k \otimes \mathbb{1} - \mathbb{1} \otimes \frac{1}{2}\hat{c}_k^T \hat{c}_k^*. \tag{5.12}$$

5.2.4 Spectrum of Liouvillian

As we have noted in §5.2.2, the Liouvillian consists of two types of terms: those corresponding to the unitary dynamics governed by the Hamiltonian and

those describing the non-unitary dynamics governed by the jump operators. From its vector representation, Eq. (5.11) we can see that the former yields anti-Hermitian matrix elements, which does not hold for the latter. Therefore, the spectrum of the Liouvillian is in general distributed in the complex plane $\mathbb{C}$.

The CPTP operator describing the time evolution $e^{\mathcal{L}t}$, which is often referred to as the quantum channel, can be shown to have eigenvalues with non-positive real parts [209]. See Fig. 5.2(a) for a pictorial illustration. States in physical systems associated with a strictly negative real eigenvalue undergoes a trajectory with decay, while those corresponding to the kernel of $\mathcal{L}$ would survive after infinitely long time. It is shown that there are at least one zero-eigenvalue for a Liouvillian that is time-homogeneous. Such a physical state corresponding to the kernel of the Liouvillian, which is a mixed state in general, is called *the stationary state* [209].

Although there may emerge multiple stationary states depending on the setup, in the following we exclusively consider systems with unique stationary states, which are confirmed to be present in various systems. For example, if the annihilation operator, or the incoherent spin flip along the z-axis in the language of spins, is included as the dissipation for each site, the quantum system has a unique stationary state regardless of the Hamiltonian [210]. Unique stationary states also appear for other types of dissipations, as demonstrated in, e.g., Refs. [193, 211, 212].

Note that a stationary state is equivalent in two representations. Since the Choi-Jamiołkowski isomorphism introduced in Eq. (5.6) is a one-to-one mapping, the vector representation of an element of kernel of $\mathcal{L}$ is a null vector of $\hat{\mathcal{L}}$. More concretely, we find

$$\mathcal{L}[\hat{\rho}] = 0 \Longleftrightarrow \hat{\mathcal{L}}\,|\rho\rangle\rangle = 0. \tag{5.13}$$

Furthermore, the right-hand side of Eq. (5.13) can be considered as a condition regarding the L_2 norm of the state as

$$||\hat{\mathcal{L}}\,|\rho\rangle\rangle||^2 = 0 \Longleftrightarrow \langle\langle\rho|\hat{\mathcal{L}}^\dagger\hat{\mathcal{L}}|\rho\rangle\rangle = 0 \Longleftrightarrow \hat{\mathcal{L}}^\dagger\hat{\mathcal{L}}\,|\rho\rangle\rangle = 0. \tag{5.14}$$

The equivalence between the equations in the middle and the right-most follows from the fact that the operator $\hat{\mathcal{L}}^\dagger\hat{\mathcal{L}}$ is by construction a positive-semidefinite Hermitian operator. In other words, the kernels of $\hat{\mathcal{L}}^\dagger\hat{\mathcal{L}}$ and $\hat{\mathcal{L}}$ are identical to each other. [See Fig. 5.2(b) for the graphical description.] As we see in the following

subsections, the relationship denoted by Eq. (5.14) allows us to apply the well-established ground-state search technique in closed systems such as the variational approaches, in addition to the Lanczos method, if the first excited energy of $\hat{\mathcal{L}}^\dagger\hat{\mathcal{L}}$ does not vanish [198]. The expectation value $\langle\langle\rho|\hat{\mathcal{L}}^\dagger\hat{\mathcal{L}}|\rho\rangle\rangle$ is suited for the cost function in the variational Monte Carlo method.

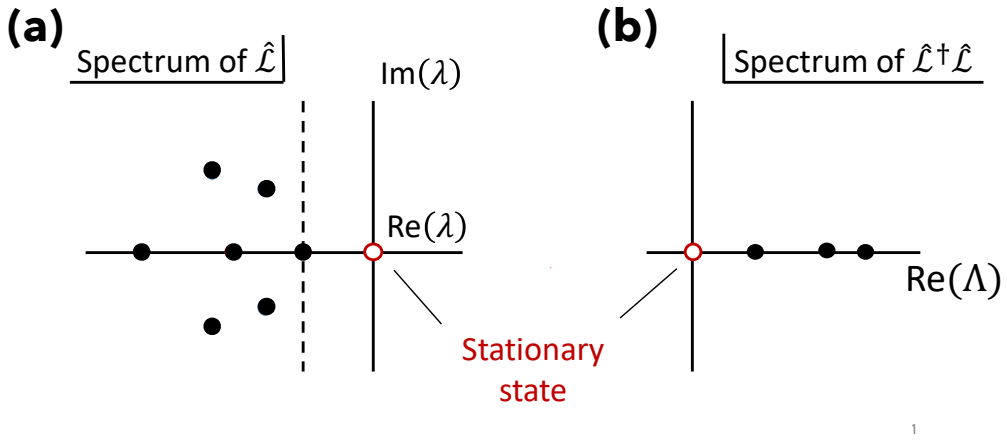

Figure 5.2: Spectrum of (a) the Liouvillian $\hat{\mathcal{L}}$ and (b) the product of its Hermitian conjugate and itself, i.e., $\hat{\mathcal{L}}^\dagger\hat{\mathcal{L}}$. The white unfilled and black filled circles denote the stationary states and decaying modes, repectively. The distance between the imaginary axis and the dashed line gives the reciprocal of the longest decay time of non-stationary states. The real parts of eigenvalues of $\hat{\mathcal{L}}$ are non-positive, which reflects that non-stationary modes would decay along time evolution. Note that the spectrum shown in (b) is by definition real. In the current thesis, we consider systems that can be shown to have unique stationary states.

5.3 Stationary States

As we have discussed in the previous section, the stationary states are the null space of the Liouvillian operator. We firstly give an instructive example of stationary states that can be analytically computed in a two-level system. Next, we introduce the variational ansatz, represented by the cRBM, for a stationary state of a given many-body system. After the numerical verification of its capability to express highly-entangled quantum states, we discuss our optimization algorithm to express the stationary state.

5.3.1 Stationary states in two-level system

Let us assume a system consisting of a single qubit, namely a two-level system, with the two computational basis separated by some gap Δ. Here, the Hamiltonian of the system is given as

$$H = \frac{\Delta}{2}\hat{\sigma}^z. \tag{5.15}$$

Such an elementary setup is crucial in quantum experiments, and hence realized in numerous systems such as the superconducting qubits, trapped ions, Rydberg atoms, and so on. Among the decoherence effects caused by the external environment, we consider two types of dissipation: the damping and dephasing. The damping is usually considered to include the effect of the energy loss, or equivalently the spontaneous emission, and the dephasing is a term that kills the quantum superposition. The GKSL equation with such terms in the matrix representation is given as

$$\frac{\hat{\rho}(t)}{dt} = -i\frac{\Delta}{2}[\hat{\sigma}^z, \hat{\rho}(t)] + \gamma_1 \mathcal{D}[\hat{\sigma}^-]\hat{\rho}(t) + \frac{\gamma_\phi}{2}\mathcal{D}[\hat{\sigma}^z]\hat{\rho}(t), \tag{5.16}$$

where γ_1 and γ_ϕ gives the amplitude of the damping and dephasing, respectively. It is useful to introduce the notation by the Bloch vector to represent the state as

$$\hat{\rho(t)} = \frac{1}{2}[\hat{\mathbb{1}} + x(t)\hat{\sigma}^x + y(t)\hat{\sigma}^y + z(t)\hat{\sigma}^z] = \frac{1}{2}\begin{pmatrix} 1+z(t) & x(t)-iy(t) \\ x(t)+iy(t) & 1-z(t) \end{pmatrix}, \tag{5.17}$$

where each element is given as $x(t) = \mathrm{Tr}[\hat{\rho}(t)\hat{\sigma}^x]$, $y(t) = \mathrm{Tr}[\hat{\rho}(t)\hat{\sigma}^y]$, and $z(t) = \mathrm{Tr}[\hat{\rho}(t)\hat{\sigma}^z]$ with restriction due to the positive-semidefiniteness of the density matrix, $x^2(t) + y^2(t) + z^2(t) \leq 1$. This can be solved analytically as [213]

$$\hat{\rho}(t) = \frac{1}{2}\begin{pmatrix} (z(0)+1)e^{-\gamma_1 t} & e^{-\gamma_2 t}(x(t)e^{-i\Delta t} - iy(0)e^{i\Delta t}) \\ e^{-\gamma_2 t}[x(0)e^{i\Delta t} + iy(0)e^{-i\Delta t}] & 2-(z(0)+1)e^{-\gamma_1 t} \end{pmatrix}, \tag{5.18}$$

where $\gamma_2 = \gamma_1/2 + \gamma_\phi$.

Shown in Fig. 5.3 is the visualization of Eq. (5.18) on the Bloch sphere. We plot the trajectories with various initial pure state under mere damping, i.e., $\gamma_1 = 2$ and $\gamma_{\phi=0}$, in Fig. 5.3(a) and the ones under dephasing, i.e., $\gamma_1 = 0, \gamma_\phi = 0.5$, in Fig. 5.3(b). Under the damping, it is clear that the state always evolves into the ground state, while this is not the case when non-diagonal terms are present in the Hamiltonian. On the other hand, under the dephasing, the system loses quantum

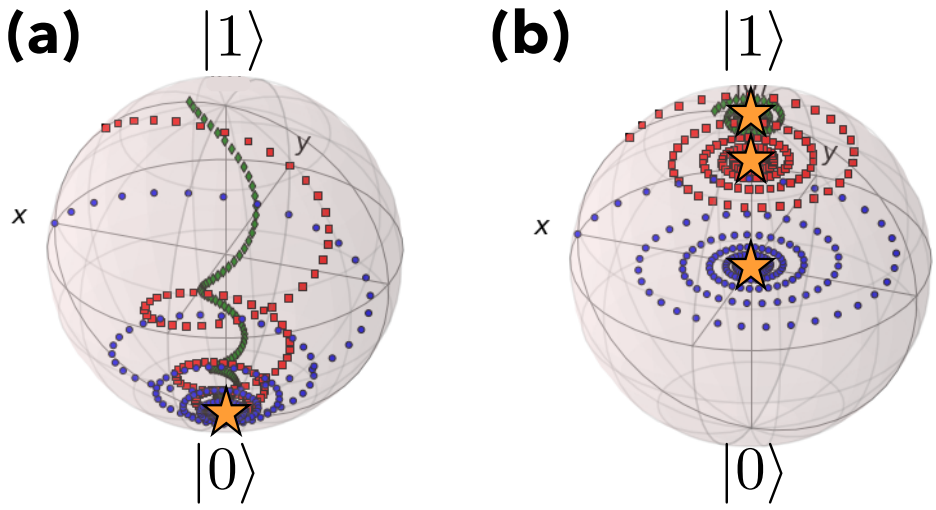

Figure 5.3: A single-qubit with its computational basis, $|0\rangle$ and $|1\rangle$ separated by gap Δ under (a) damping and (b) dephasing. The trajectory of the quantum states are plotted on the Bloch sphere. Here, the parameters defined in Eq. (5.16) are given as $\gamma_1 = 2, \gamma_\phi = 0$ in (a) and $\gamma_1 = 0, \gamma_\phi = 0.5$ in (b). The green diamond, red rectangle, and blue circles represent the different initial pure states corresponding to $r = 0.5$, 0.7, and 0.9, respectively. The stationary states are denoted by the yellow stars.

coherence and the non-diagonal parts of the density matrix decays. Note that the initial pure state in Fig. 5.3 is given as

$$|\psi_0\rangle = \frac{1}{\sqrt{r^2 + (1-r)^2}} \left((1-r)\,|0\rangle + r\,|1\rangle \right), \tag{5.19}$$

where $|0(1)\rangle$ denotes the ground (excited) state of the qubit.

5.3.2 Stationary states in many-body system

The size of the Liouvillian of N-qubit system is $4^N \times 4^N$ in the vector representation, and hence the full spectrum of larger systems becomes intractable. To overcome this problem, in the current thesis we develop an algorithm based on the variational Monte Carlo (VMC) method, which is a very powerful numerical technique to investigate the ground states, excited states, and time evolution in many-body quantum systems.

The main philosophy of the VMC method is given as follows. The Rayleigh-Ritz variational principle states that the lowest eigenvector $|\psi_0\rangle$ of a given Her-

mitian operator $\hat{A} = \hat{A}^\dagger$ can be obtained as

$$|\psi_0\rangle = \arg\min_{|\psi\rangle} \frac{\langle\psi|\hat{A}|\psi\rangle}{\langle\psi|\psi\rangle}, \tag{5.20}$$

where the minimization takes the whole space into account. In practice, the size of the whole space considered in, e.g., quantum physics or chemistry is enormous so that exhaustive exploration becomes numerically unrealistic. One may employ, however, some parametrized trial state, or the ansatz, $|\psi_\theta\rangle$, to *approximate* the lowest eigenstate by $|\psi_{\widetilde{\theta}}\rangle$ as

$$|\psi_{\widetilde{\theta}}\rangle = \arg\min_{|\psi_\theta\rangle} \frac{\langle\psi_\theta|\hat{A}|\psi_\theta\rangle}{\langle\psi_\theta|\psi_\theta\rangle}. \tag{5.21}$$

Its accuracy such as the fidelity with the exact solution depends crucially on the expressive power of the ansatz and also the strategy of the optimization.

In the following, we introduce our **neural stationary state (NSS) algorithm**, which partly relies on the VMC method, to construct the stationary state of a given open quantum many-body system. The NSS algorithm is summarized in four steps as

(a) Define cost function.

(b) Choose ansatz.

(c) Choose optimization strategy.

(d) Run optimization.

which are explained in detail in the following.

(a) Define Cost Function

As we have discussed in §5.2, the stationary state corresponds to "the ground state" of the Hermitian operator $\hat{\mathcal{L}}^\dagger\hat{\mathcal{L}}$. The stationary state can thus be obtained via optimization of variational parameters as in Eq. (5.21). Namely, the best approximation given by the optimal parameters $\widetilde{\theta}$ can be obtained by

$$|\rho_{\widetilde{\theta}}\rangle\rangle = \arg\min_{|\rho_\theta\rangle\rangle} \frac{\langle\langle\rho_\theta|\hat{\mathcal{L}}^\dagger\hat{\mathcal{L}}|\rho_\theta\rangle\rangle}{\langle\langle\rho_\theta|\rho_\theta\rangle\rangle}, \tag{5.22}$$

where $|\rho_\theta\rangle$ is the ansatz with variational parameters θ. The subscript for ansatz would be abbreviated in the following for simplicity. The cost function C is evaluated via the Monte Carlo sampling instead of the brute-force calculation as follows,

$$\begin{aligned} C &= \frac{\langle\langle\rho|\hat{\mathcal{L}}^\dagger\hat{\mathcal{L}}|\rho\rangle\rangle}{\langle\langle\rho|\rho\rangle\rangle} \\ &= \frac{\sum_{\sigma,\tau,\sigma',\tau'}\langle\langle\rho|\sigma,\tau\rangle\rangle\langle\langle\sigma,\tau|\hat{\mathcal{L}}^\dagger\hat{\mathcal{L}}|\sigma',\tau'\rangle\rangle\langle\langle\sigma',\tau'|\rho\rangle\rangle}{\sum_{\sigma,\tau}\langle\langle\rho|\sigma,\tau\rangle\rangle\langle\langle\sigma,\tau|\rho\rangle\rangle} \\ &= \frac{\sum_{\sigma,\tau,\sigma',\tau'}(\rho^*_{\sigma\tau})(\hat{\mathcal{L}}^\dagger\hat{\mathcal{L}})_{(\sigma\tau),(\sigma'\tau')}\rho_{\sigma'\tau'}}{\sum_{\sigma\tau}|\rho_{\sigma\tau}|^2} \\ &= \frac{\sum_{\sigma\tau}|\rho_{\sigma\tau}|^2 E^{\mathrm{loc}}_{\sigma\tau}}{\sum_{\sigma\tau}|\rho_{\sigma\tau}|^2} \\ &= \frac{\sum_{(\sigma\tau)\in\mathcal{D}} E^{\mathrm{loc}}_{\sigma\tau}}{\sum_{(\sigma\tau)\in\mathcal{D}} 1} = \frac{1}{|\mathcal{D}|}\sum_{(\sigma\tau)\in\mathcal{D}} E^{\mathrm{loc}}_{\sigma\tau}, \end{aligned} \tag{5.23}$$

where $\rho_{\sigma\tau}$ is the element of the density matrix ansatz in the vector representation, $\mathcal{D} = \{(\sigma_m,\tau_m)\}_{m=1}^M$ is the set of M spin configurations drawn from the probability distribution $P(\sigma,\tau) \propto |\rho_{\sigma,\tau}|^2$. In the current thesis, we employ the Metropolis-Hastings rule to perform the single-spin flip update. [See Appendix D for details.] A sample is taken as the spin configuration realized after each sweep over the whole spin. In the fourth line of Eq. (5.23), we introduce the local energy as a diagonal matrix as follows,

$$\begin{aligned} \hat{E}^{\mathrm{loc}} &= \mathrm{diag}\{E^{\mathrm{loc}}_{\sigma,\tau}\}_{(\sigma,\tau)}, \\ E^{\mathrm{loc}}_{\sigma,\tau} &= \sum_{\sigma',\tau'}\frac{\rho_{\sigma'\tau'}}{\rho_{\sigma\tau}}(\hat{\mathcal{L}}^\dagger\hat{\mathcal{L}})_{(\sigma\tau,\sigma'\tau')}, \end{aligned} \tag{5.24}$$

which can be calculated efficiently for local operators.

(b) Choose Ansatz

As the variational ansatz $|\rho_\theta\rangle\rangle$, we consider the cRBM. Let us remind that the explicit expression of the ansatz can be written as follows,

$$\begin{aligned} \langle\langle\sigma,\tau|\rho_{\mathrm{RBM}}\rangle\rangle = \frac{1}{Z}\sum_{\{h_j\}}&\exp\left(\sum_{i,j}W_{ij}\sigma_i h_j + \bar{W}_{ij}\tau_i h_j\right) \\ &\times\exp\left(\sum_i a_i\sigma_i + \bar{a}_i\tau_i + \sum_j b_j h_j\right), \end{aligned} \tag{5.25}$$

where W_{ij} ($\bar{W}_{ij}$) denotes the complex interaction amplitude between the i-th physical (fictitious) spin σ_i (τ_i) and j-th hidden spin h_j, a_i ($\bar{a}_i$) is a complex magnetic field on the i-th physical (fictitious) spin, and b_j is a complex magnetic field on the j-th hidden spin. The normalization factor Z is determined such that $\langle\langle\rho_{\mathrm{RBM}}|\rho_{\mathrm{RBM}}\rangle\rangle = 1$. Denoting the number of the physical, fictitious, and hidden spins as $N, \bar{N}(= N)$, and M, respectively, we define the number ratio of the spins as $\alpha = M/(N + \bar{N})$ to compare the performance of the cRBM ansatz under different system sizes. The graphical illustration of the ansatz is provided in Fig. 5.4(a).

The matrix representation of the state given by Eq. (5.25), or $\hat{\rho}_{\mathrm{RBM}}$, does not in general satisfy the physical conditions required for density matrices: the positive-semidefiniteness and Hermiticity. While we may impose symmetry in the parameters so that the conditions are fulfilled [214], we observe that such restriction worsens the performance of the stochastic reconfiguration method used for the optimization of the parameters. To ensure the two conditions, we may as well employ the vanilla stochastic gradient descent.

We argue that, on the other hand, sufficient optimization of the cost function without parameter constraints is expected to ensure these two conditions in an approximated way [198]. In fact, we have confirmed that absolute values of unphysical negative eigenvalues of $\hat{\rho}_{\mathrm{RBM}}$, if any, and $||\hat{\rho}_{\mathrm{RBM}} - \hat{\rho}^{\dagger}_{\mathrm{RBM}}||/||\hat{\rho}_{\mathrm{RBM}} + \hat{\rho}^{\dagger}_{\mathrm{RBM}}||$ are in the order of 10^{-3}. Such sufficiently small magnitudes of the both quantities compared to unity indicate the success of optimization in the NSS algorithm [*3]. The physical observables of the stationary states, such as the entropy, are computed using the symmetrized density matrix,

$$\hat{\rho}'_{\mathrm{RBM}} = \frac{\hat{\rho}_{\mathrm{RBM}} + \hat{\rho}^{\dagger}_{\mathrm{RBM}}}{2}, \tag{5.26}$$

which assures the physical observables to be real values.

While the parameters are unrestricted during the optimization, it is instructive to provide the explicit expression of the ansatz assured to represent physical density matrix [214]. [See Fig. 5.4 for the graphical illustration.] Concretely, the

[*3] The two quantities can be further reduced by, for instance, taking larger α.

ansatz is given as

$$\begin{aligned}\langle\langle \sigma, \tau|\rho_{\mathrm{RBM}}\rangle\rangle = \frac{1}{Z} \sum_{\{h_j, h_k^{(1)}, h_k^{(2)}\}} & \exp\left(\sum_{i,j}(W_{ij}\sigma_i + W_{ij}^*\tau_i)h_j\right) \\ & \times \exp\left(\sum_{i,k} W_{ik}\sigma_i h_k^{(1)} + b_k h_k^{(1)}\right) \exp\left(\sum_{i,k} W_{ik}^*\tau_i h_k^{(2)} + b_k^* h_k^{(2)}\right) \\ & \times \exp\left(\sum_i a_i\sigma_i + a_i^*\tau_i\right), \end{aligned} \tag{5.27}$$

where h_j is the j-th hidden spin that interacts with both the physical and fictitious spins, $h_k^{(1,2)}$ is the k-th hidden spin that interact with only the visible (fictitious) spins. We introduce the number ratio of spins as $\alpha = M/N$ and $\alpha' = M'/N$ where $M^{(')}$ is the number of hidden spins that is connected to both (either of) physical and fictitious spins, and the total as $\alpha_{\mathrm{tot}} = \alpha + 2\alpha'$. Note the interactions and the magnetic fields on hidden spins are related with complex conjugate operations.

The ansatz given as Eq. (5.27) is as highly expressive as the one for the pure states in terms of the entanglement. In Ref. [62] it is shown that the maximally entangled pure states [*4] can be expressed using only $O(L)$ hidden spins, where L is the total number of spins in the system. Similarly, the cRBM ansatz efficiently expresses density matrices with large operator space entanglement, namely the entanglement entropy of the density matrix in the vector representation [202, 203]. Here, the concrete definition of the operator space entanglement entropy is given as follows. Let us take a mixed state in the vector representation as $|\rho\rangle\rangle$, which is a pure state on the doubled Hilbert space spanned by L physical and L fictitious spins. After choosing $[L/2]$ physical spins and its corresponding $[L/2]$ fictitious spins to form a subsystem $\mathcal{S}$, we compute the entanglement entropy of $\mathrm{Tr}_{\bar{\mathcal{S}}}[|\rho\rangle\rangle\langle\langle\rho|]$, where $\bar{\mathcal{S}}$ is the complement of $\mathcal{S}$. Here, $[x]$ is the largest integer that does not exceed x.

To demonstrate our argument, we show that the cRBM ansatz given by Eq. (5.27) with random parameters exhibits volume-law scaling of the operator space entanglement entropy. Shown in Fig. 5.5 is the system size dependence of the operator space entanglement entropy in random-valued cRBM ansatz characterized by different number of hidden spins. Both the real and imaginary parts of the

[*4] The entanglement entropy for the pure states is defined for a composite system $\mathcal{H} = \mathcal{H}_A \otimes \mathcal{H}_B$ as the von Neumann entropy of the reduced density matrix obtained by tracing out the subspace $\mathcal{H}_A$.

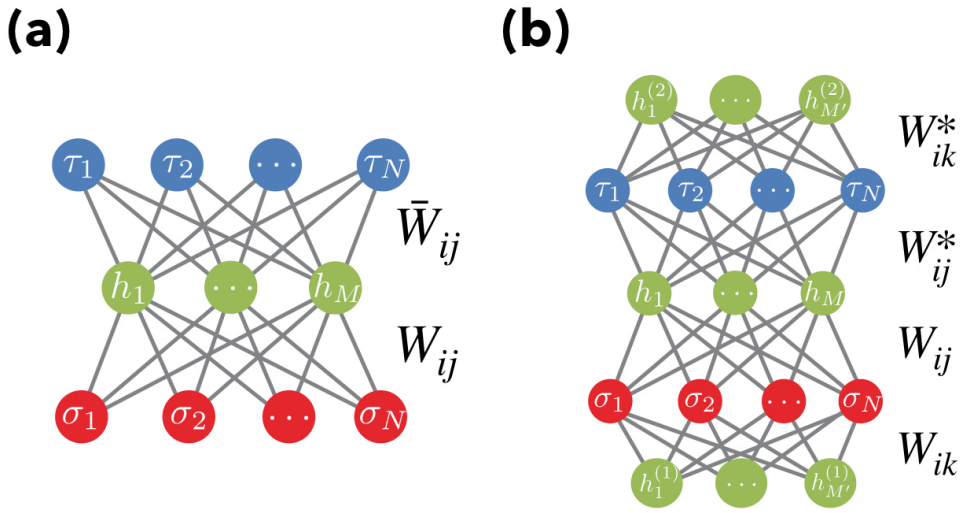

Figure 5.4: Graphical illustration of the cRBM ansatz for the stationary state in the vector representation. Network structures denote (a) the ansatz employed in the NSS algorithm and (b) a state assured to satisfy the requirements for physical density matrices. As is discussed in the main text, network parameters are subject to some restriction. While the interactions W_{ij} and $\bar{W}_{ij}$, for instance, are independent in (a), they are related via complex conjugate operation as $\bar{W}_{ij} = W^*_{ij}$ in (b).

parameters are drawn randomly from a section $[-r, r]$ where r may differ for W_{ij}, W_{ik}, a_i, b_k.

The increase of quantum entanglement in the operator space along the number of spins demonstrates the volume-law scaling. We thus find that the large operator space entanglement entropy is not necessarily an obstacle for reliable simulations for our NSS algorithm, in contrast with methods based on the tensor network ansatz such as the MPO algorithm. As a caveat, we note that not all volume-law states can be expressed efficiently by the cRBM ansatz, which is discussed in Appendix F.

(c) Choose Optimization Strategy

In the following, we introduce the stochastic reconfiguration (SR) method [215] which updates the variational parameters θ in the cRBM ansatz by minimization of the cost function defined in §5.3.2. In short, the SR method is designed to perform the imaginary time evolution in a stochastic manner. The imaginary time

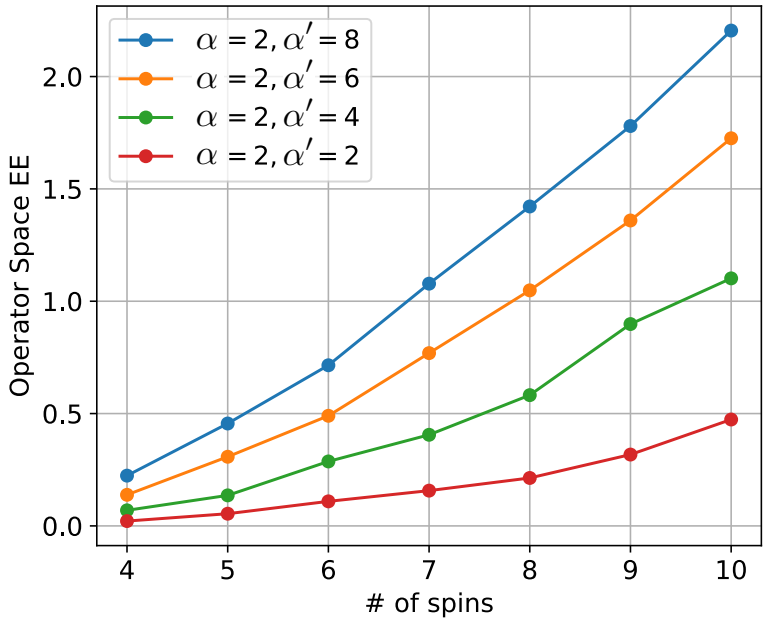

Figure 5.5: The volume-law scaling of the operator space entanglement entropy in the random-valued cRBM ansatz given by Eq. (5.27). Here, the number ratios of the hidden spins are taken as $(\alpha, \alpha') = (2,8), (2,6), (2,4), (2,2)$. We do not observe any evident difference between finite α, and hence we fix as $\alpha = 2$. The amplitudes of the random parameters are taken as $r = 0.05, 0.003, 0.1, 0.1$ for W_{ij}, W_{ik}, a_i, b_k, respectively. Note that each point shows the averaged value over 10 random states that are independently generated.

evolution technique relies on the fact that the lowest eigenstate $|\psi\rangle_{\mathrm{GS}}$ of a given Hermitian operator $\hat{H}$ can be obtained as follows,

$$\begin{aligned} |\Psi\rangle_{\mathrm{GS}} &= \lim_{\beta\to\infty}\lim_{N\to\infty}\left(e^{-\frac{\beta}{N}\hat{H}}\right)^N |\Psi\rangle_0 \\ &\sim \lim_{N\to\infty}\left(1-\epsilon\hat{H}\right)^N |\Psi\rangle_0 , \end{aligned} \tag{5.28}$$

where the initial state $|\Psi\rangle_0$ is taken to be non-orthogonal to the lowest eigenstate and $\epsilon \in \mathbb{R}$ is a sufficiently small positive value so that the linear approximation from the first to the second line holds. Instead of considering the full Hilbert space, the SR method simulates the evolution of the variational parameters. Let $|\Psi_\theta\rangle$ and $|\Psi'_\theta\rangle$ be a variational state before and after imaginary-time evolution for

infinitesimally small step. We consider expansion as

$$\begin{aligned} |\Psi_{\theta'}\rangle &= |\Psi\rangle_\theta + \sum_p \delta\theta_p \frac{\partial}{\partial\theta_p} |\Psi\rangle_\theta + O\left((\delta\theta_p)^2\right) \\ &\sim |\Psi\rangle_\theta + \sum_p \delta\theta_p \hat{\Delta}_p |\Psi_\theta\rangle , \\ \hat{\Delta}_p &= \mathrm{diag}\left(\{(\partial/\partial\theta_p)\log\langle\sigma|\Psi_\theta\rangle\}_{\sigma\in\mathcal{S}}\right) \end{aligned} \tag{5.29}$$

where $\hat{\Delta}_p$ is a diagonal operator with each element given as logarithmic derivative of the wave function with respect to parameter p. Note that $\mathcal{S}$ is the set of all possible spin configuration basis. The update of parameters $\{\delta\theta_p\}$ are determined by requiring that the Fubini-Study metric between the state given by the imaginary-time evolution as Eq. (5.28) and the one by (5.29) to be minimized, i.e.,

$$\delta\widetilde{\theta} = \arg\min_{\delta\theta} \left(\mathcal{F}\left((1-\epsilon\hat{H})|\Psi_\theta\rangle , (1+\sum_p \delta\theta_p\hat{\Delta}_p)|\Psi_\theta\rangle \right) \right), \tag{5.30}$$

$$\mathcal{F}(|\phi_1\rangle , |\phi_2\rangle) := \arccos\sqrt{\frac{\langle\phi_1|\phi_2\rangle}{\langle\phi_1|\phi_1\rangle}\frac{\langle\phi_2|\phi_1\rangle}{\langle\phi_2|\phi_2\rangle}}, \tag{5.31}$$

where $\delta\widetilde{\theta}$ is the update of variational parameters that best approximates the imaginary time evolution. The explicit expressions of the updates in the variational parameters are given as follows,

$$\begin{aligned} \delta\widetilde{\theta}_p &= -\epsilon\sum_{p'} (S)^{-1}_{pp'} f_{p'}, \\ f_p &:= \langle\hat{\Delta}_p^\dagger \hat{E}_{\mathrm{loc}}\rangle - \langle\hat{\Delta}_p^\dagger\rangle\langle\hat{E}_{\mathrm{loc}}\rangle , \\ S_{pp'} &:= \langle\hat{\Delta}_p^\dagger\hat{\Delta}_{p'}\rangle - \langle\hat{\Delta}_p^\dagger\rangle\langle\hat{\Delta}_{p'}\rangle , \end{aligned} \tag{5.32}$$

where f_p, or the **force**, invokes the "motion" of the parameters and $S_{pp'}$, the quantum Fisher information, is known to play the role of the quantum geometric tensor which yields the steepest gradient direction in terms of the information geometry [61, 216, 217].

The evaluation of the force and geometric tensor is performed by Monte Carlo sampling in the vector representation over the probability distribution

$$p(\sigma,\tau) = \frac{|\langle\langle\sigma,\tau|\rho_{\mathrm{RBM}}\rangle\rangle|^2}{\langle\langle\rho_{\mathrm{RBM}}|\rho_{\mathrm{RBM}}\rangle\rangle}. \tag{5.33}$$

A step of parameter update by Eq. (5.32) is referred to as an epoch in the following. The number of the sampled spin configurations at k-th epoch of optimization

is denoted as $M^{(k)}$, which is taken to be a constant M in our optimization. The update is repeated for N_{it} epochs until the cost function reaches the order of 10^{-3} or less.

As was introduced in previous sections, the Hermitian operator is taken as the product $\hat{\mathcal{L}}^\dagger\hat{\mathcal{L}}$, and the variational parameters are the interactions and magetization fields in the cRBM ansatz. We present the pseudo code of the SR method in Algorithm 1.

Algorithm 1 Stochastic Reconfiguration in the NSS algorithm

Set Liouvillian operator $\hat{\mathcal{L}}$.
Set initial parameters $\theta^{(k=0)}$.
Set learning rate schedule $\{\epsilon^{(k)}\}$ and sampling numbers $\{M^{(k)}\}$.
Initialize epoch number $k = 0$.
while termination condition not satisfied **do**

1. Define the local energy $\hat{E}^{\text{loc}}$ and logarithmic derivative of ansatz $\hat{\Delta}_p$ as

$$\begin{aligned}\left(\hat{E}^{\text{loc}}\right)_{\sigma\tau} &= \sum_{\sigma'\tau'} \frac{\langle\langle\sigma'\tau'|\rho_\theta^{(k)}\rangle\rangle}{\langle\langle\sigma\tau|\rho_\theta^{(k)}\rangle\rangle}\langle\langle\sigma'\tau'|\hat{\mathcal{L}}^\dagger\hat{\mathcal{L}}|\sigma\tau\rangle\rangle \\ \left(\hat{\Delta}_p\right)_{\sigma\tau} &= \partial_{\theta_p}\left(\log\langle\langle\sigma\tau|\rho_\theta^{(k)}\rangle\rangle\right)\end{aligned}$$

2. Compute the force $f^{(k)}$ and metric $S^{(k)}$as

$$\begin{aligned}f_p^{(k)} &= \langle\langle\hat{\Delta}_p^\dagger\hat{E}^{\text{loc}}\rangle\rangle - \langle\langle\hat{\Delta}_p^\dagger\rangle\rangle\langle\langle\hat{E}^{\text{loc}}\rangle\rangle, \\ S_{pp'}^{(k)} &= \langle\langle\hat{\Delta}_p^\dagger\hat{\Delta}_{p'}\rangle\rangle - \langle\langle\hat{\Delta}_p^\dagger\rangle\rangle\langle\langle\hat{\Delta}_{p'}\rangle\rangle,\end{aligned}$$

3. Update $\theta^{(k)} \leftarrow \theta^{(k)} - \epsilon^{(k)}\sum_{p'}\left(S^{(k)}\right)^{-1}_{pp'} f_{p'}^{(k)}$
4. $k \leftarrow k+1$

end while

(d) Run optimization

Since the cost function, ansatz, and the optimization strategy have been defined, one may finally run the algorithm to obtain the stationary state of a given system. Figure 5.6 shows the iteration of the cost function for one-dimensional transverse-field Ising model with damping, which is introduced and also further discussed in §5.4.1. We observe that the cost function converges after 1000 epochs

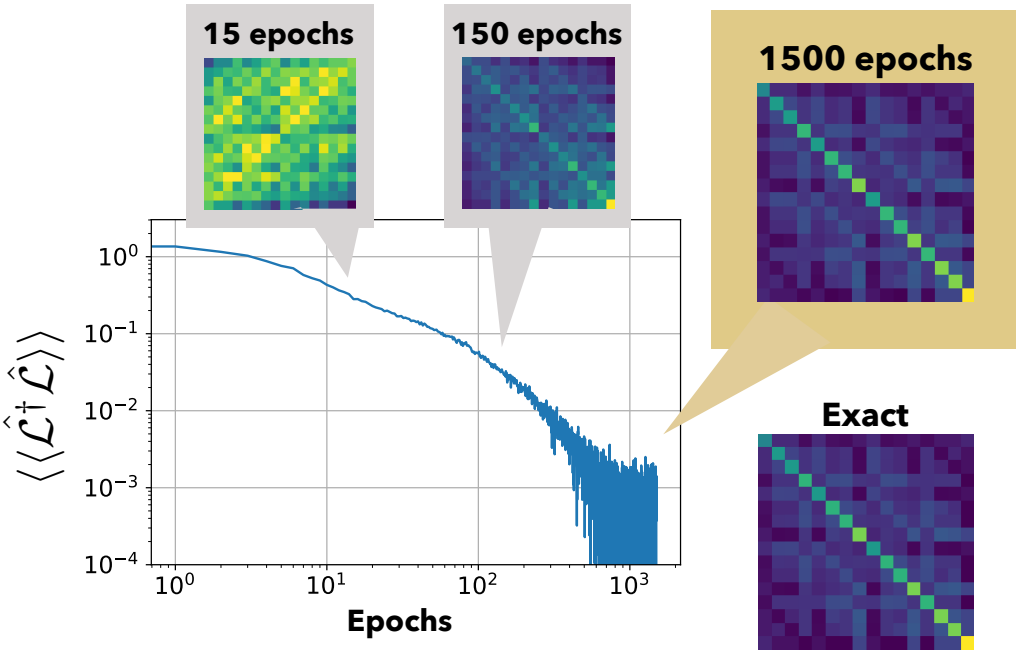

Figure 5.6: Iteration of the cost function $\langle\langle \hat{\mathcal{L}}^\dagger \hat{\mathcal{L}} \rangle\rangle$ for the one-dimensional transverse-field Ising model with damping under the periodic boundary condition, which is introduced in §5.4. Shown in the insets are the real part of the density matrix obtained from the cRBM ansatz after 15, 150, and 1500 epochs, respectively. After the convergence of the optimization, the cRBM ansatz nicely reproduces the result from exact diagonalization. The parameters are taken as $V = 0.3, g = 1, \gamma = 0.5$, and the system size is taken as $L = 4$. We generate $M = 2000$ spin configurations at each epoch.

or so. The fluctuation of the cost function, $\langle\langle \hat{\mathcal{L}}^\dagger \hat{\mathcal{L}} \rangle\rangle$, after the convergence is in the order of 10^{-3}, which is related with the residual error between the exact solution. One may either increase the number of sampling, M, to suppress the variance in the evaluation of the cost function or increase the number of parameters in the ansatz to reach higher accuracy.

5.4 Result

In this section, we demonstrate the NSS algorithm by applying it to three models that are in principle experimentally realizable using, e.g., cold atoms or trapped ions [218], namely the transverse-field Ising models in 1d and 2d as well as the XYZ model in 1d. Let us remind that the Liouvillian in the vector repre-

sentation can be given as follows,

$$\begin{aligned} \hat{\mathcal{L}} \left|\rho(t)\right\rangle\rangle &= \left(-i(\hat{H} \otimes \mathbb{1} - \mathbb{1} \otimes \hat{H}^T) + \sum_k \gamma_k \hat{\mathcal{D}}[\hat{c}_k] \right) \left|\rho(t)\right\rangle\rangle, \\ \hat{\mathcal{D}}[\hat{c}_k] &= \hat{c}_k \otimes \hat{c}_k^* - \frac{1}{2}\hat{c}_k^\dagger \hat{c}_k \otimes \mathbb{1} - \mathbb{1} \otimes \frac{1}{2}\hat{c}_k^T \hat{c}_k^*, \end{aligned} \tag{5.34}$$

where $\hat{H}$ is the Hamiltonian of the system, $\hat{c}_k$ is the k-th jump operator with its amplitude given by $\gamma_k > 0$, and $\hat{\mathcal{D}}$ is the dissipator describing the non-unitary dynamics.

5.4.1 Transverse-field Ising model in one dimension

To discuss the validity of our NSS ansatz for the concrete open quantum many-body systems, we first consider the stationary state of 1d transverse-field Ising model with the length L under the periodic boundary condition. Here, the Hamiltonian and the jump operators are given as

$$\hat{H} = \frac{V}{4} \sum_{i=0}^{L-1} \hat{\sigma}_i^z \hat{\sigma}_{i+1}^z + \frac{g}{2} \sum_{i=0}^{L-1} \hat{\sigma}_i^x, \tag{5.35}$$

$$\hat{c}_i = \hat{\sigma}_i^-, \quad \gamma_i = \gamma, \tag{5.36}$$

where $\hat{\sigma}_i^a$ $(a = x, y, z)$ is the Pauli matrix that acts on the i-th site, V is the strength of the nearest-neighbor interaction, g is the amplitude of the transverse magnetic field along the x-axis, and γ gives the magnitude of the homogeneous damping. To take advantage of the periodic boundary condition, i.e., $\hat{\sigma}_L = \hat{\sigma}_0$, we impose translation symmetry on the cRBM ansatz.

As was introduced in Sec. 5.3, we minimize the expectation value $\langle\langle \hat{\mathcal{L}}^\dagger \hat{\mathcal{L}} \rangle\rangle$ using the SR method. Figure. 5.7 shows the comparison of stationary-state density matrices obtained by the Lanczos method, which utilizes the Krylov subspace to efficiently approximate a subset of eigenvectors and eigenvalues of a given sparse matrix [219], and the NSS algorithm with the number ratio of the spins taken as $\alpha = 1$. Here, the model parameters are given as $V = 0.3, g = 1$, and $\gamma = 0.5$, which results in a stationary state with the volume-law entropy. Figure 5.7(a) and (b) visually illustrates that the approximation of the state with the NSS algorithm well represents the stationary state calculated by the Lanczos method.

We argue that the accuracy of the stationary state is also confirmed quantitatively via the calculation of the fidelity. The fidelity between $\hat{\rho}_1$ and $\hat{\rho}_2$, which

is exclusively considered as the stationary-state density matrices obtained by the NSS algorithm and Lanczos method in practice, is defined as [220]

$$F(\hat{\rho}_1, \hat{\rho}_2) = \left(\mathrm{Tr} \sqrt{\sqrt{\hat{\rho}_1} \hat{\rho}_2 \sqrt{\hat{\rho}_1}} \right)^2 . \tag{5.37}$$

This corresponds to the largest fidelity between any two purifications[*5] of the density matrices or the minimum overlap between probability distributions defined by positive-valued operator measurement [*6]. For the current case, we find the fidelity to satisfy $F > 0.999$. We also observe in Fig. 5.7(c) that the expectation value $\langle\langle \hat{\mathcal{L}}^\dagger \hat{\mathcal{L}} \rangle\rangle$, which gives measure of the approximation [*7], is neatly optimized and reaches the order of 10^{-3}. Accordingly, we find that the physical quantities are in good agreement with the exact results. For example, the entropy contribution by each eigenvalue of the density matrix, i.e., $-p_n \ln p_n$ for the n-th eigenvalue p_n, is remarkably accurate (see Fig. 5.7(d)), such that the relative error of the total entropy is the order of 10^{-3}.

As is the case with other VMC calculations, it must be noted that both numerical cost and required memory for the NSS algorithm are much suppressed compared to methods that deal with the whole Hilbert space. In particular, the wall times for the NSS algorithm and the Lanczos method are compared in Appendix G.

[*5] A purification of a mixed state refers to a pure state in the higher dimensions that is related in the following way. Let $\hat{\rho}$ be a mixed state in the system $\mathcal{H}_S$. When a pure state $|\Psi\rangle \in \mathcal{H}_S \otimes \mathcal{H}_A$, where $\mathcal{H}_A$ is an auxiliary space, satisfies $\hat{\rho} = \mathrm{Tr}_{\mathcal{H}_A}[|\Psi\rangle \langle\Psi|]$, the pure state $|\Psi\rangle$ is a purification of the mixed state $\hat{\rho}$. Obviously, a purification of a given state is not unique.

[*6] Let $\{\hat{E}_i\}$ be a set of positive operator valued measurement (POVM), and $p_i^{(k)} = \mathrm{Tr}[\hat{\rho}_k \hat{E}_i]$ the probability distribution given by the POVMs. The fidelity can be found to satisfy

$$\arg\min_{\{\hat{E}_i\}} \sum_i \sqrt{p_i^{(1)} p_i^{(2)}} = F(\hat{\rho}_1, \hat{\rho}_2), \tag{5.38}$$

where the left-hand-side considers the minimum over overlap of probability distributions [221].

[*7] We can show that $|\langle\langle \rho_{\mathrm{SS}} | \rho_{\mathrm{RBM}} \rangle\rangle|^2 \geq 1 - \frac{\langle\langle \hat{\mathcal{L}}^\dagger \hat{\mathcal{L}} \rangle\rangle}{\Delta}$, where Δ is the spectral gap of $\hat{\mathcal{L}}^\dagger \hat{\mathcal{L}}$.

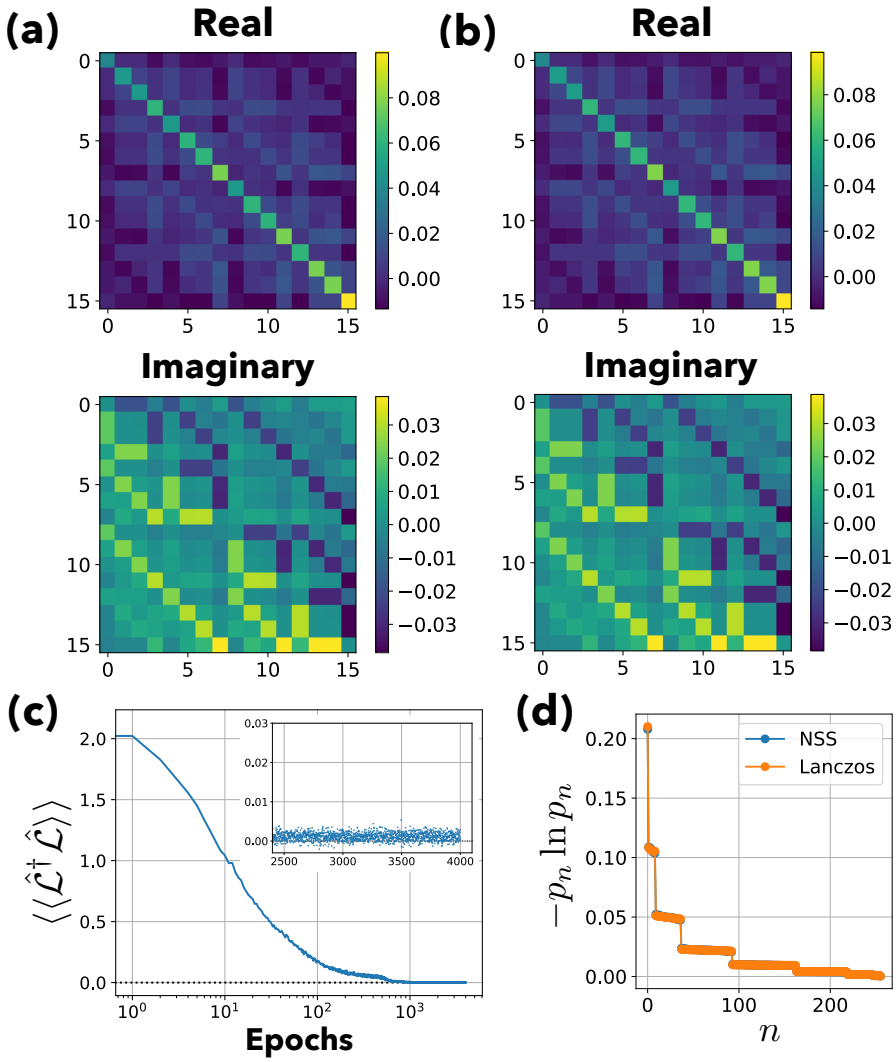

Figure 5.7: (a) The real and imaginary parts of the stationary-state density matrix of the 1d transverse-field Ising model with dissipations in Eq. (5.35) obtained by the Lanczos method. (b) The real and imaginary parts of the stationary-state density matrix obtained by the NSS algorithm. The fidelity F between the stationary states obtained by the Lanczos and the NSS algorithms is over 0.999. (c) Iteration of the cost function $\langle\langle \hat{\mathcal{L}}^\dagger \hat{\mathcal{L}} \rangle\rangle$. The optimization works well and $\langle\langle \hat{\mathcal{L}}^\dagger \hat{\mathcal{L}} \rangle\rangle$ reaches the order of 10^{-3}. The inset shows the convergence at the last 1500 epochs. (d) The entropy contribution $-p_n \ln p_n$, where p_n is the n-th eigenvalue of the density matrix from the top. The blue and orange dots denote the results for the NSS algorithm and Lanczos method, respectively. The relative error for the total entropy is order of 10^{-3}. For all panels, we use $V = 0.3, g = 1$, and $\gamma = 0.5$, and the number ratio of the spins is $\alpha = 1$. In panels (a) and (b), the system size is $L = 4$ and the sampling number per iteration is $M = 2000$, repeated for $N_e = 1500$ epochs, while we take $L = 8$, $M = 2000$, $N_e = 4000$ for (c) and (d).

5.4.2 Transverse-field Ising model in two dimensions

We next demonstrate the NSS algorithm for the 2D transverse-field Ising model on the square lattice with system size L_x and L_y along the x- and y-axes, respectively. We again take the periodic boundary condition. The Hamiltonian and the jump operators are given as [201]

$$\hat{H} = \frac{V}{4}\sum_{\langle i,i'\rangle}\hat{\sigma}_i^z\hat{\sigma}_{i'}^z + \frac{g}{2}\sum_i \hat{\sigma}_i^x, \tag{5.39}$$

$$\hat{c}_i = \hat{\sigma}_i^-, \quad \gamma_i = \gamma, \tag{5.40}$$

where the summation in the first term of $\hat{H}$ is taken over the edges connecting the neighboring sites, which are denoted as i and i'.

The iteration of the cost function in Figure 5.8(a) shows that the optimization works well even for the 2D case. Indeed, as shown in Fig. 5.8(b), the entropy contribution for each eigenvalue of the stationary state is well reproduced with high accuracy. This result strengthens the expectation that the cRBM ansatz does not suffer from high spatial dimensionality.

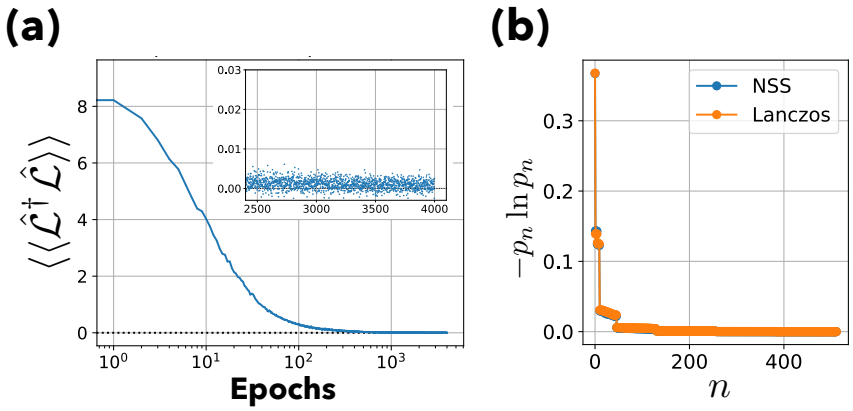

Figure 5.8: (a) Iteration of the cost function $\langle\langle\mathcal{L}^\dagger\mathcal{L}\rangle\rangle$ for the 2d transverse-field Ising model defined as Eq. (5.39). The inset shows the convergence at the last 1500 epochs. (b) The entropy contribution $-p_n \ln p_n$ by the n-th eigenvalue of the density matrix. The blue and orange dots denote the results for the NSS algorithm and Lanczos method, respectively. The relative error of the total entropy is order of 10^{-5}. We use the parameters $L_x = L_y = 3, V = 0.3, g = 1$, and $\gamma = 1$. The number ratio of the spins is $\alpha = 4$, and the resulting fidelity is $F = 0.9996$. The sampling number per iteration is $M = 4000$, repeated for $N_e = 4000$ epochs.

5.4.3 XYZ model in one dimension

Finally, we investigate the 1d XYZ model, in which the dissipations are known to invoke dramatic change of the phase diagram compared with its counterpart in the closed system [200]. The model is defined as

$$\hat{H} = \sum_{i=0}^{L-1} J_x \hat{\sigma}_i^x \hat{\sigma}_{i+1}^x + J_y \hat{\sigma}_i^y \hat{\sigma}_{i+1}^y + J_z \hat{\sigma}_i^z \hat{\sigma}_{i+1}^z \tag{5.41}$$

$$\hat{c}_i = \hat{\sigma}_i^-, \quad \gamma_i = \gamma, \tag{5.42}$$

where J_a is the interaction for a $(a = x, y, z)$ component of the spin. We particularly consider $J_x = 0.9, J_y = 0.4, J_z = 1$, and $\gamma = 1$ under the periodic boundary condition. Here, finite systems show "remnants" of the phase transition which is inappropriately suggested by the mean-field approximation [199].

Shown in Fig. 5.9 is the comparison of the NSS algorithm and the Lanczos method regarding the entropy contribution from each eigenvalue of the stationary state. Even though our choice of parameters leads to the non-simple stationary state of our small systems (as indicated from the peak of the structure factor [200]), the optimized cRBM ansatz describes the exact results well.

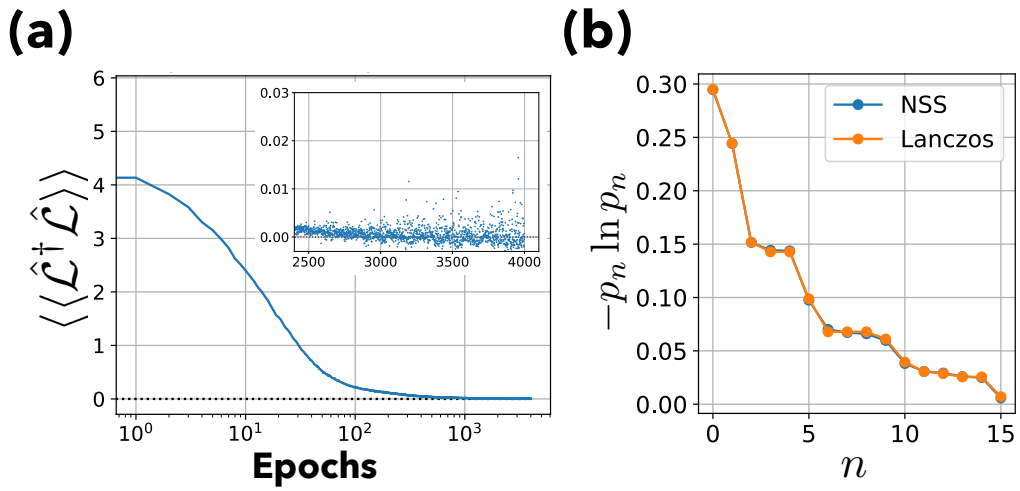

Figure 5.9: (a) Iteration of the cost function $\langle\langle \mathcal{L}^\dagger \mathcal{L} \rangle\rangle$ for the 1d Ising model defined as Eq. (5.41). The inset shows the convergence at the last 1500 epochs. (b) The entropy contribution $-p_n \ln p_n$ for the n-th eigenvalue of the stationary-state density matrix. The data for the NSS (blue) and the exact diagonalization (orange) agree well with each other. The fidelity of the NSS is over 0.998 and the relative error of the total entropy is order of 10^{-2}. In both panels, the parameters of the model are taken as $J_x = 0.9, J_y = 0.4, J_z = 1.0, L = 4$, and $\gamma = 1$. The number ratio of the spins is taken as $\alpha = 16$ and the sampling number per iteration is $M = 16000$, repeated for $N_e = 4000$ epochs.

5.5 Summary of this Chapter

We have developed a new algorithm that optimizes the neural quantum states which are suited for expressing the stationary states of open quantum many-body systems. The complex-valued restricted Boltzmann machine is applied as the variational ansatz to solve the zero-energy ground state search problem on an Hermitian operator which is obtained by mapping the original stationary-state search problem of the Gorini-Kossakowski-Sudarshan-Lindblad equation.

As is expected from the pure-state case, the cRBM can even express density matrices with volume-law operator space entanglement, namely the entanglement entropy in the vector representation. We have then demonstrated that the cRBM ansatz is capable of expressing the stationary states of the dissipative one- and two-dimensional transverse-field Ising models and one-dimensional XYZ model. In particular, we have shown that the one-dimensional transverse-field Ising model is simulated better with our NSS algrithm than the Lanczos method in terms of the system-size scaling of the computational time.

While the aim of our work is to show the first demonstration of the adequacy of the NSS algorithm for open quantum many-body systems including highly entangled states and two-dimensional states, we leave several intriguing questions as future works. One naive question is the capability of our method to simulate larger system sizes, in which other methods suffer from expensive numerical cost. Another important question is to clarify the versatility of open quantum many-body systems describable by our method. We expect that our ansatz performs well regardless of the dimensionality. This is suggested from the bipartite-graph structure of the RBM, which is free from the geometry of the underlying physical lattice. Given the significance in many-body quantum physics even in the isolated systems and the difficulty in the previously-developed methods, one of the most important future tasks would be to apply the method to dissipative two-dimensional systems such as the Bose/Fermion-Hubbard model. It is surely an important question how the model behaves under the dissipation, which often cause drastic change in the property of the system. It is also interesting whether our method works for various long-range interacting systems (such as the Haldane-Shastry model [71]) with dissipations, whose mixed stationary states can be highly entangled.

Two comments regarding the extension of our work are in order. Firstly, the application to obtain relaxation time is worth investigating. While in the current

work we have adopted the product of the Liouvillian operator and its hermitian conjugate as the ”generator” of imaginary time evolution, the scheme can be extended to deal with real-time evolution by considering another variational principle, which contains information on the decay of non-stationary states. Secondly, it would be interesting to consider some ”inverse problem” in which either the Hamiltonian or dissipation is tunable to maximize some physical observable or fidelity with desirable states.

Note that after the completion of our work published as Ref. [222], we became aware of some related works. Refs. [223] discussed the time evolution and stationary states of open quantum many-body systems by using the cRBM and Ref. [224, 225] studied the approximation of the stationary states by the cRBM ansatz.

6
Summary of Thesis

In this Chapter, the results obtained in this thesis are summarized and future perspectives are given.

In Chapter 3, we have developed a new scheme to classify the quantum phases of free-fermion systems with disorder. Given the disorder that keeps the discrete symmetries of the ensemble as a whole, we argue that translational symmetry, which is broken in the individual quasiparticle distribution, is recovered statistically by taking the ensemble average. This enables one to classify the quantum phases in the disordered regime using a neural network trained in the clean limit. In particular, the neural network has been shown to be capable of classifying the phases of 2d noncentrosymmetric superconductor in class DIII with disorder in the following two cases. One is the extension of the phase diagram from the clean limit ($w = 0$) to the disordered region ($w > 0$) when all possible phases are present in the clean limit. The machine successfully learns the property of each phase from the average quasiparticle distribution $\langle P(\mathbf{r}) \rangle$ with *quasi*-translational symmetry. The high values of confidence of the machine within the phases reflects the success of the feature extraction and statistical recovery of translational symmetry. Another is the detection of the unlearned phase. A correctly optimized MLP exhibits high confidence when the learned feature is present in the data, and vice versa. When the new phase does not exhibit localization in either bulk or the edge, and the machine gets confused. The consistency with other independent methods has been confirmed. We emphasize that since the current method relies on the appearance of edge states assured by the bulk-edge correspondence and the statistical recovery of the translational symmetry, it is applicable to models with arbitrary lattice geometry, dimension, and symmetry class. Application to even wider class of models including topological crystalline insulators/superconductors is worth investigating. Also, we naturally expect from the ubiquitous appearance of the bulk-edge correspondence that the proposed scheme is applicable even under the presence of interaction or in bosonic systems.

In Chapter 4, we have found an exact representation of the generalized Ising models by the Boltzmann machine. We have shown that the appropriate combination of the algebraic transformations, namely the star-triangle and decoration-iteration transformations, lead to expression of the many-spin interaction in terms of fewer-spin interactions at the expense of the degrees of freedom. Furthermore, such a representation is found to be beneficial from the perspective of Monte Carlo simulations since the celebrated cluster update algorithm becomes applicable. This point has been demonstrated in a model with two- and three-spin interactions on the Kagomé lattice that the application of the cluster update algorithm by Swendsen and Wang drastically reduces the critical slowing down in terms of the autocorrelation between the samples. We note that, in some specific many-spin interacting models, it is possible to introduce cluster-update algorithm with fewer auxiliary degrees of freedom by modifying the Fortuin-Kasteleyn transformation [15], which implicitly assumes application to models with finite-temperature phase transition in universality class such as the square Ising model or Potts model. In sharp contrast, the transformation technique introduced in our work allows us to apply arbitrary global update algorithm, and hence provide a general and systematic framework for models with arbitrary interaction in various lattice geometry. It is noteworthy that our scheme is also capable of handling many-spin interacting classical spin systems with continuous degrees of freedom. This can be done by considering projection of each variable on some axis. Namely, the continuous variables are decomposed into components that are parallel and orthogonal to some random axes, and new Ising variables are defined from the parallel component. By regarding the model obtained by the projection as the generalized Ising model, we can apply our method, which is beyond our scope in the current thesis.

In Chapter 5, we have developed a new numerical algorithm that optimizes the complex-valued restricted Boltzmann machine (cRBM), which can express mixed states with volume-law operator space entanglement, to the approximate representation of stationary states in open quantum many-body systems. The variational Monte Carlo technique is used to solve the zero-energy ground state search problem on an Hermitian operator which is obtained by mapping the original stationary-state search problem of the Gorini-Kossakowski-Sudarshan-Lindblad equation. We have demonstrated that the cRBM ansatz is capable of expressing the stationary states of the dissipative one- and two-dimensional transverse-field Ising models and one-dimensional XYZ model. While the aim of our work

is to provide the first demonstration the algorithm for open quantum many-body systems including highly entangled states and two-dimensional states, several intriguing questions are left as future works. One naive question is the capability of the algorithm to simulate larger system sizes, and another important question is the versatility of open quantum many-body systems describable by our method. We expect that our ansatz performs well regardless of the dimensionality due to the bipartite-graph structure, which is free from the geometry of the underlying physical lattice, of the RBM. Given the significance in many-body quantum physics even in the isolated systems and the difficulty in the previously-developed methods, one of the most important future tasks would be to apply the method to dissipative two-dimensional systems such as the Bose/Fermion-Hubbard model. It is surely an important question how the model behaves under the dissipation, which often cause drastic change in the property of the system. It is also interesting whether our method works for various long-range interacting systems with dissipations, whose mixed stationary states can be highly entangled as well.

A
Mini-batch Training Algorithms

In this Appendix, we discuss the mini-batch training algorithms. In particular, we discuss the stochastic gradient descent (SGD) algorithm and the AdaGrad algorithm [134], in which the learning rate for the gradient vector is changed adaptively.

As is described in Algorithm 2 below, the SGD algorithm simply employs the mini-batch evaluation of the gradient vector. Although the idea is rather simple, this strategy is advantageous compared to the gradient descent in the following points:

- *[Machine Learning.]* Computing the gradient vector based on the whole training dataset is tedious. Since the gradient vector for likelihood-based cost function is given as the mean over the dataset, we may approximate it from a subset, or mini-batch, of the dataset. The numerical cost for a single update is determined from the size of the mini-batch, and hence the SGD algorithm is considered to be a scalable approach for larger dataset.

- *[Variational Monte Carlo.]* The SGD algorithm is often applied in variational calculations in condensed matter problems where the dataset is sampled from the machine by Monte Carlo sampling, which can be accelerated by parallelization.

Among the hyperparameters to train the network, the scheduling of the learning rate $\{\epsilon^{(k)}\}$ has been recognized to be crucial and yet difficult. Rather than constructing a "hand-crafted" schedule through trial-and-error, it is more efficient and natural to develop an adaptive way of tuning the learning rate. In Algorithm 3, we show the algorithm of AdaGrad, which scales each element of the gradient vector inverse proportionally to the accumulated squared value of the element. Given the initial rate ϵ, the algorithm determines the learning rate at each step. Instead of accumulating the gradient for the whole iteration, we may also consider an exponentially weighted moving average. This is called the

RMSProp algorithm [226], and is also widely used in the machine learning community.

Other approaches to speed up the optimization of parameters of neural networks include the momentum method [227], the combination of adaptive learning rate scheduling with the momentum [228], the use of the second order derivative such as the Newton method. No universally optimal strategy has been known up to now, and one typically choose the optimization depending on their knowledge on the hyperparameter tuning.

Algorithm 2 Stochastic Gradient Descent Algorithm

Set initial parameter $\theta^{(k=0)}$, the learning rate schedule $\{\epsilon^{(k)}\}$ and mini-batch sizes $\{M^{(k)}\}$.
Set labeled dataset $\mathcal{D} = \{(\hat{\mathbf{x}}_i, \hat{\mathbf{y}}_i)\}$.
while termination condition not satisfied **do**
  Sample mini-batch of dataset $\mathcal{D}^{(k)} = \{(\hat{\mathbf{x}}_i, \hat{\mathbf{y}}_i)\}_{i=1}^{M^{(k)}}$.
  Evaluate gradients by mini-batch as $\partial_\theta C_\theta^{(k)}$
  Update $\theta^{(k)} \leftarrow \theta^{(k)} - \epsilon^{(k)} \partial_\theta C_\theta^{(k)}$
  $k \leftarrow k + 1$
end while

Algorithm 3 AdaGrad Algorithm

Set initial parameter $\theta^{(k=0)} = \{\theta_i^{(k=0)}\}_i$ and initial learning rate ϵ
Set minibatch numbers $\{M^{(k)}\}_k$
Set Gradient accumulation r=0 and small constant δ
while termination condition not satisfied **do**
  Get a random minibatch of training dataset $\mathcal{D}^{(k)} = \{\mathbf{x}_m, \mathbf{y}_m\}_{m=1}^{M^{(k)}}$
  for θ_i in $\theta^{(k)}$ **do**
    Evaluate gradients with respect to the cost function of minibatch as $g_i = \partial_{\theta_i} C_\theta^{(k)}$
    Accumulate the squared gradient amplitude $r_i \leftarrow r_i + g_i^2$
    Update $\theta_i^{(k)} \leftarrow \theta_i^{(k)} - \frac{\epsilon}{\delta + \sqrt{r_i}} \partial_{\theta_i} C_\theta^{(k)}$
  end for
  $k \leftarrow k + 1$
end while

B
Transfer Matrix Method

In this Appendix, we introduce the transfer matrix (TM) method for quasi-one-dimensional disordered system [116, 229, 230]. Metal-insulator transition such as the Anderson transition can be understood from the size dependence of the localization length λ and (thermal) conductivity g, which is easily computed by the TM method. Let us consider a quasi-one-dimensional system with the length L_x and the width S. We assume that the time-independent Schrödinger equation is given as follows,

$$L_{i-1}^{\dagger}\boldsymbol{\psi}_{i-1} + H_i\boldsymbol{\psi}_i + L_i\boldsymbol{\psi}_{i+1} = E\boldsymbol{\psi}_i. \tag{B.1}$$

Here, $H_i = H_i^{\dagger}$ is the Hamiltonian restricted on the i-th block and E is the eigenenergy. We may simply consider the slice of the rectangle as a block when only the nearest neighbor hopping is present, but otherwise not necessarily a geometrical intersection. $\boldsymbol{\psi}_i$ is the $2S$-dimensional wave function of the (quasi)particle on the i-th block and L_i is the hopping matrix from i-th to $(i+1)$-th block. Assuming $\det|L_i| \neq 0$, Eq. (B.1) is rewritten as

$$\begin{aligned}\begin{pmatrix} \boldsymbol{\psi}_{i+1} \\ \boldsymbol{\psi}_i \end{pmatrix} &= \begin{pmatrix} L_i^{-1}(E - H_i) & -L_i \\ I_{2S\times 2S} & 0 \end{pmatrix}\begin{pmatrix} \boldsymbol{\psi}_i \\ \boldsymbol{\psi}_{i-1} \end{pmatrix} \\ &:= \hat{T}_i(E)\begin{pmatrix} \boldsymbol{\psi}_i \\ \boldsymbol{\psi}_{i-1} \end{pmatrix},\end{aligned} \tag{B.2}$$

where the above defined $\hat{T}_i(E)$ is referred to as one-step TM. The wave function at the edge and the total TM, $\hat{T}(E)$, is obtained as follows,

$$\begin{pmatrix} \boldsymbol{\psi}_{L_x} \\ \boldsymbol{\psi}_{L_x-1} \end{pmatrix} = \left(\prod_{i=0}^{L_x-1}\hat{T}_i\right)\begin{pmatrix} \boldsymbol{\psi}_1 \\ \boldsymbol{\psi}_0 \end{pmatrix} := \hat{T}(E)\begin{pmatrix} \boldsymbol{\psi}_1 \\ \boldsymbol{\psi}_0 \end{pmatrix}. \tag{B.3}$$

In the limit of $L_x \to \infty$, we consider the positive definite operator, $\hat{\Gamma} = \lim_{S\to\infty}(\hat{T}\hat{T}^{\dagger})^{1/2S}$, to introduce

$$\lambda_j = \frac{1}{\ln \gamma_j}, \tag{B.4}$$

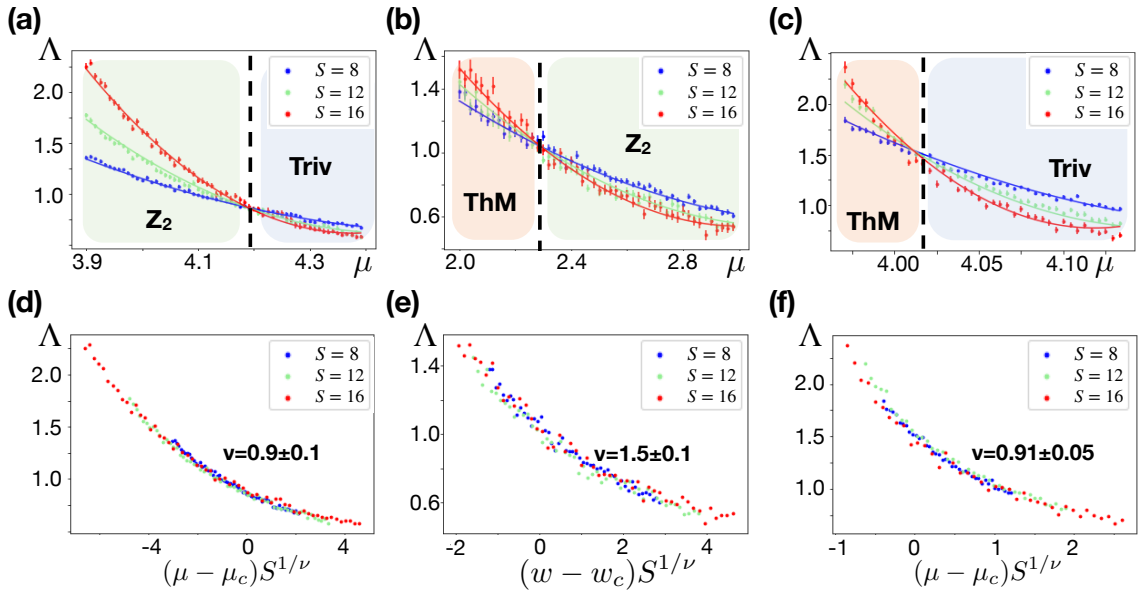

Figure B.1: Finite-size scaling of the dimensionless localization length, Λ, by the transfer matrix method for the Hamiltonian defined by Eq. (3.1) in the main text is shown in (a)-(c). The parameters are given as (a) $(w, \Delta, \Delta_2) = (5, 3, 0)$ under the OBC, (b) $(w, \Delta, \Delta_2) = (12.5, 3, 0)$ under the PBC, and (c) $(w, \Delta, \Delta_2) = (5, 3, 2)$ under the OBC. Presented in (d)-(f) are the corresponding data collapses. The system width varies as $S = 8, 12, 16$.

where γ_j is the j-th eigenvalue, which is positive and finite, of $\hat{\Gamma}$. The corresponding eigenfunction behaves as $\exp(\pm x/\lambda_j)$, with the sign denoting the direction of the decay, and therefore λ_j can be understood as the localization length. We set the length of the system from 10^4 to 10^5 so that the statistical error is small enough.

As pointed out by MacKinnon and Kramer, the finite-size scaling of the maximum localization length, $\lambda_{\max} := \lambda$, is equivalent to the scaling theory of conductance g [116, 129]. The dimensionless localization length in the vicinity of the metal-insulator transition point is assumed to be expressed by one-parameter scaling. Namely, by writing the parameter related to the transition as q (e.g. chemical potential μ and the amplitude of the Anderson potential w in our work),

$$\begin{aligned} \Lambda(q) := \frac{\lambda(q)}{S} &= \Lambda_c + \sum_{n=1}^{N} a_n (q - q_c)^n S^{n/\nu} \\ &+ \sum_{n=1}^{N'} b_n (q - q_c)^n S^{n/\nu + y}, \end{aligned} \tag{B.5}$$

where the subscripts c denote the value at the critical point, a_n and b_n are the expansion coefficients, and ν is the critical exponent for the localization length. The third term is the irrelevant length scale collection by the boundary, whose size dependence corrected by $y < 0$. Finite integers N and N' denote the number of the fitting parameters, which is taken as $N = 2, N' = 0$ in this work. Examples for $\mathbb{Z}_2$-trivial and $\mathbb{Z}_2$-thermal metal (ThM) phase transitions are shown in Fig. B.1, in which the rising (falling) of Λ for extended (localized) states are indeed observed.

Last but not least, let us note that appropriate boundary condition must be applied to detect the transition from or into the $\mathbb{Z}_2$ phase [230]. In two-dimensional systems, we have two options: open and periodic boundary condition (OBC or PBC) along the direction perpendicular to the transferred direction. The edge state appears along the transferred direction with the OBC, while the state is merely localized in the first or the last block with the OBC. Thus, to determine $\mathbb{Z}_2$-trivial ($\mathbb{Z}_2$-ThM) phase boundary, we must consider OBC (PBC) system. Note that the trivial-ThM boundary is detected in either way.

C
Noncommutative Geometry Approach for $\mathbb{Z}_2$ Topological Invariant

In this appendix, we introduce the noncommutative geometry approach to map out the phase diagram of 2d class DIII system. The $\mathbb{Z}_2$ index derived in previous works [101, 102] is numerically advantageous since it can be determined from the discrete spectrum of a certain compact operator without taking the disorder average. See Ref. [111] for detailed numerical implementation. The definition of the $\mathbb{Z}_2$ index of 2d class DIII system is given as

$$\nu = \text{ker dim } [\mathcal{A} - 1] \ \text{ modulo 2}, \tag{C.1}$$

where $\nu = 0$ and 1 correspond to the trivial and the $\mathbb{Z}_2$ phases, respectively. The operator $\mathcal{A}$ measures the difference between two projections,

$$\mathcal{A} = P_{\mathrm{F}} - \mathcal{D}_a^* P_{\mathrm{F}} \mathcal{D}_a. \tag{C.2}$$

Here, P_{F} is the projection operator onto the quasiparticle states below zero energy. The Dirac operator $\mathcal{D}_a$ is defined by

$$\mathcal{D}_a(\boldsymbol{r}) := \frac{r_1 + ir_2 - (a_1 + ia_2)}{|r_1 + ir_2 - (a_1 + ia_2)|}, \tag{C.3}$$

where $\boldsymbol{r} = (r_1, r_2) \in \mathbb{Z}^2$ denotes the position operator of a square lattice and $\boldsymbol{a} = (a_1, a_2) \in \mathbb{R}^2 \backslash \mathbb{Z}^2$ is a vector off the lattice points. The operator $\mathcal{D}_a^*$ is the adjoint of the Dirac operator $\mathcal{D}_a$. Hereafter, we regard λ_i as the i-th eigenvalue of the operator $\mathcal{A}$ in descending order including multiplicity.

Shown in Fig. C.1(a) is $\lambda_1 - \lambda_2$ as a function of the chemical potential μ and the disorder amplitude W with the pairings fixed as $\Delta = 3$ and $\Delta_2 = 0$. The orange-colored region denotes the $\mathbb{Z}_2$ phase since $\lambda_1 \sim 1$ [see, for instance, Fig. C.1(c)] and $\lambda_1 - \lambda_2 \neq 0$ evidently hold and thus imply $\nu = 1$. In Fig. C.1(a) we see that the numerical result is in good agreement with the boundary obtained by the TM. The two black areas above and to the right of the $\mathbb{Z}_2$ phase are identified

as the ThM and the trivial phases, respectively. This is done in the following way. When the spectral gap is open (= trivial or $\mathbb{Z}_2$ phase), the eigenvalues below unity always come in pairs [see Fig. C.1(b)(c)] owing to the two symmetries: the time-reversal symmetry of the Hamiltonian and the supersymmetric structure of the operator $\mathcal{A}$. However, the doublet structure is not guaranteed when the spectral or the mobility gap vanishes (the thermal metal (ThM) phase), and in fact, each eigenvalue shows no such a specific structure in the leftmost region of Fig. C.1(b).

The difference between the first and second eigenvalues for $\Delta_2 = 2$ is also given in Fig. C.1(d). In the orange region, $\lambda_1 \sim 1$ [see, for instance, Fig. C.1(e)] and $\lambda_1 - \lambda_2 \neq 0$, and hence $\nu = 1$ which corresponds to the $\mathbb{Z}_2$ phase. The black region denotes the trivial phase with $\nu = 0$ because there is no $\lambda_1 \sim 1$. [See Fig. C.1(e)]. While the boundary of the $\mathbb{Z}_2$ phase is consistent with the TM, detection of the phase boundary between the ThM and the trivial phase requires deep consideration in some situations. In Fig. C.1(e), the two phases are distinguishable by the presence of the doublet structure, whereas in Fig. C.1(f), it is hard to tell whether the intermediate region between the $\mathbb{Z}_2$ and the trivial phase is a finite window of the ThM. As is seen in Fig. 3 of the main text, this is indeed a small window of ThM, which is unambiguously captured by the MLP.

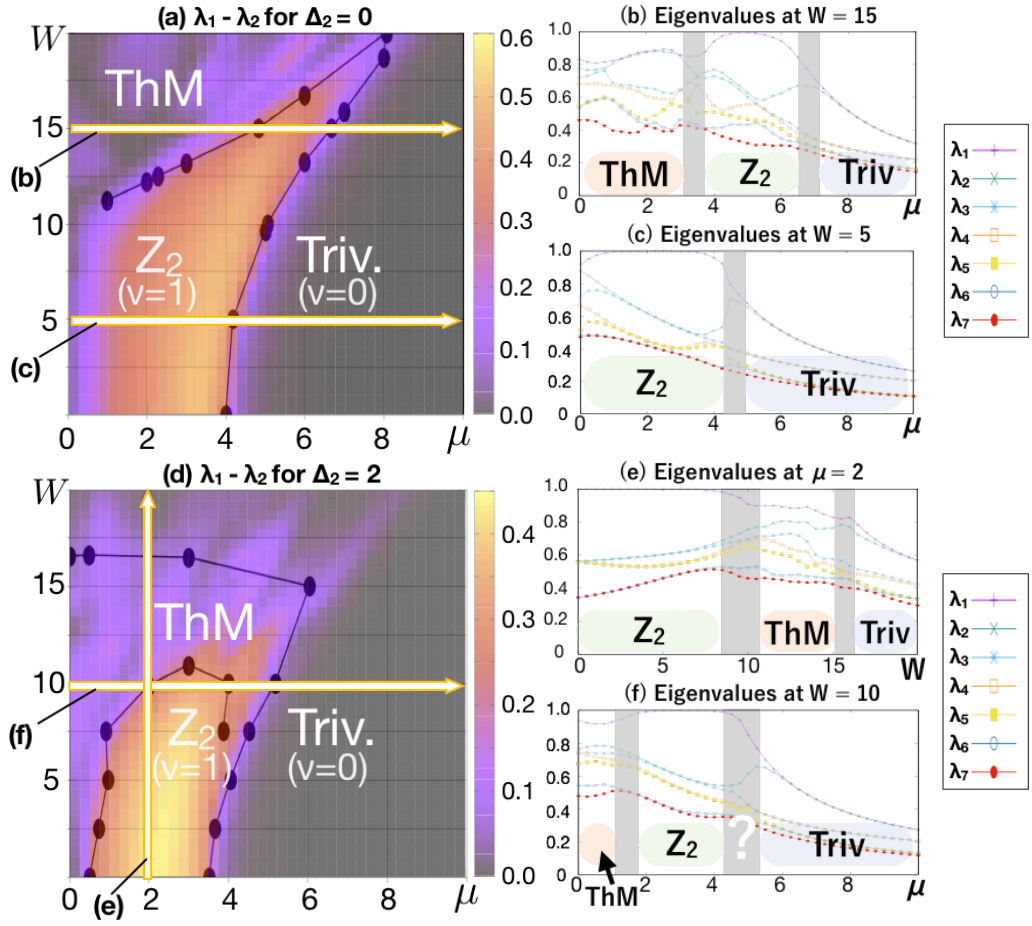

Figure C.1: (a) and (d) $\lambda_1 - \lambda_2$ as a function of the chemical potential μ and the disorder strength w for class DIII Hamiltonian given by Eq. (3.1) of the main text. The parameters are taken as $(t, \Delta, \Delta_2) =$ (a) (1, 3, 0) and (d) (1, 3, 2), respectively, and the system size is 20×20. (b), (c), (e), and (f) show μ and w dependences of the eigenvalues λ_i $(i = 1, 2, \ldots, 7)$ of the operator $\mathcal{A}$ on the system size 20×20. The parameters are taken as $(t, \Delta, \Delta_2, w) =$ (b) (1, 3, 0, 15), (c) (1, 3, 0, 5), (f) (1, 3, 2, 10), and (e) $(t, \Delta, \Delta_2, \mu) =$ (1, 3, 2, 2), respectively. The gray bars in (b), (c), (e), and (f) denote marginal areas.

D
Monte Carlo Sampling Algorithms

Monte Carlo simulation is a very powerful strategy based on random sampling when a problem is too difficult to solve analytically, or too demanding to perform a deterministic numerical calculation. One of its most successful application is the calculation of the statistical or thermodynamical property of a given classical model by generating Markov chains[*1]. Two conditions are frequently imposed on the transition matrix from state A to B, $\mathcal{T}(A \to B)$, to assure the unique stationary distribution:

1. *Detailed balance condition.* Given the likelihood, or the Boltzmann factor, of the objective states as π, the transition matrices obey

$$\frac{\mathcal{T}(A \to B)}{\mathcal{T}(B \to A)} = \frac{\pi(B)}{\pi(A)}. \tag{D.1}$$

2. *Ergodicity.* For any states A and B, there exists a set of intermediate states $\{X_i\}_{i=1}^{m}$ such that

$$\mathcal{T}(A \to X_1)\mathcal{T}(X_1 \to X_2) \cdots \mathcal{T}(X_m \to B) \neq 0. \tag{D.2}$$

In many situations, the transition matrix is constructed in a two-step manner [231]. Concretely, we take a product as $\mathcal{T}(A \to B) = T(A \to B)\alpha(A \to B)$ where T is the proposal rate which is usually sparse and α is the acceptance rate to assure the satisfaction of the detailed balance condition. The single-spin flip algorithm and the cluster update algorithm can be understood as examples of such strategy.

[*1] Let $P(X_i|X_{i-1}, ..., X_1)$ be the likelihood for the state of the system to be X_i in the i-th step with the previous states given as $X_1, ..., X_{i-1}$ from the beginning. The sampling is Markovian, i.e., we are generating a Markov chain, if

$$P(X_i|X_{i-1}, ..., X_1) = P(X_i|X_{i-1}).$$

D.1 Single-spin flip algorithm

The versatility and simplicity of the single-spin flip (SSF) algorithm[*2] allows us to apply it in various fields including condensed matter physics, statistical mechanics, and machine learning. In the following, we provide the overview of the SSF algorithm for the classical Ising model.

Let a Hamiltonian defined on a set of sites V be

$$H(\boldsymbol{\sigma}) = -\sum_{\mathcal{C}\subset V} J_{\mathcal{C}} \prod_{\sigma\in\mathcal{C}} \sigma, \tag{D.3}$$

where $\mathcal{C}$ is a support of a local interaction term, $J_{\mathcal{C}}$ is the amplitude of the interaction, and $\boldsymbol{\sigma} := (\sigma_1, \sigma_2, ..., \sigma_{|V|}) \in \mathcal{S}$ is a spin configuration where $\mathcal{S}$ being the set of all possible spin configurations. In a typical SSF algorithm, the proposal rate is given as

$$T(\boldsymbol{\sigma} \to \boldsymbol{\sigma}') = \begin{cases} 1/|V| & \text{if dist}(\boldsymbol{\sigma}, \boldsymbol{\sigma}')=1, \\ 0 & \text{otherwise,} \end{cases} \tag{D.4}$$

where $\text{dist}(\boldsymbol{\sigma}, \boldsymbol{\sigma}')$ is the count of spins different from each other. The acceptance rate is given by the well-known **Metropolis-Hastings rule** as

$$\alpha(\boldsymbol{\sigma} \to \boldsymbol{\sigma}') = \min\left(1, \exp(\beta(H(\boldsymbol{\sigma}) - H(\boldsymbol{\sigma}')))\right), \tag{D.5}$$

where β is the inverse temperature of the system. In many cases, repetition of Eq. (D.4) and (D.5) over $|V|$ times is defined as a single Monte Carlo step. We summarize the algorithm in Algorithm 4.

Algorithm 4 Single-spin flip algorithm for Ising models

Set inverse temperature β.
Set initial spin configuration $\boldsymbol{\sigma}$ on sites V.
while termination condition is not satisfied **do**
  for i-th flip trial out of $|V|$ trials **do**
    Proposal: Select random site (or choose sequentially).
    Acceptance: Flip the spin configuration with probability $\min(1, \exp(-\beta\Delta H))$.
  end for
end while

[*2] It is also referred to as the local update algorithm.

D.2 Cluster update algorithm without magnetic fields

As is discussed in Chapter 4, the cluster update algorithm by Swendsen and Wang was initially developed to speed up the pre-thermalization and reduce the autocorrelation time in Monte Carlo simulation of the classical Ising model on square lattice [139]. In the following, we assume a Ising model with merely two-spin interaction defined on a graph $G = (V, E)$ as

$$H = -\sum_{\langle i,j\rangle \in E} J_{ij}\sigma_i\sigma_j, \tag{D.6}$$

where J_{ij} is the interaction between the i-th and j-th sites. We provide the pseudo-code in Algorithm 5.

Algorithm 5 Cluster Update Algorithm by Swendsen and Wang

```
Set inverse temperature β.
Set initial spin configuration σ.
while termination condition is not satisfied do
    for every edge ⟨i, j⟩ with non-zero interaction do
        Connect the edge with probability δ_{σ_i,σ_j} (1 − 2 exp(−βJ_ij))
    end for
    Compute the clusters, i.e., the sets of connected sites.
    for every cluster do
        Flip all the spins in cluster with probability 1/2.
    end for
end while
```

D.3 Cluster update under magnetic fields

In this Appendix, we introduce two flavors of cluster updates accompanied with magnetic fields. We assume a model defined on a graph $G = (V, E)$ as follows:

$$H = -\sum_{\langle i,j\rangle \in E} J_{ij}\sigma_i\sigma_j - \sum_{i\in V} h_i\sigma_i, \tag{D.7}$$

where J_{ij} is the two-spin interaction between two binary degrees of freedom at sites i and j, or σ_i and σ_j, and h_i is the external field on site i. One way to take the

external field into account is to modify the probability of flipping the cluster that is formed using the information on the interactions, and the other is to extend the space to express the field terms by interactions with the auxiliary space.

To introduce the first approach, let us remind that the detailed balance condition under the two-step strategy is given as,

$$\frac{\pi(B)}{\pi(A)} = \frac{T(A \to B)\alpha(A \to B)}{T(B \to A)\alpha(B \to A)}. \tag{D.8}$$

The cluster update algorithm in the previous section is rejection-free under $h_i = 0$. Since the external field modifies the Boltzmann weight as $\pi(A) \to e^{-\beta \sum_i h_i \sigma_i^A} \cdot \pi(A)$ at the inverse temperature β, the trial proposal must absorb such change to realize a rejection-free scheme in an arbitrary external field. Concretely, the k-th cluster C_k formed by the ordinary bonding process is flipped with probability $p_k = e^{-\beta m_k}/(e^{-\beta m_k} + e^{+\beta m_k})$ where $m_k = -\sum_{i \in C_k} h_i \sigma_i$ is the Zeeman energy by the external field. The additional computational effort per single MC step is ignorable.

In the second approach, known as the "ghost spin method," one introduces an auxiliary spin that interacts with any spin exposed to the external (or virtual) field [232, 233]. Defining $\widetilde{G} = (\widetilde{V}, \widetilde{E})$ with the ghost spin on the 0-th site as

$$V \to \widetilde{V} = \{0\} \cap V, \tag{D.9}$$

$$E \to \widetilde{E} = \{\langle 0, i\rangle | i \in V\}, \tag{D.10}$$

we alternatively consider a Hamiltonian as follows,

$$\widetilde{H} = -\sum_{\langle i,j\rangle \in \widetilde{E}} \widetilde{J}_{ij} \sigma_i \sigma_j, \tag{D.11}$$

where

$$\widetilde{J}_{ij} = \begin{cases} J_{i,j} & \text{if } \langle i, j\rangle \in E \\ h_i & \text{if } j = 0 \\ h_j & \text{if } i = 0 \end{cases}. \tag{D.12}$$

Now that the new Hamiltonian consists solely of two-spin interactions, the ordinary cluster update can be applied.

D.4 Observation of physical quantity in extended model

The transformation considered in the main text preserves the partition function, and moreover the Boltzmann factor for visible spin configurations. There-

fore, to compute the expectation value of a physical observable $O(\boldsymbol{\sigma})$ in the extended space, one may simply consider the identical mapping $\widetilde{O}(\sigma, h) = O(\sigma)$ to obtain

$$\begin{aligned} \langle O \rangle &= \frac{\sum_{\sigma,h} \widetilde{O}(\sigma,h)\widetilde{\pi}(\sigma,h)}{\sum_{\sigma,h} \widetilde{\pi}(\sigma,h)} = \frac{\sum_{\sigma} O(\sigma) \left(\sum_{h} \widetilde{\pi}(\sigma,h)\right)}{Z} \\ &= \frac{\sum_{\sigma} O(\sigma)\pi(\sigma)}{Z}. \end{aligned} \tag{D.13}$$

In other words, one may simply ignore all the hidden spins and compute the quantities using the operator in the original space.

E
Partition Function of Three-spin Interacting Model on Kagomé Lattice

In this Appendix, we show that a model with only three-spin interactions on the Kagomé lattice is soluble. This model is a specific case of a broader class of models with crossing symmetry studied in Ref. [234], which do not exhibit a phase transition at finite temperature. The partition function is written as

$$Z = \sum_{\boldsymbol{\sigma}} \exp\left[\sum_{\triangle} M_{\triangle}\tau_{\triangle} + \sum_{\triangledown} M_{\triangledown}\tau_{\triangledown}\right], \tag{E.1}$$

where $M_{\triangle}$ denotes the three-spin interaction and $\tau_{\triangle} := \prod_{j\in\triangle}\sigma_j$ the product of the Ising spins in an upward triangle in the lattice. Also $M_{\triangledown}$ and $\tau_{\triangledown}$ are defined similarly for a downward triangle. In order to compute Eq. (E.1), we introduce the identity for a binary variable $x = \pm 1$ as follows,

$$e^{Kx} = \cosh(K) \sum_{n=0,1} (x\ \tanh(K))^n . \tag{E.2}$$

Applying this identity to each triangle yields

$$\begin{aligned} Z &= \sum_{\boldsymbol{\sigma}} \sum_{n_{\triangle}, n_{\triangledown}} \prod_{\triangle}\prod_{\triangledown} \cosh(M_{\triangle})\cosh(M_{\triangledown}) \\ &\quad \times \left(\tau_{\triangle}\tanh(M_{\triangle})\right)^{n_{\triangle}} \left(\tau_{\triangledown}\tanh(M_{\triangledown})\right)^{n_{\triangledown}} . \end{aligned} \tag{E.3}$$

Next, let us consider taking the sum over σ_j at some site j in Eq. (E.1). Denoting the triangles touching the site j as $\triangle(j)$ and $\triangledown(j)$, the contribution from the spin at j can be given as $\sum_{\sigma_j} \sigma_j^{n_{\triangle(j)}+n_{\triangledown(j)}}$, which is nonzero only when $n_{\triangle(j)} = n_{\triangledown(j)}$. This argument holds for arbitrary j, and therefore the requirement $n_{\triangle} = n_{\triangledown} = 0, 1$ for all $\triangle$ and $\triangledown$ imposed for nonzero contribution. Accordingly, we obtain the concise expression of the partition function as

$$Z = C\left(1 + \prod_{\triangle,\triangledown} \tanh(M_{\triangle})\tanh(M_{\triangledown})\right), \tag{E.4}$$

where $C = 2^{N_v} \prod_{\triangle} \prod_{\triangledown} \cosh(M_{\triangle}) \cosh(M_{\triangledown})$ with N_v being the number of visible spins, i.e., the number of sites. The above expression clearly shows that the free energy in the thermodynamic limit is analytic, and hence the model does not show a phase transition at finite temperature. For $M_{\triangle} = M_{\triangledown}$, Eq. (E.4) reproduces the partition function of the uniform model studied in Ref. [235]. We note that the present method is not limited to two-dimensional models. In fact, a similar model with four-spin interactions on a three-dimensional pyrochlore lattice is also soluble using the same technique [236].

F
Approximating Random Density Matrices by Neural Networks

In this appendix, we randomly generate a density matrix and fit it by the NSS to see that the expressive power of the ansatz does not assure efficient representation of all volume-law states. Here, random density matrices are generated as

$$\hat{\rho} = \frac{\hat{X}^2}{\mathrm{Tr}[\hat{X}^2]}, \tag{F.1}$$

where $\hat{X}$ is sampled from the Gaussian unitary ensemble of random Hermitian matrices. We have numerically checked that the operator space entanglement entropy defined as in the main text exhibits a volume-law scaling, i.e., operator space entanglement entropy $\propto L$ for matrices with size $2^L \times 2^L$ (data not shown).

Figure F.1 shows that while a random density matrix generated following Eq. (F.1) can be approximated better by the NSS with larger α, or the number ratio of the spins, the number of parameters and accordingly the numerical cost required to reach some fixed fidelity increase rapidly.

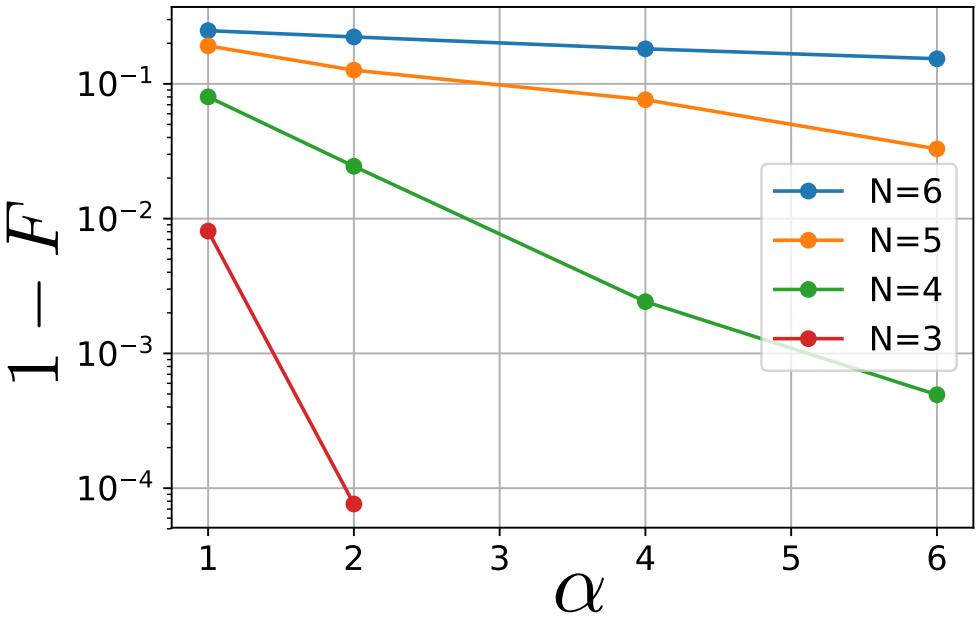

Figure F.1: The infidelity $1 - F$ of the NSS fitted to a random density matrix generated by Eq. (F.1). While the NSS with larger α, or the number ratio of the spins, better approximates the random density matrices, the number of parameters and accordingly the numerical cost required to reach some fixed fidelity increase rapidly.

G
Computational Cost of Stationary-State Search Algorithms

Here, we compare the computational cost of the NSS algorithm and the Lanczos method. While cost for the Lanczos method largely depends on the sparcity of the target matrix, it is at least linear with respect to the matrix dimension; it scales exponentially with respect to the total number of spins. The largest bottleneck of the NSS algorithm is the calculation of the inverse matrix of the quantum Fisher information S, and the second being the evaluation via Monte Carlo sampling of force f and S. Given the number of parameters as N_p, the number of epochs as N_{it}, and the sampling number per epoch as N_{samp}, the computational cost would be given as

$$O\left(N_{\mathrm{it}}(N_p^3 + N_{\mathrm{samp}}N_p^2)\right). \tag{G.1}$$

Under the periodic boundary condition, the number of parameters are $\sim \alpha N$ with α being the number ratio of spins and N being the system size. Note that although the computational cost scales polynomially with respect to the number of parameters, there might be hidden dependence of α, N_{samp}, and N_{it} on system size to reach certain accuracy.

In Fig. G.1, we show the wall time for calculating the stationary states by optimization of the NSS and the Lanczos method. Our variational method exhibits only polynomial scaling which is, clearly, far more efficient than the exponential scaling in the Lanczos method. We leave the comparison of the scaling behaviour between the tensor network ansatz in 1d/2d and our method as a future task.

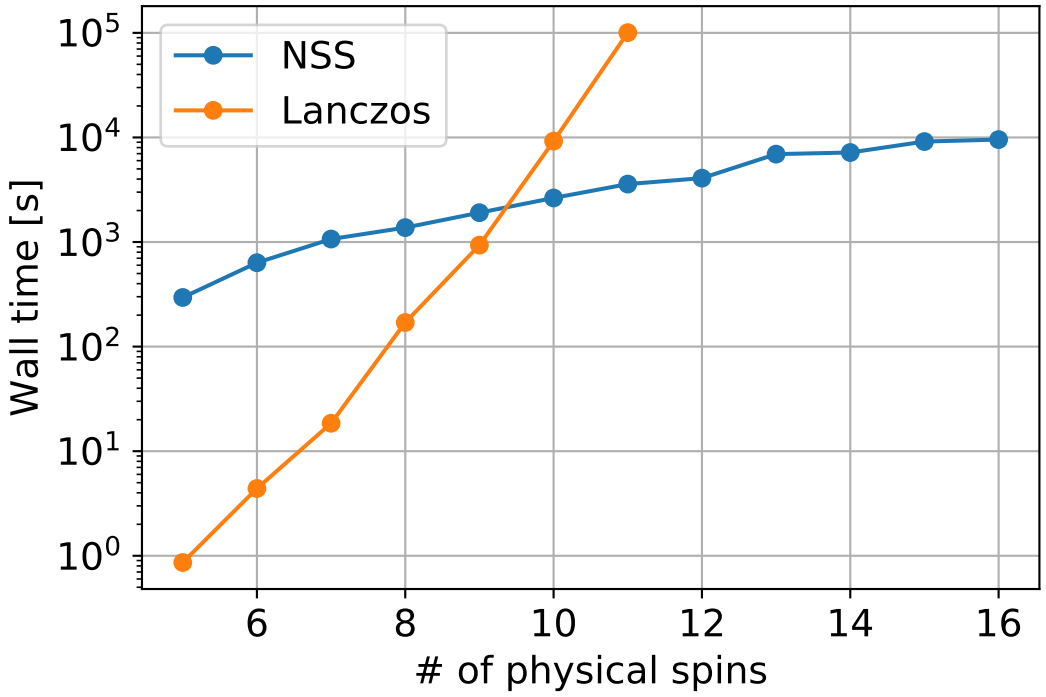

Figure G.1: The wall times for computing the stationary state of the 1D transverse-field Ising model with $V = 2, g = 1$, and $\gamma = 1$. The blue and orange dots are for the NSS ansatz optimization and the Lanczos method, respectively. Here, the number ratio of the spins is $\alpha = 4$. The NSS ansatz exhibits lower scaling as a function of the number of physical spins. The number of sampling is $N_s = 2000$ repeated for $N_{\mathrm{it}} = 1500$ iterations, which we find to be sufficient for the convergence of the VMC calculation. The computation for the NSS and Lanczos is executed on 8 cores on Intel(R) Core i7-6820HQ and 12 cores on Intel(R) Xeon(R) Silver 4110, respectively.

Bibliography

[1] A. Krizhevsky, I. Sutskever, and G. E. Hinton,
"Imagenet classification with deep convolutional neural networks",
in Advances in neural information processing systems (2012),
pp. 1097–1105.

[2] G. Hinton, L. Deng, D. Yu, G. Dahl, A.-r. Mohamed, N. Jaitly, A. Senior,
V. Vanhoucke, P. Nguyen, B. Kingsbury, and T Sainath,
"Deep neural networks for acoustic modeling in speech recognition",
IEEE Signal processing magazine **29**, 82 (2012).

[3] D. Bahdanau, K. Cho, and Y. Bengio,
"Neural machine translation by jointly learning to align and translate",
arXiv:1409.0473 (2014).

[4] Y. LeCun, Y. Bengio, and G. Hinton, "Deep learning", Nature **521**, 436–444
(2015).

[5] H. W. Lin, M. Tegmark, and D. Rolnick,
"Why does deep and cheap learning work so well?",
Journal of Statistical Physics **168**, 1223–1247 (2017).

[6] T. M. Mitchell et al., *Machine learning*, Vol. 45, 37 (1997), pp. 870–877.

[7] I. Goodfellow, Y. Bengio, and A. Courville, *Deep learning*
(MIT press, 2016).

[8] Y. Taigman, M. Yang, M. Ranzato, and L. Wolf, "Deepface: closing the gap
to human-level performance in face verification", in Proceedings of the
ieee conference on computer vision and pattern recognition (2014),
pp. 1701–1708.

[9] J. Carrasquilla and R. G. Melko, "Machine learning phases of matter",
Nat. Phys. **13**, 431–434 (2017).

[10] D. Kim and D.-H. Kim,
"Smallest neural network to learn the ising criticality",
Phys. Rev. E **98**, 022138 (2018).

[11] L. Wang, "Discovering phase transitions with unsupervised learning",
Phys. Rev. B **94**, 195105 (2016).

[12] S. J. Wetzel, "Unsupervised learning of phase transitions: from principal component analysis to variational autoencoders",
Phys. Rev. E **96**, 022140 (2017).

[13] W. Hu, R. R. P. Singh, and R. T. Scalettar,
"Discovering phases, phase transitions, and crossovers through unsupervised machine learning: a critical examination",
Phys. Rev. E **95**, 062122 (2017).

[14] P. Ponte and R. G. Melko, "Kernel methods for interpretable machine learning of order parameters", Phys. Rev. B **96**, 205146 (2017).

[15] L. Wang,
"Exploring cluster monte carlo updates with boltzmann machines",
Phys. Rev. E **96**, 051301(R) (2017).

[16] S. J. Wetzel and M. Scherzer, "Machine learning of explicit order parameters: from the ising model to su(2) lattice gauge theory",
Phys. Rev. B **96**, 184410 (2017).

[17] F. Schindler, N. Regnault, and T. Neupert,
"Probing many-body localization with neural networks",
Phys. Rev. B **95**, 245134 (2017).

[18] J. Venderley, V. Khemani, and E.-A. Kim,
"Machine learning out-of-equilibrium phases of matter",
Phys. Rev. Lett. **120**, 257204 (2018).

[19] Y.-T. Hsu, X. Li, D.-L. Deng, and S. D. Sarma, "Machine learning many-body localization: search for the elusive nonergodic metal",
Phys. Rev. Lett. **121**, 245701 (2018).

[20] E. van Nieuwenburg, E. Bairey, and G. Refael,
"Learning phase transitions from dynamics",
Phys. Rev. B **98**, 060301 (2018).

[21] R. Nandkishore and D. A. Huse, "Many-body localization and thermalization in quantum statistical mechanics", Annual Review of Condensed Matter Physics **6**, 15–38 (2015).

[22] F. Alet and N. Laflorencie, "Many-body localization: an introduction and selected topics", Comptes Rendus Physique **19**, 498 –525 (2018).

[23] E. V. H. Doggen, F. Schindler, K. S. Tikhonov, A. D. Mirlin, T. Neupert, D. G. Polyakov, and I. V. Gornyi, "Many-body localization and delocalization in large quantum chains", Phys. Rev. B **98**, 174202 (2018).

[24] T. Ando, "Theory of quantum transport in a two-dimensional electron system under magnetic fields. iii. many-site approximation", J. Phys. Soc. Jpn. **37**, 622–630 (1974).

[25] K. v. Klitzing, G. Dorda, and M. Pepper, "New method for high-accuracy determination of the fine-structure constant based on quantized hall resistance", Phys. Rev. Lett. **45**, 494–497 (1980).

[26] Y. Zhang and E.-A. Kim, "Quantum loop topography for machine learning", Phys. Rev. Lett. **118**, 216401 (2017).

[27] P. Zhang, H. Shen, and H. Zhai, "Machine learning topological invariants with neural networks", Phys. Rev. Lett. **120**, 066401 (2018).

[28] T. Ohtsuki and T. Ohtsuki, "Deep learning the quantum phase transitions in random Two-Dimensional electron systems", J. Phys. Soc. Jpn. **85**, 123706 (2016).

[29] T. Ohtsuki and T. Ohtsuki, "Deep learning the quantum phase transitions in random electron systems: applications to three dimensions", J. Phys. Soc. Jpn. **86**, 044708 (2017).

[30] E. P. L. Nieuwenburg, Y.-H. Liu, and S. D. Huber, "Learning phase transitions by confusion", Nat. Phys. **13**, 435 (2017).

[31] P. Broecker, F. F. Assaad, and S. Trebst, "Quantum phase recognition via unsupervised machine learning", arXiv:1707.00663 (2017).

[32] E. Stoudenmire and D. J. Schwab,
"Supervised learning with tensor networks",
in Advances in neural information processing systems (2016),
pp. 4799–4807.

[33] I. Glasser, N. Pancotti, and J. I. Cirac,
"Supervised learning with generalized tensor networks",
arXiv preprint arXiv:1806.05964 (2018).

[34] Z.-Y. Han, J. Wang, H. Fan, L. Wang, and P. Zhang,
"Unsupervised generative modeling using matrix product states",
Phys. Rev. X **8**, 031012 (2018).

[35] E. M. Stoudenmire,
"Learning relevant features of data with multi-scale tensor networks",
Quantum Science and Technology **3**, 034003 (2018).

[36] S. Efthymiou, J. Hidary, and S. Leichenauer,
"Tensornetwork for machine learning", arXiv preprint arXiv:1906.06329
(2019).

[37] B. S. Rem, N. Käming, M. Tarnowski, L. Asteria, N. Fläschner, C. Becker,
K. Sengstock, and C. Weitenberg, "Identifying quantum phase transitions
using artificial neural networks on experimental data",
Nature Physics **15**, 917–920 (2019).

[38] A. Bohrdt, C. S. Chiu, G. Ji, M. Xu, D. Greif, M. Greiner, E. Demler,
F. Grusdt, and M. Knap, "Classifying snapshots of the doped Hubbard
model with machine learning", Nature Physics **15**, 921–924 (2019).

[39] Y. Zhang, A Mesaros, K Fujita, S. Edkins, M. Hamidian, K Ch'ng,
H Eisaki, S Uchida, J. Davis, E Khatami, and E.-A Kim,
"Machine learning in electronic-quantum-matter imaging experiments",
Nature **570**, 484–490 (2019).

[40] H. C. Nguyen, R. Zecchina, and J. Berg, "Inverse statistical problems:
from the inverse ising problem to data science",
Advances in Physics **66**, 197–261 (2017).

[41] T. Tanaka, "Mean-field theory of boltzmann machine learning",
Physical Review E **58**, 2302 (1998).

[42] R. Salakhutdinov and H. Larochelle,
"Efficient learning of deep boltzmann machines", in Proceedings of the thirteenth international conference on artificial intelligence and statistics (2010), pp. 693–700.

[43] J. Sohl-Dickstein, P. B. Battaglino, and M. R. DeWeese,
"New method for parameter estimation in probabilistic models: minimum probability flow", Phys. Rev. Lett. **107**, 220601 (2011).

[44] D. Wu, L. Wang, and P. Zhang, "Solving statistical mechanics using variational autoregressive networks", Phys. Rev. Lett. **122**, 080602 (2019).

[45] G. Torlai and R. G. Melko,
"Learning thermodynamics with boltzmann machines",
Phys. Rev. B **94**, 165134 (2016).

[46] A. Morningstar and R. G. Melko,
"Deep learning the ising model near criticality",
The Journal of Machine Learning Research **18**, 5975–5991 (2017).

[47] J. Liu, Y. Qi, Z. Y. Meng, and L. Fu, "Self-learning monte carlo method", Phys. Rev. B **95**, 041101 (2017).

[48] L Huang and L Wang, "Accelerated monte carlo simulations with restricted boltzmann machines", Phys. Rev. B **95**, 035105 (2017).

[49] F. Verstraete, V. Murg, and J. Cirac,
"Matrix product states, projected entangled pair states, and variational renormalization group methods for quantum spin systems",
Advances in Physics **57**, 143–224 (2008).

[50] R. Orús, "Tensor networks for complex quantum systems",
Nature Reviews Physics **1**, 538–550 (2019).

[51] S. R. White,
"Density matrix formulation for quantum renormalization groups",
Phys. Rev. Lett. **69**, 2863–2866 (1992).

[52] M. B. Hastings, "Solving gapped hamiltonians locally",
Phys. Rev. B **73**, 085115 (2006).

[53] M. B. Hastings, "An area law for one-dimensional quantum systems",
J. Stat. Mech. **2007**, P08024 (2007).

[54] M. B. Hastings, "Entropy and entanglement in quantum ground states", Phys. Rev. B **76**, 035114 (2007).

[55] F. Verstraete, M. M. Wolf, and J. I. Cirac, "Quantum computation and quantum-state engineering driven by dissipation", Nature physics **5**, 633 (2009).

[56] G. Vidal, "Entanglement renormalization", Phys. Rev. Lett. **99**, 220405 (2007).

[57] Y.-Y. Shi, L.-M. Duan, and G. Vidal, "Classical simulation of quantum many-body systems with a tree tensor network", Phys. Rev. A **74**, 022320 (2006).

[58] G. Carleo, I. Cirac, K. Cranmer, L. Daudet, M. Schuld, N. Tishy, L. Vogt-Maranto, and L. Zdeborova, arXiv:1903.10563 (2019).

[59] R. G. Melko, G. Carleo, J. Carrasquilla, and J. I. Cirac, "Restricted Boltzmann machines in quantum physics", Nature Physics **15**, 887–892 (2019).

[60] S. D. Sarma, D.-L. Deng, and L.-M. Duan, "Machine learning meets quantum physics", arXiv preprint arXiv:1903.03516 (2019).

[61] G. Carleo and M. Troyer, "Solving the quantum many-body problem with artificial neural networks", Science **355**, 602–606 (2017).

[62] D.-L. Deng, X. Li, and S. Das Sarma, "Quantum entanglement in neural network states", Phys. Rev. X **7**, 021021 (2017).

[63] Y. Nomura, A. S. Darmawan, Y. Yamaji, and M. Imada, "Restricted boltzmann machine learning for solving strongly correlated quantum systems", Phys. Rev. B **96**, 205152 (2017).

[64] Z. Cai and J. Liu, "Approximating quantum many-body wave functions using artificial neural networks", Phys. Rev. B **97**, 035116 (2018).

[65] H. Saito, "Solving the bose-hubbard model with machine learning", J. Phys. Soc. Jpn. **86**, 093001 (2017).

[66] H. Saito and M. Kato, "Machine learning technique to find quantum many-body ground states of bosons on a lattice", J. Phys. Soc. Jpn. **87**, 014001 (2018).

[67] I. Glasser, N. Pancotti, M. August, I. D. Rodriguez, and J. I. Cirac, "Neural-network quantum states, string-bond states, and chiral topological states", Phys. Rev. X **8**, 011006 (2018).

[68] R. Kaubruegger, L. Pastori, and J. C. Budich, "Chiral topological phases from artificial neural networks", Phys. Rev. B **97**, 195136 (2018).

[69] Y. Huang and J. E. Moore, *Neural network representation of tensor network and chiral states*, 2017.

[70] T. Vieijra, C. Casert, J. Nys, W. De Neve, J. Haegeman, J. Ryckebusch, and F. Verstraete, "Restricted boltzmann machines for quantum states with nonabelian or anyonic symmetries", arXiv preprint arXiv:1905.06034 (2019).

[71] D.-L. Deng, X. Li, and S. Das Sarma, "Machine learning topological states", Phys. Rev. B **96**, 195145 (2017).

[72] Z.-A. Jia, Y.-H. Zhang, Y.-C. Wu, L. Kong, G.-C. Guo, and G.-P. Guo, "Efficient machine-learning representations of a surface code with boundaries, defects, domain walls, and twists", Phys. Rev. A **99**, 012307 (2019).

[73] S. Lu, X. Gao, and L.-M. Duan, "Efficient representation of topologically ordered states with restricted boltzmann machines", Phys. Rev. B **99** (2019).

[74] K. Choo, T. Neupert, and G. Carleo, "Two-dimensional frustrated $J1-J2$ model studied with neural network quantum states", Phys. Rev. B **100**, 125124 (2019).

[75] X. Liang, W.-Y. Liu, P.-Z. Lin, G.-C. Guo, Y.-S. Zhang, and L. He, "Solving frustrated quantum many-particle models with convolutional neural networks", Phys. Rev. B **98**, 104426 (2018).

[76] F. Ferrari, F. Becca, and J. Carrasquilla, "Neural gutzwiller-projected variational wave functions", Phys. Rev. B **100** (2019).

[77] X. Gao and L.-M. Duan, "Efficient representation of quantum many-body states with deep neural networks", Nat. Commun. **8**, 662 (2017).

[78] J. Chen, S. Cheng, H. Xie, L. Wang, and T. Xiang, "Equivalence of restricted boltzmann machines and tensor network states", Phys. Rev. B **97**, 085104 (2018).

[79] S. R. Clark, "Unifying neural-network quantum states and correlator product states via tensor networks", Journal of Physics A: Mathematical and Theoretical **51**, 135301 (2018).

[80] G. Carleo, Y. Nomura, and M. Imada, "Constructing exact representations of quantum many-body systems with deep neural networks", Nat. Commun. **9**, 5322 (2018).

[81] N. Freitas, G. Morigi, and V. Dunjko, "Neural network operations and susuki–trotter evolution of neural network states", International Journal of Quantum Information **16**, 1840008 (2018).

[82] K. Choo, G. Carleo, N. Regnault, and T. Neupert, "Symmetries and many-body excitations with neural-network quantum states", Phys. Rev. Lett. **121**, 167204 (2018).

[83] N. Irikura and H. Saito, "Neural-network quantum states at finite temperature", (2019).

[84] F. Rosenblatt, "The perceptron: a probabilistic model for information storage and organization in the brain.", Psychological review **65**, 386 (1958).

[85] G Cybenko, Math. Control Signals Systems **2**, 303 (1989).

[86] K Hornik, M Stinchcombe, and H White, Neural Networks **2**, 359 (1989).

[87] K. Hornik, "Approximation capabilities of multilayer feedforward networks", Neural Networks **4**, 251 –257 (1991).

[88] K. Fukushima, "Neocognitron: a self-organizing neural network model for a mechanism of pattern recognition unaffected by shift in position", Biological cybernetics **36**, 193–202 (1980).

[89] Y. LeCun, B. Boser, J. S. Denker, D. Henderson, R. E. Howard, W. Hubbard, and L. D. Jackel, "Backpropagation applied to handwritten zip code recognition", Neural computation **1**, 541–551 (1989).

[90] K. Simonyan and A. Zisserman,
"Very deep convolutional networks for large-scale image recognition",
arXiv preprint arXiv:1409.1556 (2014).

[91] Y. Levine, O. Sharir, N. Cohen, and A. Shashua,
"Quantum entanglement in deep learning architectures",
Phys. Rev. Lett. **122**, 065301 (2019).

[92] P Smolensky,
Parallel Distributed Processing: Volume 1: Foundations (MIT Press, Cambridge, 1986).

[93] N. Le Roux and Y. Bengio, "Representational power of restricted
boltzmann machines and deep belief networks",
Neural Computation **20**, 1631–1649 (2008).

[94] G. E. Hinton, S. Osindero, and Y.-W. Teh,
"A fast learning algorithm for deep belief nets",
Neural computation **18**, 1527–1554 (2006).

[95] Y. Bengio, P. Lamblin, D. Popovici, and H. Larochelle,
"Greedy layer-wise training of deep networks",
Advances in neural information processing systems, 153–160 (2007).

[96] D. J. Thouless, M Kohmoto, M. P. Nightingale, and M den Nijs,
"Quantized hall conductance in a two-dimensional periodic potential",
Phys. Rev. Lett. **49**, 405 (1982).

[97] M Kohmoto,
"Topological invariant and the quantization of the hall conductance",
Ann. Phys. (NY) **160**, 343 (1985).

[98] C. L. Kane and E. J. Mele,
"Z2 topological order and the quantum spin hall effect",
Phys. Rev. Lett. **95**, 146802 (2005).

[99] C. L. Kane and E. J. Mele, "Quantum spin hall effect in graphene",
Phys. Rev. Lett. **95**, 226801 (2005).

[100] M. Z. Hasan and C. L. Kane, "Colloquium: topological insulators",
Rev. Mod. Phys. **82**, 3045–3067 (2010).

[101] H. Katsura and T. Koma, "The 2 index of disordered topological
insulators with time reversal symmetry", J. Math. Phys. **57**, 021903 (2016).

[102] H. Katsura and T. Koma,
"The noncommutative index theorem and the periodic table for disordered topological insulators and superconductors",
J. Math. Phys. **59**, 031903 (2018).

[103] Q. Niu, D. J. Thouless, and Y.-S. Wu,
"Quantized hall conductance as a topological invariant",
Phys. Rev. B **31**, 3372–3377 (1985).

[104] T. A. Loring and M. B. Hastings,
"Disordered topological insulators via c∗ − *algebras*",
EPL **92**, 67004 (2010).

[105] H.-M. Guo, "Topological invariant in three-dimensional band insulators with disorder", Phys. Rev. B **82**, 115122 (2010).

[106] I. C. Fulga, F. Hassler, and A. R. Akhmerov,
"Scattering theory of topological insulators and superconductors",
Phys. Rev. B **85**, 165409 (2012).

[107] B. Leung and E. Prodan, "Effect of strong disorder in a three-dimensional topological insulator: phase diagram and maps of the 2 invariant",
Phys. Rev. B **85**, 205136 (2012).

[108] B. Sbierski and P. W. Brouwer, "2 phase diagram of three-dimensional disordered topological insulators via a scattering matrix approach",
Phys. Rev. B **89**, 155311 (2014).

[109] T. A. Loring, "K-theory and pseudospectra for topological insulators",
Ann. Phys. **356**, 383 –416 (2015).

[110] T. A. Loring and H. Schulz-Baldes,
"Finite volume calculation of k-theory invariants.", New York J. Math. **23** (2017).

[111] Y. Akagi, H. Katsura, and T. Koma, "A new numerical method for ℤ_2 topological insulators with strong disorder", J. Phys. Soc. Jpn. **86**, 123710 (2017).

[112] A. P. Schnyder, S. Ryu, A. Furusaki, and A. W. W. Ludwig,
"Classification of topological insulators and superconductors in three spatial dimensions", Phys. Rev. B **78**, 195125 (2008).

[113] A. Y. Kitaev,
"Periodic table for topological insulators and superconductors",
AIP Conf. Proc. **1134**, 22 (2009).

[114] A. Altland and M. R. Zirnbauer, "Nonstandard symmetry classes in mesoscopic normal-superconducting hybrid structures",
Phys. Rev. B **55**, 1142–1161 (1997).

[115] P. Anderson, "Absence of diffusion in certain random lattices",
Phys. Rev. **109**, 1492 (1958).

[116] A. MacKinnon and B. Kramer, "The scaling theory of electrons in disordered solids: additional numerical results",
Z. Phys. B **53**, 1–13 (1983).

[117] M Diez, I. C. Fulga, D. I. Pikulin, J Tworzydło, and C. W. J. Beenakker, "Bimodal conductance distribution of kitaev edge modes in topological superconductors", New J. Phys. **16**, 063049 (2014).

[118] I. C. Fulga, A. R. Akhmerov, J. Tworzydło, B. Béri, and C. W. J. Beenakker, "Thermal metal-insulator transition in a helical topological superconductor", Phys. Rev. B **86**, 054505 (2012).

[119] A. Kitaev, "Fault-tolerant quantum computation by anyons",
Ann. Phys. (NY) **303**, 2 –30 (2003).

[120] S. B. Bravyi and A. Y. Kitaev, "Fermionic quantum computation",
Ann. Phys. (NY) **298**, 210 –226 (2002).

[121] L. A. Wray, S.-Y. Xu, Y. Xia, Y. S. Hor, D. Qian, A. V. Fedorov, H. Lin, A. Bansil, R. J. Cava, and M. Z. Hasan, "Observation of topological order in a superconducting doped topological insulator",
Nat. Phys. **6**, 855–859 (2010).

[122] L. Fu and E. Berg, "Odd-Parity topological superconductors: theory and application to CuxBi2Se3", Phys. Rev. Lett. **105**, 097001 (2010).

[123] Z. Wang, P. Zhang, G. Xu, L. K. Zeng, H. Miao, X. Xu, T. Qian, H. Weng, P. Richard, A. V. Fedorov, H. Ding, X. Dai, and Z. Fang,
"Topological nature of the fese0.5te0.5 superconductor",
Phys. Rev. B **92**, 115119 (2015).

[124] P. Zhang, K. Yaji, T. Hashimoto, Y. Ota, T. Kondo, K. Okazaki, Z. Wang, J. Wen, G. D. Gu, H. Ding, and S. Shin, "Observation of topological superconductivity on the surface of an iron-based superconductor", Science **360**, 182 (2018).

[125] M Sato and S Fujimoto, "Topological phases of noncentrosymmetric superconductors: edge states, majorana fermions, and non-Abelian statistics", Phys. Rev. B **79**, 094504 (2009).

[126] M. R. Zirnbauer, "Riemannian symmetric superspaces and their origin in random-matrix theory", Journal of Mathematical Physics **37**, 4986–5018 (1996).

[127] L. Fu and C. L. Kane, "Topological insulators with inversion symmetry", Phys. Rev. B **76**, 045302 (2007).

[128] X.-L. Qi, T. L. Hughes, and S.-C. Zhang, "Topological invariants for the fermi surface of a time-reversal-invariant superconductor", Phys. Rev. B **81**, 134508 (2010).

[129] E Abrahams, P. W. Anderson, D. C. Licciardello, and T. V. Ramakrishnan, "Scaling theory of localization: absence of quantum diffusion in two dimensions", Phys. Rev. Lett. **42**, 673 (1979).

[130] S Hikami, "Anderson localization in a nonlinear- σ -model representation", Phys. Rev. B **24**, 2671 (1981).

[131] F. Evers and A. D. Mirlin, "Anderson transitions", Rev. Mod. Phys. **80**, 1355–1417 (2008).

[132] T. Senthil and M. P. A. Fisher, "Z2 gauge theory of elecron fractionalization in strongly correlated systems", Phys. Rev. B **62**, 7850–7881 (2000).

[133] C. M. Bishop, *Pattern recognition and machine learning* (Springer Science+ Business Media, 2006).

[134] J. Duchi, E. Hazan, and Y. Singer, "Adaptive subgradient methods for online learning and stochastic optimization", J. Mach. Learn. Res. **12**, 2121–2159 (2011).

[135] D. E. Rumelhart, G. E. Hinton, and R. J. Williams, "Learning representations by back-propagating errors", Nature **323**, 533–536 (1986).

[136] N. Srivastava, G. Hinton, A. Krizhevsky, I. Sutskever, and R. Salakhutdinov, "Dropout: a simple way to prevent neural networks from overfitting", J. Mach. Learn. Res. **15**, 1929–1958 (2014).

[137] M. V. Medvedyeva, J Tworzydło, and C. W. J. Beenakker, "Effective mass and tricritical point for lattice fermions localized by a random mass", Phys. Rev. B **81**, 214203 (2010).

[138] H. Araki, T. Mizoguchi, and Y. Hatsugai, "Phase diagram of a disordered higher-order topological insulator: a machine learning study", Phys. Rev. B **99**, 085406 (2019).

[139] R. H. Swendsen and J.-S. Wang, "Nonuniversal critical dynamics in monte carlo simulations", Phys. Rev. Lett. **58**, 86–88 (1987).

[140] U. Wolff, "Collective monte carlo updating for spin systems", Phys. Rev. Lett. **62**, 361–364 (1989).

[141] N. Prokof'ev and B. Svistunov, "Worm algorithms for classical statistical models", Phys. Rev. Lett. **87**, 160601 (2001).

[142] H. Evertz, "The loop algorithm", Adv. Phys. **52**, 1 (2003).

[143] G. Biroli and M. Mézard, "Lattice glass models", Phys. Rev. Lett. **88**, 025501 (2001).

[144] V. Blum, G. L. W. Hart, M. J. Walorski, and A. Zunger, "Using genetic algorithms to map first-principles results to model hamiltonians: application to the generalized ising model for alloys", Phys. Rev. B **72**, 165113 (2005).

[145] L. Berthier and G. Biroli, "Theoretical perspective on the glass transition and amorphous materials", Rev. Mod. Phys. **83**, 587–645 (2011).

[146] J. D. Biamonte, Phys. Rev. A **77**, 052331 (2008).

[147] W. Lechner, P. Hauke, and P. Zoller, "A quantum annealing architecture with all-to-all connectivity from local interactions", Science advances **1**, e1500838 (2015).

[148] M. Leib, P. Zoller, and W. Lechner, "A transmon quantum annealer: decomposing many-body ising constraints into pair interactions", Quantum Sci. Technol. **1**, 015008 (2016).

[149] V. Choi, "Minor-embedding in adiabatic quantum computation: ii. minor-universal graph design", Quantum Information Processing **10**, 343–353 (2011).

[150] M. E. Fisher, "Transformations of ising models", Phys. Rev. **113**, 969 (1959).

[151] F. J. Wegner, "Duality in generalized ising models and phase transitions without local order parameters", J. Math. Phys. **12**, 2259–2272 (1971).

[152] I. Syozi, "Statistics of kagomé lattice", Prog. Theor. Phys. **6**, 306 (1951).

[153] I Syozi, Phase Transition and Critical Phenomena, Vol. 1, edited by C. Domb, and M. S. Green (Academic, London, 1972).

[154] D. Antonosyan, S. Bellucci, and V. Ohanyan, "Exactly solvable ising-heisenberg chain with triangular xxz-heisenberg plaquettes", Phys. Rev. B **79**, 014432 (2009).

[155] O. Rojas, J. Valverde, and S. de Souza, "Generalized transformation for decorated spin models", Physica A **388**, 1419 –1430 (2009).

[156] B. Lisnyi and J. Strečka, "Exact results for a generalized spin-1/2 ising–heisenberg diamond chain with the second-neighbor interaction between nodal spins", Phys. Status Solidi B **251**, 1083 (2014).

[157] F. Y. Wu, "Eight-vertex model and ising model in a non-zero magnetic field: honeycomb lattice", J. Phys. A **23**, 375 (1990).

[158] K. Lin and F. Wu, "General 8-vertex model on the honeycomb lattice: equivalence with an ising model", Mod. Phys. Lett. B **4**, 311 (1990).

[159] W. T. Lu and F. Y. Wu, "Soluble kagome ising model in a magnetic field", Phys. Rev. E **71**, 046120 (2005).

[160] F Caravelli and C Nisoli, "Computation via interacting magnetic memory bbites: integration of boolean gates", arXiv:1810.09190 (2018).

[161] K. Lin and F. Wu,
"Rigorous results on the anisotropic triangular ising model",
Int. J. Mod. Phys. B **5**, 2125 (1991).

[162] R. J. Baxter, "Eight-vertex model in lattice statistics",
Phys. Rev. Lett. **26**, 832–833 (1971).

[163] R. J. Baxter, "Partition function of the eight-vertex lattice model",
Ann. Phys. (N.Y.) **70**, 193 –228 (1972).

[164] J. Strečka, "Strong- and weak-universal critical behaviour of a mixed-spin ising model with triplet interactions on the union jack (centered square) lattice", Entropy **20**, 91 (2018).

[165] J. Strečka, "Generalized algebraic transformations and exactly solvable classical-quantum models", Phys. Lett. A **374**, 3718 –3722 (2010).

[166] L. Čanová, J. Strečka, J. Dely, and M. Jaščur, Acta Phys. Pol. A **113**, 449 (2008).

[167] J. Strečka, L. Čanová, M. Jaščur, and M. Hagiwara, Phys. Rev. B **78**, 024427 (2008).

[168] J. Strečka, A Tanaka, L. Čanová, and T. Verkholyak,
Phys. Rev. B **80**, 174410 (2009).

[169] R. J. Baxter and F. Y. Wu, "Exact solution of an ising model with three-spin interactions on a triangular lattice",
Phys. Rev. Lett. **31**, 1294–1297 (1973).

[170] L. Onsager, "Crystal statistics. i. a two-dimensional model with an order-disorder transition", Phys. Rev. **65**, 117–149 (1944).

[171] R. J. Glauber, "Time- dependent statistics of the ising model",
J. Math. Phys. **4**, 294–307 (1963).

[172] N. Ito,
"Non-equilibrium relaxation and interface energy of the ising model",
Physica A **196**, 591 –614 (1993).

[173] F. Y. Wu, X. N. Wu, and H. W. J. Blöte,
"Critical frontier of the antiferromagnetic ising model in a magnetic field: the honeycomb lattice", Phys. Rev. Lett. **62**, 2773–2776 (1989).

[174] K. Binder, "Critical properties from monte carlo coarse graining and renormalization", Phys. Rev. Lett. **47**, 693–696 (1981).

[175] S Tanaka, R Tamura, and B. Chakrabarti,
Quantum spin glasses, annealing and computation
(Cambridge Univ. Press, Cambridge and Delhi, 2017).

[176] M. E. Fisher,
"Rigorous inequalities for critical-point correlation exponents",
Phys. Rev. **180**, 594–600 (1969).

[177] J. T. Barreiro, M. Müller, P. Schindler, D. Nigg, T. Monz, M. Chwalla, M. Hennrich, C. F. Roos, P. Zoller, and R. Blatt,
"An open-system quantum simulator with trapped ions", Nature **470**, 486 (2011).

[178] G. Barontini, R. Labouvie, F. Stubenrauch, A. Vogler, V. Guarrera, and H. Ott, "Controlling the dynamics of an open many-body quantum system with localized dissipation", Phys. Rev. Lett. **110**, 035302 (2013).

[179] R. Labouvie, B. Santra, S. Heun, and H. Ott,
"Bistability in a driven-dissipative superfluid",
Phys. Rev. Lett. **116**, 235302 (2016).

[180] T. Tomita, S. Nakajima, I. Danshita, Y. Takasu, and Y. Takahashi,
"Observation of the mott insulator to superfluid crossover of a driven-dissipative bose-hubbard system", Science Advances **3**, e1701513 (2017).

[181] M. Fitzpatrick, N. M. Sundaresan, A. C. Y. Li, J. Koch, and A. A. Houck,
"Observation of a dissipative phase transition in a one-dimensional circuit qed lattice", Phys. Rev. X **7**, 011016 (2017).

[182] G. Lindblad, "On the generators of quantum dynamical semigroups",
Comm. Math. Phys. **48**, 119–130 (1976).

[183] V. Gorini, A. Kossakowski, and E. C. G. Sudarshan,
"Completely positive dynamical semigroups of nâlevel systems",
Journal of Mathematical Physics **17**, 821–825 (1976).

[184] B. Kraus, H. P. Büchler, S. Diehl, A. Kantian, A. Micheli, and P. Zoller,
"Preparation of entangled states by quantum markov processes",
Phys. Rev. A **78**, 042307 (2008).

[185] M. J. Kastoryano, F. Reiter, and A. S. Sørensen, "Dissipative preparation of entanglement in optical cavities", Phys. Rev. Lett. **106**, 090502 (2011).

[186] S. Diehl, E. Rico, M. A. Baranov, and P. Zoller, "Topology by dissipation in atomic quantum wires", Nature Physics **7**, 971 (2011).

[187] C. Bardyn, M. Baranov, C. Kraus, E Rico, A İmamoğlu, P Zoller, and S Diehl, "Topology by dissipation", New Journal of Physics **15**, 085001 (2013).

[188] S. Diehl, A. Tomadin, A. Micheli, R. Fazio, and P. Zoller, "Dynamical phase transitions and instabilities in open atomic many-body systems", Phys. Rev. Lett. **105**, 015702 (2010).

[189] A. Tomadin, S. Diehl, and P. Zoller, "Nonequilibrium phase diagram of a driven and dissipative many-body system", Phys. Rev. A **83**, 013611 (2011).

[190] C. Ates, B. Olmos, J. P. Garrahan, and I. Lesanovsky, "Dynamical phases and intermittency of the dissipative quantum ising model", Phys. Rev. A **85**, 043620 (2012).

[191] Z. Gong, R. Hamazaki, and M. Ueda, "Discrete time-crystalline order in cavity and circuit qed systems", Phys. Rev. Lett. **120**, 040404 (2018).

[192] F. M. Gambetta, F. Carollo, M. Marcuzzi, J. P. Garrahan, and I. Lesanovsky, "Discrete time crystals in the absence of manifest symmetries or disorder in open quantum systems", Phys. Rev. Lett. **122**, 015701 (2019).

[193] Z. Cai and T. Barthel, "Algebraic versus exponential decoherence in dissipative many-particle systems", Phys. Rev. Lett. **111**, 150403 (2013).

[194] A. H. Werner, D. Jaschke, P. Silvi, M. Kliesch, T. Calarco, J. Eisert, and S. Montangero, "Positive tensor network approach for simulating open quantum many-body systems", Phys. Rev. Lett. **116**, 237201 (2016).

[195] A. A. Gangat, T. I, and Y.-J. Kao, "Steady states of infinite-size dissipative quantum chains via imaginary time evolution", Phys. Rev. Lett. **119**, 010501 (2017).

[196] A. Kshetrimayum, H. Weimer, and R. Orús,
"A simple tensor network algorithm for two-dimensional steady states",
Nat. Commun. **8**, 1291 (2017).

[197] H. Weimer, A. Kshetrimayum, and R. Orús,
"Simulation methods for open quantum many-body systems",
arXiv preprint arXiv:1907.07079 (2019).

[198] J. Cui, J. I. Cirac, and M. C. Bañuls, "Variational Matrix Product Operators for the Steady State of Dissipative Quantum Systems",
Phys. Rev. Lett. **114**, 220601 (2015).

[199] H. Weimer, "Variational principle for steady states of dissipative quantum many-body systems", Phys. Rev. Lett. **114**, 040402 (2015).

[200] J. Jin, A. Biella, O. Viyuela, L. Mazza, J. Keeling, R. Fazio, and D. Rossini, "Cluster mean-field approach to the steady-state phase diagram of dissipative spin systems", Phys. Rev. X **6**, 031011 (2016).

[201] J. Jin, A. Biella, O. Viyuela, C. Ciuti, R. Fazio, and D. Rossini, "Phase diagram of the dissipative quantum ising model on a square lattice",
Phys. Rev. B **98**, 241108 (2018).

[202] T. Prosen and I. Pižorn,
"Operator space entanglement entropy in a transverse ising chain",
Phys. Rev. A **76**, 032316 (2007).

[203] I. Pižorn and T. Prosen,
"Operator space entanglement entropy in xy spin chains",
Phys. Rev. B **79**, 184416 (2009).

[204] A. Peres, "Separability criterion for density matrices",
Phys. Rev. Lett. **77**, 1413–1415 (1996).

[205] M. Horodecki, P. Horodecki, and R. Horodecki,
"Separability of mixed states: necessary and sufficient conditions",
Physics Letters A **223**, 1 –8 (1996).

[206] K. Kraus, *States, effects, and operations* (SpringerVerlag, Berlin, 1983).

[207] M.-D. Choi, "Completely positive linear maps on complex matrices",
Linear Algebra and its Applications **10**, 285 –290 (1975).

[208] A. JamioÅkowski, "Linear transformations which preserve trace and positive semidefiniteness of operators",
Reports on Mathematical Physics **3**, 275 –278 (1972).

[209] B. Baumgartner and H. Narnhofer, "Analysis of quantum semigroups with GKS–lindblad generators: II. general",
Journal of Physics A: Mathematical and Theoretical **41**, 395303 (2008).

[210] S. G. Schirmer and X. Wang,
"Stabilizing open quantum systems by markovian reservoir engineering",
Phys. Rev. A **81**, 062306 (2010).

[211] T. Prosen, "Comments on a boundary-driven open xxz chain: asymmetric driving and uniqueness of steady states", Physica Scripta **86**, 058511 (2012).

[212] B. Horstmann, J. I. Cirac, and G. Giedke,
"Noise-driven dynamics and phase transitions in fermionic systems",
Phys. Rev. A **87**, 012108 (2013).

[213] J. Gambetta, A. Blais, M. Boissonneault, A. A. Houck, D. Schuster, and S. M. Girvin, "Quantum trajectory approach to circuit qed: quantum jumps and the zeno effect", Phys. Rev. A **77**, 012112 (2008).

[214] G. Torlai and R. G. Melko,
"Latent space purification via neural density operators",
Phys. Rev. Lett. **120**, 240503 (2018).

[215] S. Sorella,
"Generalized lanczos algorithm for variational quantum monte carlo",
Phys. Rev. B **64**, 024512 (2001).

[216] S.-I. Amari, K Kurata, and N. H,
IEEE Transactions on Neural Networks **3**, 260 (1992).

[217] S.-I. Amari, "Natural gradient works efficiently in learning",
Neural Computation **10**, 251–276 (1998).

[218] T. E. Lee, S. Gopalakrishnan, and M. D. Lukin, "Unconventional magnetism via optical pumping of interacting spin systems",
Phys. Rev. Lett. **110**, 257204 (2013).

[219] R. B. Lehoucq, D. C. Sorensen, and C. Yang, *ARPACK users' guide: solution of large-scale eigenvalue problems with implicitly restarted Arnoldi methods* **6** (1998).

[220] R. Jozsa, "Fidelity for mixed quantum states",
Journal of Modern Optics **41**, 2315–2323 (1994).

[221] J. Preskill, "Lecture notes for ph219/cs219: quantum information",

[222] N. Yoshioka and R. Hamazaki, "Constructing neural stationary states for open quantum many-body systems", Phys. Rev. B **99**, 214306 (2019).

[223] M. J. Hartmann and G. Carleo, "Neural-network approach to dissipative quantum many-body dynamics", Phys. Rev. Lett. **122**, 250502 (2019).

[224] F. Vicentini, A. Biella, N. Regnault, and C. Ciuti, "Variational neural-network ansatz for steady states in open quantum systems", Phys. Rev. Lett. **122**, 250503 (2019).

[225] A. Nagy and V. Savona, "Variational quantum monte carlo method with a neural-network ansatz for open quantum systems", Phys. Rev. Lett. **122**, 250501 (2019).

[226] G. Hinton, N. Srivastava, and K. Swersky,
"Neural networks for machine learning", Coursera, Video lectures (2012).

[227] B. T. Polyak,
"Some methods of speeding up the convergence of iteration methods", USSR Computational Mathematics and Mathematical Physics **4**, 1–17 (1964).

[228] D. P. Kingma and J. Ba, "Adam: a method for stochastic optimization", arXiv preprint arXiv:1412.6980 (2014).

[229] L. Molinari, J. Phys. A: Math. Gen. **30**, 983 (1997).

[230] A. Yamakage, K. Nomura, K. I. Imura, and Y. Kuramoto, "Criticality of the metal–topological insulator transition driven by disorder", Phys. Rev. B **87**, 205141 (2013).

[231] J. Gubernatis, N. Kawashima, and P. Werner,
Quantum Monte Carlo Methods (Cambridge University Press, 2016).

[232] A Coniglio, F de Liberto, G Monroy, and F Peruggi, "Exact relations between droplets and thermal fluctuations in external field", J. Phys. A **22**, L837 (1989).

[233] J Kent-Dobias and J. P. Sethna, "Cluster representations and the wolff algorithm in arbitrary external fields", Phys. Rev. E **98**, 063306 (2018).

[234] S. H. Simon and P. Fendley,
"Exactly solvable lattice models with crossing symmetry",
J. Phys. A **46**, 105002 (2013).

[235] K. A. Muttalib, M. Khatun, and J. H. Barry, Phys. Rev. B **96**, 184411 (2017).

[236] J. H. Barry and F. Y. Wu, Int. J. Mod. Phys. B **3**, 1247 (1989).